NASA-CR-159099

NASA CONTRACTOR REPORT 159099

Engine Induced Structural-Borne Noise in a General Aviation Aircraft

James F. Unruh, Dennis C. Scheidt and
Daniel J. Pomerening

SOUTHWEST RESEARCH INSTITUTE
San Antonio, Texas 78284

CONTRACT NAS1-14861
AUGUST 1979

National Aeronautics and
Space Administration

SOUTHWEST RESEARCH INSTITUTE
Post Office Drawer 28510, 6220 Culebra Road
San Antonio, Texas 78284

Engine Induced Structural-Borne Noise in a General Aviation Aircraft

James F. Unruh, Dennis C. Scheidt and
Daniel J. Pomerening

Prepared for
National Aeronautics and Space Administration
Langley Research Center
Hampton, Virginia

Final Report
Contract NAS1-14861
SwRI Project No. 02-4860

August 1979

Approved by:

H. Norman Abramson, Vice President
Engineering Sciences Division

FRONTISPIECE

ABSTRACT

An experimental and analytical study of structural-borne interior noise in a single engine general aviation aircraft was conducted to (1) determine the importance of engine induced structural-borne noise and (2) determine the necessary modeling requirements for the prediction of structural-borne interior noise. Engine attached/detached ground test data show that (1) engine induced structural-borne noise is a primary interior noise source for the single engine test aircraft, (2) cabin noise is highly influenced by responses at the propeller tone, and (3) cabin acoustic resonances can influence overall noise levels. Results from structural and acoustic finite element coupled models of the test aircraft show that (1) wall flexibility has a strong influence on fundamental cabin acoustic resonances, (2) the lightweight fuselage structure has a high modal density, and (3) finite element analysis procedures are appropriate for the prediction of structural-borne noise. The analytical studies were limited to the frequency range below 200 Hz due to a high structural modal density.

TABLE OF CONTENTS

LIST OF FIGURES

LIST OF FIGURES (CONT.)

LIST OF FIGURES (CONT.)

LIST OF TABLES

NOMENCLATURE

c	speed of sound in the acoustic media
i,j	indices
p	acoustic perturbation pressure
q_A	acoustic subvolume modal degrees of freedom
q_S	structural modal degrees of freedom
r	a subscript denoting r-th coupled mode
t	temporal variable
u	structural nodal displacements
x,y,z	Cartesian coordinates
A	subscript denoting acoustic region
$A(\omega)$	acoustic admittance, frequency dependent
B	the structural acoustic coupling matrix
$C_A(\omega)$	acoustic damping matrix, frequency dependent
C_S	structural damping matrix
F	externally applied structural forces
$\overline{F}$	generalized applied forces
I	subscript or superscript denoting interior region and unit diagonal matrix
K	stiffness matrix, in general
M	mass matrix, in general
N	number of basis functions
P	nodal perturbation pressure, in general
$\hat{P}_I$	interior pressures for zero surface pressures
Q	eigenvectors, in general
R	applied structural loads or acoustic region
S	transformed stiffness matrix or surface of acoustic region; also subscript or superscript denoting surface nodes
T	decoupling transformation submatrix
W	transformed mass matrix
β	critical damping ratio
γ	coupled system modal degrees of freedom
η	outward normal to the boundary
λ	eigenvalue, square of the circular frequency
ρ_o	mean density of the acoustic media
ϕ_j	j-th pressure series basis function
ψ	coupled system eigenvectors
ω	circular frequency
∇	gradient operator
∇^2	Laplacian operator

I. INTRODUCTION

Interior noise levels in propeller-driven general aviation aircraft are often higher than those considered marginally acceptable in other forms of transportation (ref. 1). Reduction of the interior noise levels is highly desirable for improved safety through improved intra-cabin and air-to-ground communications and reduced pilot fatigue, and for improved comfort of crew and passengers (refs. 2 and 3). Previous studies of the sources and characteristics of interior noise in general aviation aircraft (refs. 4, 5, and 6) have shown the interior noise spectra to be dominated by low frequency tones, at multiples of the engine 1/2 rpm harmonic, with the airborne propeller source and structural-borne engine vibration source providing the primary contributions. Nevertheless, a direct quantitative measure of the relative importance of these primary noise sources is not available.

Interior noise control considerations for light aircraft have received some attention in recent years (ref. 7). However, if efficient noise control measures are to be employed, the designer must have a quantitative measure of the relative importance of the primary noise sources and a means by which he can evaluate the effectiveness of a potential noise control measure.

In an effort to assess the importance of engine vibration as a source of structural-borne noise in a typical single engine light aircraft, an experimental and analytical program was undertaken with the specific objectives to:

(1) determine, through ground test, the importance of engine vibration as a source of interior noise,
(2) develop structural-borne noise prediction procedures, and
(3) investigate potential methods for structural-borne noise control.

The approach to this program has been to acquire a Cessna Model 172 single engine aircraft, and via direct decoupling of the engine and fuselage structure during ground test operations, obtain a measure of the engine-induced structural-borne interior noise component. A finite element structural-acoustic coupled model was then developed for structural-borne noise

prediction in the low frequency range up to 200 Hz. Predictions from the model were compared to the measured modal responses of the aircraft and through the use of measured input engine forces a comparison to the measured structural-borne interior noise levels during engine operation was obtained. A limited investigation of the sensitivity of structural-borne interior noise levels to several of the aircraft physical parameters was carried out. However, a thorough investigation of structural-borne noise control for the aircraft is the subject of a continued effort.

II. TEST FACILITY, INSTRUMENTATION, AND PROCEDURES

A. Test Aircraft

The test aircraft used during this investigation was a 1963 Cessna Model 172 Skyhawk. This model was chosen because of its wide-spread popularity as a light single engine aircraft and because its general construction and use of materials reflect present-day technology throughout the industry.

The Model 172 was equipped with a 145 HP, six-cylinder engine with a two-bladed, fixed-pitch propeller. For this configuration, the propeller harmonics are multiples of two times the engine rpm and the harmonics associated with the engine firing are multiples of three times the engine rpm. Later year models (after 1967) of the Model 172 were equipped with four-cylinder engines with two-bladed, fixed-pitch propellers. However, the fuselage construction since 1963 has remained unchanged.

As shown in the Frontispiece, the wings and empannage of the aircraft were removed during all tests. This was a safety precaution to eliminate potential rigid body motion during high rpm engine operations. Both forward and rear seats were also removed during all tests to accommodate microphone instrumentation.

B. Modal Survey Tests

Modal surveys for fundamental fuselage structural and cabin interior acoustic modes were carried out for both the interior-installed and interior-removed configurations. The interior-installed configuration consisted of all standard interior trim items with the exception of the front and rear seats. The total weight of removed trim items for the interior-removed configuration was 451 newtons (101.4 lbs); the front and rear seats accounted for 262 newtons (58.9 lbs) of this total.

1. Acoustic Mode Survey

Cabin interior acoustic modal surveys were conducted for the interior-installed and interior-removed configurations. Two methods of excitation were used: (1) the cabin volume was excited by an 8-inch audio speaker driven with constant current and placed in various corners of the cabin, and (2) an M.B. electrodynamic shaker was attached to the engine mount frame and directly to

the fuselage (ref. Figure 1) to provide a controlled force level throughout the frequency region of interest. Two 1/2-inch B&K condenser microphones were mounted in the cabin at fixed locations and were used for frequency response sweeps. For the interior-installed configuration, a 1/4-inch B&K microphone was mounted in the end of a 6-foot long steel probe and used through a small hole cut in the left door window to identify modal node points inside the cabin. For the interior-removed configuration, one of the 1/2-inch microphones was used to longitudinally traverse the full length of the cabin and aft fuselage.

The instrumentation and data acquisition system for the modal surveys is shown in Figure 2 . The procedure used to locate the acoustic resonances was to first sweep through the frequency range of interest and monitor the output of one of the fixed microphones. To obtain a clear microphone signal at the desired frequency, a 2 Hz bandwidth tracking filter (SD 122) was used. The noise source was held constant (constant current into the 8-inch speaker or constant force output from the shaker) by employing a Spectral Dynamics SD 105 amplitude servo/monitor which was driven by an SD 104A sweep oscillator. Apparent acoustic resonances, denoted by spikes in the response curves, were then further investigated by displaying the response of a pair of well separated microphones on a Tektronix storage scope. The frequency was manually tuned to peak both microphone outputs. If both microphones exhibited sharp tuned responses and both peaked at the same frequency, the response was considered to be a resonant acoustic mode. During the sweeps, the fixed microphones were moved about the cabin so as to eliminate the possibility of missing a mode, which could happen if one of the microphones were placed at a node of the mode.

An SD 109 CO/QUAD analyzer was then used to map the modal node lines. The procedure was to use a fixed microphone as one input to the analyzer while the other input was the traversing microphone output. In theory, as the traversing microphone passes through a node line, the phase would immediately shift 180°. However, in reality, dissipation in the system gives rise to a finite width node through which the phase will change continuously. Thus, by observing the relative phase of the two microphones, positions of the node lines were recorded at phases of 90°.

Modal decay of the well defined interior acoustic modes was recorded by direct storage of the decay signal as the input was abruptly turned off. For these records, the microphone outputs were input directly into the storage scope which was triggered by turning off the source. A permanent record of the decay was obtained with a Polaroid camera. Data for logarithmic decrement calculations were then taken from the photographs.

2. Structural Mode Survey

During the structural mode surveys, the aircraft was constrained by the tire hold-down fixtures used during the engine-running tests. For the interior-installed configurations, data were obtained for both engine-attached and engine-detached conditions, while for the interior-removed configuration data were obtained for the engine-attached only. A 50 lb_f M.B. electrodynamic shaker was used for all tests. For engine-off tests, the shaker was attached to the fuselage lower engine mount attach points with the shaker on the floor for vertical excitation, and mounted in a support frame for horizontal excitation. For the engine-attached tests, the shaker was attached to the engine mount and/or engine block for both horizontal and vertical excitation (ref. Figure 1). The instrumentation used for the modal searches consisted mainly of the instruments shown in Figure 2. A pair of Endevco #2221D accelerometers equipped with Kistler 504 charge amplifiers were used as vibration pickups. Sweeps were made to locate potential resonances, and thereafter, more detailed searches were conducted. For the overall bending modes, one accelerometer was fixed to the aircraft near an anti-node, while the other accelerometer was traversed manually along the fuselage in order to locate the nodes of the mode. For panel modes, sweeps were made with one accelerometer on the center of various panels while the second accelerometer was located on adjacent stiffeners or frame members. When the panel accelerometer peaked relative to the adjacent structure, the corresponding frequency was considered to be a panel mode. It was very difficult to isolate the panel vibration from the lightweight structure to which they were attached. This problem occurred to some degree at every panel tested.

C. Engine Running Tests

During the engine running tests, the aircraft was placed on a concrete test pad and its main landing gear wheels placed in a section of C8 channel

iron to restrain lateral motion. The channel iron was equipped with a pair of adjustable bookends to provide longitudinal restraint, and an over-the-wheel strap provided overall vertical restraint. The aircraft nose wheel was restrained in a similar manner with the shock strut in the collapsed position. Tire inflation pressures were regulated to maintain support frequencies below 11 Hz and to provide alignment between engine and fuselage during the engine-detached configuration. The deflated tires provided a minimum of 10 dB of vibration isolation between the test pad and aircraft.

The aircraft engine was attached to the fuselage at the four engine-to-fuselage attach points as indicated in Figure 3 . A pair of engine support stanchions consisting of a main support (TS 4 x 4 x 0.25) stiffened by three strut braces (3.0 OD x 0.25) provided support for the engine in the engine-detached configuration. Each of the stanchions was equipped with two protruding ears to pick up the four engine mount attach tubes to provide engine support during the engine-detached configuration. The ears protruded through the engine cowl picking up the front side of the engine mount tubes. A false firewall provided support for the engine cowl. The engine support system and false firewall is shown in Figure 4 . The engine-detached configuration required a forward movement of the engine and cowl of approximately 3.2 cm (1.25 in). During the engine-attached runs, the engine support system was left in place to maintain a constant airborne noise source between the engine-detached and engine-attached configurations. In general, one would expect this configuration to produce a somewhat higher airborne noise source than that from an unmodified aircraft. This would tend to make comparisons of engine-attached to engine-detached data yield conservative results for the engine induced structural borne noise component. The aircraft was equipped with 7.6 m (25 feet) exhaust extensions to prevent excessive exhaust noise via direct exhaust impingement onto the test pad. Engine speed was remotely controlled via a DC motor connected directly to the carbureter linkage.

The aircraft was instrumented to obtain interior noise levels, fuselage vibration levels, and engine force and acceleration levels. The engine input force levels into the fuselage were obtained via axial strain measurements made at each of the seven engine mount strut members, as shown in Figure 3. The engine acceleration levels were obtained from a triaxial

accelerometer arrangement placed on the top center of the engine. Fuselage acceleration measurements were taken at the twenty-one locations as specified in Figure 5. A corresponding description of the accelerometer locations are given in Table 1. An external microphone was placed on center 3.0 meters forward and in line with the propeller spinner to provide an external noise source reference, denoted as MER. A fixed internal reference microphone (MIR) located near the pilot's normal nead position was used with two movable microphones to map the noise field within the cabin at fourteen preset locations. The microphone locations are shown in Figure 6.

A timing reference signal was capacitively coupled from the No. 1 spark plug wire and shaped with an electronic circuit to produce a square pulse at the basic firing frequency of the No. 1 cylinder. This signal was recorded as the timing reference and also used to precisely monitor the engine speed on an electronic counter.

The accelerometers, microphones, and strain gages were driven by transducer preamplifiers, located in or near the aircraft. Output signals from the preamplifiers were then routed approximately 20 meters to an instrumentation control shack where variable gain amplifiers were used to condition all signals prior to recording. All signals were recorded on 14-channel magnetic tape for permanent record and subsequent data reduction. A schematic showing instrumentation methods employed during the engine running tests is given in Figure 7.

Detailed data specifications for all experimental tasks are given in the Data Report (Ref. 8). Data were recorded at five engine speeds: 1680, 1800, 1920, 2040, and 2160 rpm, corresponding to engine 1/2 rpm harmonics of 14, 15, 16, 17, and 18 Hz, respectively. Interior noise field and fuselage vibration levels were recorded for the following configurations:

(1) Engine attached - interior installed
(2) Engine detached - interior installed
(3) Engine attached - interior removed
(4) Engine detached - interior removed

TABLE 1. DESCRIPTION OF ACCELEROMETER LOCATIONS

Position	Description
A1A	Firewall Structure at Engine Attach Pt. #1.
A2A	Floor Panel Below Pilot Seat ≈ B.S. 40.
A3A*	Right Side Aft Panel at ≈ B.S. 100.
A1B	Upper Firewall Center Panel.
A2B	Floor Frame Below Center Rear Seat ≈ B.S. 75.
A3B*	Top Center Aft Tail Cone at Rear Window ≈ B.S. 116.
A1C	Windshield Midcenter.
A2C	Top Center Front Door Frame.
A3C*	Right Side Center Tail Cone at ≈ B.S. 124.
A1D	Right Side of Windshield.
A2D	Top Right Side Panel Between Door Frames ≈ B.S. 44.
A3D*	Right Side Center Tail Cone at ≈ B.S. 154.
A1E	Center Right Door Window.
A2E	Top Center Rear Door Frame.
A3E*	Right Side Center Tail Cone at B.S. 178.
A1F	Right Side Center Door Panel.
A2F	Top Right Panel Aft of Door at ≈ B.S. 80.
A3F*	Top Center Aft Tail Cone ≈ B.S. 160.
A1G	Center Right Rear Window.
A2G	Right Side Aft Panel at ≈ B.S. 80.
A3G*	Bottom Center Aft Tail Cone ≈ B.S. 160.

* Not used during Interior-Installed Configurations.

Engine force and acceleration levels were recorded for the engine-attached configuration.

D. Data Reduction

The data reduction of the signals taped during the engine running tests was primarily centered around a MINI-UBIQUITOUS® 444A FFT computing spectrum analyzer. The analyzer features 400-line narrowband analysis as well as 1/3 or 1/1 octave band analysis. The 1/3 or 1/1 octave bands are synthesized from 400-line spectra. Their center frequencies, bandwidths, and effective roll-offs meet ANSI Standard Class III. The analyzer also features a built-in A-weighting network which can be switched in at the input to produce 1/3 or 1/1 octave spectra modified by the A-weighting response curves. Earlier in the program, a UBIQUITOUS UA500, 500-line narrowband analyzer was also used to obtain several narrowband spectra. A Saicor SAI-43A correlation and probability analyzer with 400-line resolution was used for a detailed signal cross-correlation analysis.

From preliminary narrowband analysis of the data, it was determined that the major components of the data were deterministic complex periodic. However, due to slight changes in engine rpm, which is attributed to normal combustion engine operation and slight variations in propeller inlet wind loading, a slight unsteadiness in the data results. It was determined that averaging four seconds of data resulted in a stationary spectrum. The data reduced using the MINI-UBIQUITOUS analyzer represents an average of approximately ten seconds of data per channel. All microphone data were high-passed at 10 Hertz prior to recording and/or analysis to eliminate any unwanted signals due to "rigid body" motion of the aircraft. Overall level data were obtained from 1/3 octave analysis in the frequency range from 10 to 5000 Hz.

The sound pressure level data presented herein are referenced to $p_r = 2 \times 10^{-5}$ N/m^2 and defined in the usual way by

$$SPL = 10. * \log_{10} \left(\frac{p_{rms}}{p_r} \right)^2$$

Acceleration data are presented either in standard gravitational acceleration units, g, where $g = 9.807$ m/s^2, or in acceleration levels referenced to $a_r = 1.0g$, and defined by

$$AL = 10. * \log_{10} \left(\frac{a_{rms}}{a_r} \right)^2$$

The force data are given in levels defined by

$$FL = 10. * \log_{10} \left(\frac{f_{rms}}{f_r} \right)^2$$

where $f_r = 88.96\,N$ $(20\ lb_f)$.

For a given physical configuration, i.e., engine-attached/detached and interior installed/removed, and for a given engine speed, seven data signals were recorded at the exterior reference and interior microphones while the movable microphones provided data at the other fourteen locations. From the seven interior microphone readings, mean and standard deviations of the MIR were computed via

$$\overline{MIR} = 10. * \log_{10} \left[\frac{1}{N} \sum_{i=1}^{N} 10^{(MIR_i/10)} \right]$$

where $\overline{MIR}$ is the mean value expressed in dB;
MIR_i is an individual reading; and
N is the number of samples, i.e., $N = 7$

The standard deviation is computed from

$$\sigma = 10.* \log_{10} \left\{ \left[\frac{1}{N-1} \sum_{i=1}^{N} \left(10.^{(MIR_i/10)} - 10^{(MIR/10)} \right)^2 \right]^{\frac{1}{2}} \right\}$$

where σ is the standard deviation expressed in dB.

To obtain a distribution of sound pressure levels throughout the cabin, all microphone levels were referenced to a single MIR level. This was accomplished by using the mean $\overline{MIR}$ level as computed above and by applying corrections to each of the movable microphone levels of the form:

$$\overline{MIX_i} = 10. * \log_{10} \left[\left(\frac{10^{(\overline{MIR}/10)}}{10^{(MIR_i/10)}} \right) * 10^{(MIX_i/10)} \right]$$

where $\overline{M1X_i}$ is the local adjusted level at location 1X, $M1X_i$ is the unadjusted local level, MIR is the mean interior reference level, and MIR_i is the local interior reference level.

The speech interference levels, PSIL, given in the following section were obtained from the arithmetic average of the sound pressure levels in the three octave bands with geometric mean center frequencies at 500, 1000, and 2000 Hz.

Linear regression and simple linear correlation analyses of several of the data are presented in the following section to show certain relationships between the noise, vibration, and force levels. The stated correlation coefficient, R, is a measure of the "degree of fit" of the given points to a lease squares straight line. When $R = \pm 1$, the correlation is exact, while the variables are uncorrelated with a linear equation when $R = 0$.

III. TEST RESULTS

Presentation of the test results obtained during the program is divided into two major sections. The fuselage modal data results, consisting of measured acoustic interior resonances, structural fuselage and panel resonances, and forced harmonic response transfer function data, are given first to demonstrate the low frequency response characteristics of the lightweight fuselage structure. This data estalishes a foundation for interpreting the engine-running data and provides fundamental data for comparison to analytical model predictions. Engine-running data for the various engine-attached/detached and interior-installed/removed configurations are then given. By direct comparison of engine-detached to engine-attached data, a measure of the engine-alone contribution to the interior noise levels and fuselage vibration levels is obtained. The measured engine mount force levels provide the basic input spectra from which structural borne interior noise levels can be predicted using the analytical model. Comparison of analytical and experimental results are given in Section V. Reference is made to the Data Report of Reference 8 for additional supporting data.

A. Fuselage Modal Data

Modal surveys of the aircraft structure and cabin acoustic volume were carried out for both the interior-removed and interior-installed configurations. An electrodynamic shaker was attached to the engine mount frame and/or directly to the fuselage (as described in Section II) to provide a controlled force level during frequency sweeps to excite structural and acoustic resonances of the fuselage and cabin. Signals from fuselage-mounted accelerometers and microphones positioned within the cabin were used to detect the various resonances.

1. Acoustic Resonances

In general, the various structural panel resonances dominated the interior microphone response during the sweeps. Nevertheless, a series of well defined cabin acoustic resonances were found. In Table 2, those resonances below 100 Hz are listed along with their critical damping ratios. The lower modes were reasonably clear and exhibited clean decays except for

the 40.4 Hz mode, which appeared to be highly coupled with the flexible interior bulkhead at B.S. 108. Higher modes were also recorded; however, their decays exhibited considerable beating, indicating a coupling with the structure. The acoustic resonances given in Table 2 were all longitudinal modes having a single node plane within the fuselage cabin. For a maximum cabin dimension of 2.74m (108 in), one would expect an acoustic resonance at 62.5 Hz, based on a speed of sound of 343 m/s. However, if the total length of the fuselage were considered, i.e., into the tail cone, the maximum dimension would be 5.23m (205.8 in.) resulting in an expected resonant mode at 32.8 Hz. Upon examination of the frequencies given in Table 2, we can see that the standard interior bulkhead at B.S. 108 was transparent to the fundamental cabin mode, the node plane being near the plane of the bulkhead. The 62 Hz mode is the second cabin mode, while the 40.4 Hz mode is a coupled structural-acoustic response. As will be shown in the engine-running data, these fundamental resonances are highly excited at an engine speed of 1920 rpm. Node line plots and corresponding frequencies for several of the lower modes are given in Figure 8. Only a single mode, at 152 Hz, exhibited a node plane along the cabin height and no modes were found to have distinct node planes along the width of the cabin. With a maximum cabin width of 1.07m (42.0 in.) and height of 1.22m (48.0 in.) expected hardwalled frequencies would be 161 Hz and 141 Hz, respectively.

TABLE 2. CABIN ACOUSTIC RESONANCES BELOW 100 HZ

Configuration	Frequency Hz	Damping Ratio
Std. Interior Flexible Bulkhead at B.S. 108	32.6	0.054
	40.4	**
	61.9	0.020
Std. Interior Rigid Bulkhead at B.S. 108	62.0	0.016
Std. Interior Bulkhead at B.S. 108 Removed	34.0	0.023
	63.0	0.022
Interior Removed	35.0	0.030
	64.0	0.018

**Beating

2. Structural Resonances

During the structural modal survey, the aircraft was constrained by the tire holddown fixtures used during the engine-running tests. The rigid body frequencies of the aircraft against its tires were found to be 6.1 Hz in the vertical, 7.6 Hz in roll, and 10.1 Hz in pitch. These frequencies were judged to be sufficiently low to consider the aircraft to be in a free condition. Figure 9 summarizes the fuselage primary bending mode responses, wherein frequencies and node line plots are given for both engine-attached and engine-detached configurations. During the engine-attached resonances considerable engine and engine mount motion occurred. As can be seen by the node line plots given in Figure 9, this motion contributed greatly to the overall bending responses of the fuselage. There may be some question as to the importance of the shift in fuselage bending frequency when the engine is detached with respect to its influence on the engine-running data. As will be seen in the engine-running data, the primary low frequency response occurs at the propeller tone. The propeller tone in the engine-running tests varied from 56 to 72 Hz for the various engine rpm conditions. Thus, the shift in the fuselage vertical bending mode from 14.4 to 56.4 Hz should, at most, influence only the propeller response at the 1680 rpm condition. As will be seen, no such effect appears in the engine-running data.

Resonant responses of several panels in the cabin and tail cone area were recorded for the engine-attached and engine-detached, and interior-installed and interior-removed configurations. A summary of the fuselage panel resonant frequencies are given in Table 3. In Table 3, the panel locations are identified by the corresponding accelerometer locations used during the engine-running tests (reference Figure 5 and Table 1 discussed in Section II). In general, panel vibrations could not be isolated from the lightweight structures to which they were attached. The removal of the engine or interior trim did not appreciably affect the fundamental resonant frequencies of the fuselage panels. Decay traces of several panels were recorded; however, they were often quite erratic with considerable beating. Due to the erratic decay of the various panels, a measure of the damping effectiveness of the interior trim could not be determined.

TABLE 3. SUMMARY OF FUSELAGE PANEL RESONANT FREQUENCIES

Panel Location*	Resonant Frequencies (Hz)
A2A	103, 163, 215
A1C	103, 156, 200
A3C	44, 47
A2D	121, 180, 220
A3D	44, 47, 61
A1E	45, 92
A1F	30
A2F	73, 98
A3F	93, 130, 200
A1G	60, 75, 125

*Corresponding to accelerometer locations (see Fig. 5)

3. Transfer Functions

Transfer functions for firewall excitation to fuselage vibration and interior noise response were recorded to clarify the character of the acoustic and structural responses in the lower frequency range (10-400 Hz). Typical examples are given in Figures 10 through 12. The input motion was at engine mount position 2, lower left, driving longitudinally at a constant force. The sweep rate was set at 0.2 decades per minute which was considered to be sufficiently slow to capture the character of the resonances. The engine was removed and the interior installed. Figure 10 gives the transfer function of the acceleration at the right door, accelerometer position A1F. The panel mode at 30 Hz and structural side bending mode at 53 Hz are the first two broadband peaks. The sharp peak at approximately 40 Hz is attributed to the acoustic mode at 40.4 Hz, but the peak at approximately 44 Hz is not identified as a structural, panel, or acoustic resonance. Typical acceleration response of a frame member, A2C, which is the top center front door frame, is given in Figure 11. No distinct structural resonances appear in the transfer function.

The transfer function for firewall excitation to interior noise at MIR, near the pilot's head, is given in Figure 12. The fundamental acoustic resonance

at 32.6 appears as a rather broadband response; the 40.4 Hz acoustic resonance is the next strongest resonance. Thereafter, the spectra is rich with various resonances that can be correlated with the panel resonances given in Table 3.

It is apparent from the transfer function data that numerous resonances are present below 100 Hz, and above 100 Hz, the responses become more broadband in character. This confirms the difficulty that was encountered in attempting to obtain clear resonances, either panel, structural, or acoustic, in the higher frequency ranges.

B. Engine Running Data

In the sections to follow, representative noise, vibration and force data will be given and overall data trends will be discussed. This study was primarily focused on structural-borne noise, as determined from direct subtraction of the engine-attached and engine-detached data. Nevertheless, to qualify the ground test procedures and to insure that statistically significant data were obtained, some discussion as to data analysis procedures employed and comparison to flight data in the literature will be given.

1. Narrow Band Spectra

Representative narrow band spectra of interior sound pressure, fuselage acceleration, engine strut force, and engine acceleration levels are given in Figure 13, As can be seen, these spectra are mainly complex periodic, consisting of engine 1/2 rpm harmonics (18 Hz for the 2160 rpm condition). The interior noise and fuselage vibration spectra are dominated by the first propeller harmonic at 72 Hz, with support from the second and third propeller harmonics occurring at 144 and 215 Hz, respectively. By comparison of the engine-attached to engine-detached spectra, it can be seen that the engine-attached spectra are considerably richer in harmonics than the engine-detached spectra. However, responses at all harmonics decrease, to varying degrees, when the engine is detached. It is of interest to note that the broadband noise and fuselage vibration levels remain essentially unchanged when the engine is detached. Detailed analysis of the various harmonic contributions of similar flight data are given in Reference 5.

The probability density functions (PDF) of the interior reference microphone at each of three engine speeds are given in Figure 14. The un-

filtered PDF shows the overall signals to be random, as expected from a combination of tones. When the signal was filtered through a 2-1/2 Hz bandwidth filter centered at the first propeller harmonic, the PDF showed the signal to be somewhat random, particularly at the higher rpm. It was noted that during most of the data acquisition a slight engine speed modulation occurred which explains the random nature of the response since a modulated pure tone will appear as a narrow band random signal. With the filter centered at the second propeller harmonic, the PDF showed the signal to be very much harmonic.

Auto- and cross-correlation analysis techniques were also applied to the noise and fuselage vibration data. The data analyses are given in Reference 8. In general, the correlation analyses showed the signals to be very much harmonic and, hence, phase-correlated. Thus, correlation analysis of these signals were of no value in determining noise source contributions.

The engine strut force level spectra (see Figure 13c) are dominated by the fundamental engine 1/2 rpm harmonic with support from various higher harmonics and what appears to be a series of engine to engine mount resonances occurring above 200 Hz. The engine acceleration spectra (see Figure 13d), while also rich with engine 1/2 rpm harmonics, tend to increase in magnitude up to approximately 400 Hz, with a dropping of or leveling out in magnitude thereafter.

To obtain a more comprehensive view of engine induced structural-borne noise, in the sections to follow, data will be presented as one-third octave spectra and overall levels out to 5000 Hz.

2. Sound Pressure Level Data

As discussed in Section II, mapping of the sound pressure levels within the cabin required seven configuration changes using two movable microphones to obtain data at fourteen locations. During each of the seven runs, data were taken at the fixed external reference, MER, and fixed internal reference, MIR, microphones. The statistical significance of the sound pressure level data can then be judged by correlation plots of overall sound pressure levels (OASPL) at MER and MIR. A typical correlation plot is shown in Figure 15. In general, the data scatter decreases with increasing rpm and increases when the interior is removed. However, the engine-attached data are well separated

from the engine-detached data, and the scatter within similar configurations is, in general, much less than the mean OASPL difference between configurations.

Results from a statistical analysis of the seven PSIL, OASPL linear, and OASPL A-weighted levels obtained at the interior reference microphone during east test configuration are given in Table 4. From the seven interior microphone readings, mean and standard deviations of the MIR were computed via the expressions given in Section II.D. The changes in dB level per doubling of engine speed are also given in Table 4. These values were obtained directly from a linear regression of the level data. The engine-alone levels were computed from the difference in engine-attached and engine-detached levels. It is important to note that the engine-alone contributions are most accurately determined when a large difference in levels exists. As the difference drops, it is more likely that the level difference is only data scatter rather than significant data. For example, the 1σ spread for the mean non-weighted OASPL levels at MIR at 1680 rpm with the interior installed, are calculated as follows: From Table 4, the mean level for the engine-attached is MIR = 101.4 dB and standard deviation σ = 89.8 dB, from which we obtain MIR + 1σ = 101.6 dB and MIR - 1σ = 101.1 dB. Likewise, for the engine-detached, MIR = 98.0 dB and σ = 91.7 dB, from which we obtain MIR + 1σ = 98.9 dB and MIR - 1σ = 96.8 dB. The maximum difference in engine-attached and engine-detached is 101.6 - 96.8 = 99.9 dB, whereas the minimum difference is 101.1 - 98.9 = 97.1 dB. Thus, the 1σ variation for the engine-alone contribution is 99.9 to 97.1 dB. The level given in Table 4 is 98.7 dB based on the difference of mean levels only.

The mean levels of MIR are plotted versus engine speed in Figure 16 for the interior-installed configuration. The linear correlation line for the OASPL and A-weighted levels for the engine-attached configuration are also noted. These curves show the OASPL data to increase 20.6 dB in level per doubling of engine speed, and the A-weighted level to increase 16.8 dBA per doubling of engine speed. This data compares well to the flight data reported by Jha and Catherines (ref. 5) wherein increases in levels of 20 dB non-weighted and 17 dBA per doubling of speed were reported. However, the overall levels for the ground test data are higher than the flight test data at the same rpm condition. This in part is attributed to the differences in engine power levels between flight and ground operations for the same engine speed and in part to ground reflection. No attempt is made here to correct for

TABLE 4. STATISTICAL PROPERTIES OF MIR

(a) Interior Installed

Engine RPM	Engine Attached						Engine Detached						Attached-Detached		Engine Alone	
	PSIL-dB		OASPL-dB		OASPL-dBA		PSIL-dB		OASPL-dB		OASPL-dBA		OASPL-dB	OASPL-dBA	OASPL-dB	OASPL-dBA
	$\bar{x}$	σ	$\bar{x}$	σ	$\bar{x}$	σ	$\bar{x}$	σ	$\bar{x}$	σ	$\bar{x}$	σ	$\bar{x}$	$\bar{x}$	$\bar{x}$	$\bar{x}$
1680	82.5	70.4	101.4	89.8	88.5	78.9	79.6	72.1	98.0	91.7	85.3	76.8	3.4	3.2	98.7	85.7
1800	84.2	73.3	101.5	93.9	89.7	81.0	80.8	72.8	99.2	93.1	86.6	79.0	2.3	3.1	97.7	86,8
1920	84.8	72.8	106.4	95.7	90.6	78.0	82.4	76.4	100.6	91.1	88.4	81.0	5.8	2.3	105.0	86.7
2040	86.2	78.9	106.4	94.0	92.7	80.9	83.7	76.0	102.3	90.5	89.8	77.5	4.2	2.8	104.3	89.5
2160	88.3	80.2	107.2	94.5	93.7	81.5	84.9	75.5	103.3	93.2	90.7	81.6	3.9	3.0	104.9	90.7
Slope*	17.0		20.6		16.8		16.9		17.1		17.5				23.8	15.9

(b) Interior Removed

Engine RPM	Engine Attached						Engine Detached						Attached-Detached		Engine Alone	
	PSIL-dB		OASPL-dB		OASPL-dBA		PSIL-dB		OASPL-dB		OASPL-dBA		OASPL-dB	OASPL-dBA	OASPL-dB	OASPL-dBA
	$\bar{x}$	σ	$\bar{x}$	σ	$\bar{x}$	σ	$\bar{x}$	σ	$\bar{x}$	σ	$\bar{x}$	σ	$\bar{x}$	$\bar{x}$	$\bar{x}$	$\bar{x}$
1680	89.0	84.4	105.6	97.8	95.4	91.6	83.1	75.9	101.3	94.3	88.5	81.2	4.3	6.9	103.5	94.4
1800	90.2	86.9	108.7	102.7	96.1	92.4	84.8	74.0	103.5	94.3	90.4	80.9	5.1	5.7	107.1	94.7
1920	91.2	86.8	111.0	105.9	97.0	92.3	86.7	77.4	105.7	98.4	92.3	80.9	5.4	4.8	109.5	95.3
2040	92.5	87.6	110.6	104.3	98.6	94.2	88.5	80.8	107.6	98.5	94.3	86.8	3.0	4.3	107.7	96.6
2160	93.7	88.9	111.7	100.7	99.9	94.2	89.0	78.6	108.3	101.6	95.2	87.1	3.4	4.7	109.1	98.0
Slope*	14.6		17.6		14.4		19.4		22.6		21.6				14.8	11.4

* dB level per doubling of engine RPM, via linear regression.

these effects without having available appropriate flight test data. Note, however, that any increase in airborne source such as that due to ground reflection would tend to lend some conservatism to the computed engine-alone values.

The engine-alone noise levels at MIR versus engine speed are given in Figure 17. If the engine-detached levels represent primarily contributions from the airborne propeller source, it may be concluded that the engine-induced structure-borne noise levels as given in Figure 17, equal or exceed the airborne propeller levels at all engine speeds. Based on the data presented in Reference 2, these A-weighted structure-borne noise levels are higher than those generally considered to be acceptable for comfortable intra-cabin speech communication.

In general, the distribution of OASPL throughout the cabin showed, at most, a 3-4 dB variation, with the primary exception occurring at an engine speed of 1920 rpm. The variation in OASPL throughout the cabin for the interior-installed, engine-attached, 1920 rpm configuration is given in Figure 18. The 1920 rpm configuration shows a significant longitudinal variation in noise level within the cabin. This variation is attributed to an acoustic modal amplification. Recall the fundamental cabin acoustic resonances are near 32 and 64 Hz which correspond identically to the engine rpm and fundamental propeller harmonics at an engine speed of 1920 rpm. This accounts for the higher unweighted level values measured at 1920 rpm. A similar resonance appeared in the flight data reported in Reference 5 at an engine speed of 2000 rpm; however, no explanation was given for the higher levels. The resonance condition is quite easily identified in the one-third octave spectra given in Figure 19. The shaded levels indicate the effect of detaching the engine. More typical one-third octave spectra are given in Figure 20 for the 2160 rpm condition.

For the purpose of developing noise control measures for this aircraft, it is important to note where the energy lies in the A-weighted spectra. As can be seen in Figures 19 and 20, there is a shift in peak response from the low frequency region, at the propeller tone, to the higher frequency region, around 1000 Hz, when applying the A-weighted corrections. However, this trend diminishes as the engine speed increases. This is more easily seen by the data plotted in Figure 21 wherein the difference in A-weighted one-third

octave peak level and the level in the one-third octave containing the propeller tone is plotted versus engine speed. Note that the data in Figure 21 at 1920 rpm is somewhat misleading due to the acoustic cabin resonance amplifying the level at the propeller tone. Thus, it appears that initially, high frequency noise control measures need to be looked at; however, if substantial reduction is desired, the low frequency region of the spectra will also require attention.

Overall effects of removing the interior trim are obtained from an analysis of the difference in mean levels obtained from the interior-removed and interior-installed data. The difference data are presented in Table 5, along with mean difference values. From the linear OASPL difference values we see that the interior trim consistently provides a little over 4 dB of noise reduction in the spectra out to 5000 Hz. To determine what region of the spectra the interior is most effective will require more detailed analysis; however, in general, we can see a marked increase in the effectiveness of the trim when A-weighting is applied to the spectra. Thus, we may conclude that the interior is most effective in the higher frequency regions since A-weighting reduces the influence of the contributions below 1000 Hz.

It is quite interesting to note the effectiveness of the interior trim in reducing structure-borne noise. The A-weighted mean level differences given in Table 5 for the engine-alone noticeably exceed those given for engine-attached or engine-detached configurations. In Figure 22, engine-alone one-third octave spectra at MIR are given for the interior-installed and interior-removed conditions at an engine speed of 2160 rpm. The void in several of the analysis bands indicate that the engine-attached and engine-detached mean levels in these bands were not sufficiently different to yield significant engine-alone contributions. These figures show that the interior trim is quite effective in reducing higher frequency structure-borne noise. The equivalent A-weighted spectra to those given in Figure 22 are given in Figure 23. The spectra have been combined to show directly the effectiveness of the interior trim. If additional structure-borne noise control measures are to be applied to this aircraft, work in both the mid-frequency range and low-frequency range will be necessary.

TABLE 5. EFFECTS OF REMOVING THE INTERIOR TRIM

ENGINE RPM	DIFFERENCES IN MEAN LEVELS OF MIR INTERIOR REMOVED LEVEL - INTERIOR INSTALLED LEVEL					
	ENGINE ATTACHED		ENGINE DETACHED		ENGINE ALONE †	
	OASPL-dB	OASPL-dBA	OASPL-dB	OASPL-dBA	OASPL-dB	OASPL-dBA
1680	4.2	6.9	3.3	3.2	4.8	8.7
1800	(7.2)*	6.4	4.3	3.8	(9.4)*	7.9
1920	4.6	6.4	5.1	3.9	4.5	8.6
2040	4.2	5.9	5.3	4.5	3.4	7.1
2160	4.5	6.2	5.0	4.5	4.2	7.3
Mean	4.4 (4.9)*	6.4	4.6	4.0	4.2 (5.3)*	7.9

† Computed values from engine attached - engine detached levels.

* These values were removed from the computed means.

3. Fuselage Vibration Levels

Overall fuselage rms acceleration levels for the interior-installed and interior-removed configurations are given in Table 6. Reference is made to the accelerometer locations given in Figure 5 and the physical descriptions given in Table 1. In general, the fuselage acceleration levels decreased when the engine was detached, and increased slightly when the interior was removed. This can be more readily seen by examination of the engine-attached to engine-detached response ratios given in Table 7. For those accelerometer response ratios near to 1.0, the particular fuselage location is insensitive to engine-induced structural borne vibration, whereas a sensitive location would have a response ratio greater than 1.0. The accelerometer at location A2D, yielded slightly higher responses when the engine was detached for a majority of the test configurations. This accelerometer is located on a panel on top of the aircraft cabin above the co-pilot's head. The response ratios for A2D being somewhat less than 1.0, implies that engine-induced structural borne vibration is a destructive source when combined with the airborne component. The possibility of a shift in panel frequency between the engine-attached and engine-detached configuration being the reason for the odd behavior of A2D is discarded based on the modal survey results presented in Section III.A.2. On the other hand, the somewhat erratic behavior of A1B may have been due to a change in local stiffness when the engine was detached. A1B was attached to the firewall.

To obtain a better understanding of the spectral distribution of accelerometer responses, one-third octave band analyses of the acceleration signals were obtained for all configurations. Upon inspection of the one-third octave spectra, it was found that a majority of the signal energy was contained within three of the analysis bands. As an example, in Table 8, the three highest one-third octave band acceleration levels for all accelerometers are given for the interior-removed, engine-attached configuration at an engine speed of 2160 rpm. In this table, the overall acceleration levels, in g_{rms}, are given along with the percent of the total rms level contained in the three highest band levels. Similar analysis of the accelerometer signals for all other configurations are given in Reference 8, along with a brief synopsis of the spectral activity at each accelerometer.

Accelerometer Positions	ACCELEROMETER LEVELS (g's)					
	1680 rpm		1920 rpm		2160 rpm	
	Engine Attach.	Engine Detach.	Engine Attach.	Engine Detach.	Engine Attach.	Engine Detach.
A1A	1.30	.292	1.73	.415	2.33	.533
A2A	.281	.163	.402	.263	.597	.277
A3A						
A1B	.992	.904	1.57	1.11	1.71	1.79
A2B	.201	.0979	.348	.140	.356	.187
A3B						
A1C	.531	.234	.637	.388	1.59	.572
A2C	.424	.145	.531	.188	.623	.239
A3C						
A1D	.623	.443	.900	.763	1.53	1.23
A2D	.878	.910	1.49	1.92	2.30	2.86
A3D						
A1E	.558	.399	.511	.585	.976	1.16
A2E	.251	.145	.326	.212	.492	.374
A3E						
A1F	.403	.220	.603	.338	.531	.461
A2F	.330	.268	.759	.455	.976	.798
A3F						
A1G	.420	.601	.619	.400	1.15	.671
A2G	.613	.320	.485	.351	.785	.578
A3G						

(a) Interior Installed

Accelerometer Positions	ACCELEROMETER LEVELS (g's)					
	1680 rpm		1920 rpm		2160 rpm	
	Engine Attach.	Engine Detach.	Engine Attach.	Engine Detach.	Engine Attach.	Engine Detach.
A1A	2.24	.541	2.90	.767	3.51	.949
A2A	.792	.340	.845	.550	1.16	.685
A3A	.570	.392	.806	.525	1.12	1.11
A1B	1.57	1.08	3.64	1.87	3.52	2.93
A2B	.306	.151	.460	.317	.609	.395
A3B	.381	.139	.621	.259	.708	.333
A1C	.617	.245	.884	.427	1.64	.806
A2C	.552	.161	.845	.249	.818	.361
A3C	1.16	.738	3.18	2.00	2.91	2.22
A1D	.703	.406	.939	.626	1.87	.947
A2D	1.58	1.65	2.32	2.53	5.12	4.39
A3D	1.36	.515	2.00	.900	2.69	1.89
A1E	.773	.434	1.48	.861	1.51	1.06
A2E	.265	.187	.455	.227	.634	.401
A3E	.263	.180	.448	.278	.763	.430
A1F	.517	.408	.818	.687	1.07	1.16
A2F	.923	.460	1.85	.796	3.14	1.40
A3F	.710	.513	1.11	.742	1.51	1.02
A1G	.765	.396	.783	.574	.878	.835
A2G	.611	.457	1.35	.800	1.50	1.07
A3G	1.20	.523	3.42	2.17	2.31	1.48

(b) Interior Removed

TABLE 6. OVERALL FUSELAGE ACCELERATION LEVELS

TABLE 7. OVERALL ENGINE ATTACHED/ENGINE DETACHED ACCELERATION RATIOS

Accelerometer Positions	RESPONSE RATIO – ENGINE ATTACHED/ENGINE DETACHED					
	1680 rpm		1920 rpm		2160 rpm	
	Interior Installed	Interior Removed	Interior Installed	Interior Removed	Interior Installed	Interior Removed
A1A	4.45	4.14	4.17	3.78	4.37	3.53
A2A	1.72	2.33	1.53	1.54	2.16	1.69
A3A		1.45		1.53		1.00
A1B	1.10	1.45	1.41	1.95	0.96	1.20
A2B	2.05	2.03	2.49	1.49	1.90	1.54
A3B		2.74		2.40		2.13
A1C	2.27	2.52	1.64	2.07	2.78	2.03
A2C	2.92	3.43	2.82	3.39	2.61	2.27
A3C		1.57		1.59		1.31
A1D	1.41	1.73	1.18	1.50	1.24	1.97
A2D	0.96	0.96	0.78	0.92	0.80	1.17
A3D		2.64		2.22		1.42
A1E	1.40	1.78	0.874	1.72	0.841	1.42
A2E	1.73	1.42	1.53	2.00	1.316	1.58
A3E		1.46		1.61		1.77
A1F	1.83	1.27	1.78	1.19	1.15	0.92
A2F	1.23	2.01	1.67	2.32	1.22	2.24
A3F		1.38		1.50		1.48
A1G	0.70	1.93	1.55	1.36	1.71	1.05
A2G	1.92	1.34	1.38	1.69	1.36	1.40
A3G		2.29		1.58		1.56

Accelerometer Position	† ONE- THIRD OCTAVE BAND CENTER FREQUENCY, Hz																			% * OAAL	OAAL grms
	25	31.5	40	50	63	80	100	125	160	200	250	315	400	500	630	800	1000	1250	1600	2000	
A1A															2.090	1.600			1.160		82	3.51
A2A							0.578		0.460				0.353								71	1.16
A3A						0.476	0.738		0.458												99	1.12
A1B								1.190	2.670	1.030											88	3.52
A2B										0.204	0.236						0.191				60	0.609
A3B						0.359	0.320				0.213										74	0.708
A1C						1.110				0.765	0.542										89	1.640
A2C						0.300											0.277	0.503			79	0.818
A3C			1.710			1.421	0.890														82	2.910
A1D					0.406	1.170			0.937												85	1.820
A2D						3.510		2.010	1.670												85	5.120
A3D			1.280			0.804			1.250												73	2.69
A1E			0.683	0.486		0.816															77	1.510
A2E										0.235				0.304	0.246						72	0.634
A3E									0.373	0.277	0.296										72	0.763
A1F	0.386					0.326	0.296														54	1.020
A2F						1.800	1.480		1.500												88	3.140
A3F						0.640	0.894		0.640												84	1.510
A1G			0.343	0.423					0.289												70	0.878
A2G					0.480	1.08	0.486														85	1.500
A3G					1.180	1.720		0.421													92	2.310

† Only the three highest band levels are given to emphasize the spectrum peaks.

* Percent of overall rms acceleration level in the three highest bands given.

TABLE 8. ONE-THIRD OCTAVE BAND FUSELAGE ACCELERATION LEVELS
INTERIOR REMOVED - ENGINE ATTACHED - 2160 RPM

In summary, the analysis showed a clear dominance of low frequency structural response throughout the aircraft with panel response mainly following the propeller tones. As expected, fundamental panel resonances were excited when coincidence with engine 1/2 rpm harmonics occurred.

4. Engine Force and Vibration Levels

The rms axial force levels at each of the seven engine strut members were combined using a square root of the sum of the squares (SRSS) method to obtain an overall rms engine force level at each of the five engine test speeds. Likewise, the SRSS of the rms levels taken from the three accelerometers mounted on the engine block was taken to obtain a measure of the overall engine acceleration level. The interior reference microphone sound pressure level was also recorded during the engine force and acceleration runs. From these data the correlation plots given in Figure 24 were constructed. The line corresponding to the linear regression best fit to the data is shown for each of the plots along with the correlation coefficient, R. The correlation plots show the overall engine acceleration levels correlate (R = 0.89) to the noise levels at MIR much better than the overall axial force levels (R = 0.34). Note that the overall force levels do not necessarily increase with increasing rpm, whereas the engine acceleration levels show a definite increase with increasing rpm. This was attributed to structural resonances on the engine mount struts. For example, reference is made to the narrow band spectrum of Figure 13c, wherein a resonance in strut #1 around 220 Hz is clearly visible along with additional resonances at approximately 320 and 490 Hz.

One-third octave force levels in strut #1 for engine speeds 1920 and 2160 rpm are given in Figure 25. As can be seen, the engine strut forces are mainly concentrated in the lower frequency region of the spectra. The corresponding engine accelerations are given in Figure 26, wherein it can be seen that the spectra are dominated by high frequency contributions. Comparison of these engine force and acceleration spectra lead one to believe that the existing engine to engine mount vibration isolators are effective in the high frequency region and not very effective in the low frequency region. However, by examination of the structural-borne noise data, the isolators are apparently not as effective as the force spectra indicate.

The variation in the engine mount strut force levels at the various engine 1/2 rpm harmonics out to 200 Hz is shown in Figure 27. In general, the trend is decreasing strut force levels with increasing frequency, with the exception of the forces at the propeller tone, wherein a noticeable increase in level occurs for several of the strut members. Beyond 200 Hz, the levels decrease much slower with multiple spikes at resonances of the engine mount structure, reference Figure 13c.

IV. ANALYTICAL STRUCTURAL-ACOUSTIC MODEL

Methods for predicting interior noise levels due to structural-borne vibration and sidewall transmission in geometrically complex enclosures are not readily available (ref. 7), particularly in the low frequency region wherein the acoustic modal density is very low and methods of architectural acoustics do not apply. However, finite element acoustic methods have received considerable attention in the past few years for computing resonant frequencies of complex shaped enclosures with both hardwalled and flexible boundaries and in applications to reduce low frequency interior noise in automobiles (refs. 9,10,11,12,13, and 14). Both structural and acoustic finite element models were used in the present study. The equations of motion, methods of solution, and structural and acoustic model definitions used in this study are presented in this section. Reference is made to the work presented in Reference 15 for verification of the accuracy of the structural-acoustic coupling and analysis procedures presented herein.

A. Equations of Motion

The finite element method is well known for its application in structural analysis (ref. 16) and, therefore, no details of the structural finite element equations formulation will be given. However, some detail will be given to the acoustic volume representation to point out the importance of the coupling terms and the way in which they are preserved in the solution technique.

1. Structural Equations

In general, we may write the dynamic structural equations of motion in matrix form as

$$[M_S]\{\ddot{u}\} + [C_S]\{\dot{u}\} + [K_S]\{u\} = \{R\}, \tag{1}$$

where M_S, C_S, and K_S are the assembled nodal mass, damping, and stiffness matrices for the structure, and $\{u\}$ are the nodal degrees of freedom. The applied loads consist of two terms, namely:

$$\{R\} = [K_{SA}']\{P_S\} + \{F\}. \tag{2}$$

The first term in Equation (2) represents the applied forces due to the acoustic back pressure which is a function of the nodal surface pressures, $\{P_S\}$, and the second term, $\{F\}$, are the forces externally applied to the structure.

2. Acoustic Equations

The acoustic equations of motion are developed from the small perturbations source free wave equation (ref. 17)

$$\nabla^2 p - 1/c^2 \ddot{p} = 0 \tag{3}$$

where p is the perturbation pressure, c the speed of sound in the media, and ∇^2 is the Laplacian operator. On the boundaries of the acoustic region, the governing equations are subject to various boundary conditions:

(1) At a rigid boundary,

$$\partial p/\partial \eta = 0 \tag{4}$$

where η is the outward normal to the boundary;

(2) At a vibrating boundary,

$$\partial p/\partial \eta = -\rho_o \ddot{u} \tag{5}$$

where $\ddot{u}$ is the acceleration normal to the boundary and ρ_o the mean density of the acoustic media;

(3) At an absorptive boundary,

$$\partial p/\partial \eta = -\rho_o A(\omega) \dot{p} \tag{6}$$

where $A(\omega)$ is acoustic admittance of the boundary which is assumed to be frequency dependent and, therefore, implies that p exhibits a harmonic time dependence $(p = \overline{p} \exp(i\omega t))$.

If we expand the pressure in terms of a series of basis (shape) functions, we may write

$$p = \sum_{j=1}^{N} \phi_j P_j \tag{7}$$

where $\phi_j = \phi_j(x,y,z)$ characterizes the spatial dependence of p and $P_j = P_j(t)$, the temporal dependence.

Upon substitution of the assumed pressure series into the equations of motion, a distribution of errors results throughout the acoustic region due to the general nature and finiteness of the assumed pressure series. In accordance with the method of weighted residuals (ref. 18), we force the distribution of errors to be orthogonal within the region to each of the basis functions in the expansion. Thus,

$$\int_R \phi_i [\nabla^2 p - 1/c^2 \ddot{p}] \, dR = 0, \text{ for } i = 1,2,3...N. \tag{8}$$

By making use of Green's vector identity,

$$\phi_i \nabla^2(p) = -\nabla(\phi_i) \cdot \nabla(p) + \nabla \cdot \left(\phi_i \nabla(p)\right) \tag{9}$$

and the integral form of the divergence theorm of Gauss,

$$\int_R \nabla \cdot (\phi_i \nabla p) \, dR = \int_S \phi_i \nabla p \cdot \vec{\eta} \, dS \tag{10}$$

where R is the acoustic region, S its bounding surface, and $\vec{\eta}$ the outward normal to the region (ref. 19); the acoustic equations of motion become:

$$\frac{1}{c^2 \rho_o} \sum_{j=1}^{N} \int_R \phi_i \phi_j \, dR \, \ddot{P}_j +$$

$$\frac{1}{\rho_o} \sum_{j=1}^{N} \int_R \left\{ \frac{\partial \phi_i}{\partial x} \frac{\partial \phi_j}{\partial x} + \frac{\partial \phi_i}{\partial y} \frac{\partial \phi_j}{\partial y} + \frac{\partial \phi_i}{\partial z} \frac{\partial \phi_j}{\partial z} \right\} dR \, P_j$$

$$= \frac{1}{\rho_o} \int_S \phi_i \frac{\partial p}{\partial \eta} \, dS, \text{ for } i = 1,2,3...N. \tag{11}$$

The first term on the left is referred to as the acoustic mass, and the second term the acoustic stiffness, and the righthand side the applied boundary forces. Here we note that the constant $1/\rho_o$ has been added to the equations for purposes of dimensionality, and the term $\partial p/\partial \eta$ has not been expanded into its series form to allow direct substitution of the

boundary Equations (4) through (6). As can be seen for a hardwalled boundary, there are no applied forces, while for a vibrating boundary the applied forces are proportional to the boundary acceleration, and for an absorptive boundary the boundary forces appear as damping terms, i.e., proportional to $\dot{P}_j$. The above formulation of the acoustic equations of motion are valid for the entire acoustic region, R, or any subregions within R, or on its surface. Thus, we can see that by letting R represent the region of a single acoustic finite element and S the surface of that element, we may easily discretize the region into an assemblage of finite elements. Reference is made to the work of Zienkiewicz (ref. 16) for the various basis (shape) functions that can be used for the acoustic element generation, which are essentially the same as those used in the generation of structural finite elements.

The assembled matrix form of the acoustic equations of motion is:

$$\left[\begin{array}{c|c} M_A{}^{SS} & M_A{}^{SI} \\ \hline M_A{}^{IS} & M_A{}^{II} \end{array}\right] \left\{\begin{array}{c} \ddot{P}_S \\ \hline \ddot{P}_I \end{array}\right\} + \left[\begin{array}{c|c} C_A{}^{(\omega)} & 0 \\ \hline 0 & 0 \end{array}\right] \left\{\begin{array}{c} \dot{P}_S \\ \hline \dot{P}_I \end{array}\right\} +$$

$$\left[\begin{array}{c|c} K_A{}^{SS} & K_A{}^{SI} \\ \hline K_A{}^{IS} & K_A{}^{II} \end{array}\right] \left\{\begin{array}{c} P_S \\ \hline P_I \end{array}\right\} = \left[\begin{array}{c} -M_{AS} \\ \hline 0 \end{array}\right] \left\{\ddot{u}\right\} \qquad (12)$$

where M_A, C_A, and K_A are the acoustic mass, damping, and stiffness matrices, and M_{AS} is the inertia coupling associated with the boundary motion. The pressure nodal degrees of freedom are partitioned into those nodes on the surface, P_S, wherein damping or boundary motion is present and all other degrees of freedom are referred to as interior nodes, P_I.

B. Method of Solution

The structural equations of motion are reduced to modal form by expansion of the nodal displacements in terms of the structural normal mode eigenvectors (ref. 20). The system normal mode eigenvectors are determined from the undamped homogeneous equations

$$[M_S]\{\ddot{u}\} + [K_S]\{u\} = 0, \qquad (13)$$

via the equivalent linear eigenvalue problem

$$[K_S - \lambda M_S]\ \{u\} = \{0\}, \tag{14}$$

where $\lambda = \omega^2$, the square of the normal mode frequencies. The physical displacements are related to the modal degrees of freedom, q_S, via the eigenvectors, Q_S, as

$$\{u\} = [Q_S]\ \{q_S\}. \tag{15}$$

The eigenvectors are normalized such that they diagonalize the mass matrix to unity and the stiffness matrix to the square of the modal frequencies. The damping matrix is now chosen to be proportional to the system mass or stiffness and, therefore, also assumes a diagonal form. This procedure transforms the structural nodal equations into the modal form,

$$\begin{aligned}[\tilde{I}]\ \{\ddot{q}_S\} + [\tilde{2\beta\omega_S}]\ \{\dot{q}_S\} + [\tilde{\omega_S{}^2}]\ \{q_S\} \\ = [Q_S{}^T]\ [K_{SA}]\ \{p_S\} + [Q_S{}^T]\ \{F\}\end{aligned} \tag{16}$$

Here we note that for most practical problems, this modal expansion substantially reduces the number of structural equations since only those modal degrees of freedom whose normal mode frequencies lie within the analysis range of interest need to be retained. This method of reduction is commonly referred to as modal truncation or synthesis.

A direct expansion of the acoustic equations of motion in terms of the system normal cavity modes is not possible as was carried out for the structural equations. Since the normal mode expansions with $\partial p/\partial \eta = 0$ on the boundary would not allow representation of system absorption or forced vibration, these inputs require non-zero boundary motion. However, in many problems the number of interior nodes plus surface nodes with negligible absorption or motion can be large as compared to those surface nodes that exhibit significant motion or absorptive capability. For these cases it would be advantageous to expand those interior nodes and surface nodes for which $\partial p/\partial \eta = 0$ into modal form and apply modal truncation to reduce the number of active degrees of freedom in the acoustic equations of motion.

This is accomplished by seeking a transformation that will stiffness decouple the two coordinate sets. This transformation is

$$\begin{Bmatrix} P_S \\ \hline P_I \end{Bmatrix} = \left[\begin{array}{c|c} I & 0 \\ \hline T & I \end{array}\right] \begin{Bmatrix} P_S \\ \hline \hat{P}_I \end{Bmatrix} \tag{17}$$

where

$$[T] = -[K_A{}^{II}]^{-1} [K_A{}^{IS}]. \tag{18}$$

The vectors of the transformation to the left of the partition are component modes of contraint. They represent the pressure perturbations at P_I when the constraint nodes P_S are individually given a unit pressure perturbation. It is to be noted that the node set P_I has been replaced with the set $\hat{P}_I$ which denotes the pressure perturbation of P_I when $P_S = 0$.

Substituting the transformation given in Equation (17) into the acoustic Equation (12) while simultaneously conserving system energy, results in the following equations of motion:

$$\left[\begin{array}{c|c} W_A{}^{SS} & W_A{}^{SI} \\ \hline W_A{}^{IS} & M_A{}^{II} \end{array}\right] \begin{Bmatrix} \ddot{P}_S \\ \hline \ddot{\hat{P}}_I \end{Bmatrix} + \left[\begin{array}{c|c} C_A(\omega) & 0 \\ \hline 0 & 0 \end{array}\right] \begin{Bmatrix} \dot{P}_S \\ \hline \dot{\hat{P}}_I \end{Bmatrix} +$$

$$\left[\begin{array}{c|c} S_A{}^{SS} & 0 \\ \hline 0 & K_A{}^{II} \end{array}\right] \begin{Bmatrix} P_S \\ \hline \hat{P}_I \end{Bmatrix} = \begin{bmatrix} -M_{AS} \\ \hline 0 \end{bmatrix} [Q_S] \{\ddot{q}_S\} \tag{19}$$

where

$$W_A{}^{SS} = M_A{}^{SS} + T^T M_A{}^{IS} + M_A{}^{SI} T + T^T M_A{}^{II} T,$$

$$W_A{}^{SI} = (W_A{}^{IS})^T = M_A{}^{SI} + T^T M_A{}^{II},$$

and

$$S_A{}^{SS} = K_A{}^{SS} + T^T K_A{}^{IS}. \tag{20}$$

Here we note that the acoustic interior nodal mass and stiffness submatrices $M_A{}^{II}$ and $K_A{}^{II}$, and surface damping matrix $C_A(\omega)$, remain unchanged under this transformation and the degrees of freedom P_S and $\hat{P}_I$ have been stiffness decoupled. The applied loads due to boundary motion also remain unchanged.

With the equations of motion in this form, we can again make use of the concept of modal truncation by extracting the eigenvalues and eigenvectors

for the subvolume consisting of the coordinate set $\hat{P}_I$ when it is subject to the constraint conditions, $P_S = 0$. The resulting homogeneous equations of motion corresponding to this condition are

$$[M_A{}^{II}] \{\ddot{\hat{P}}_I\} + [K_A{}^{II}] \{\hat{P}_I\} = \{0\} \tag{21}$$

which has an associated linear eigenvalue problem of the same form as that given in Equation (14) for the structural equations. Solution to the eigenvalue problem yields an associated set of eigenvectors or mode shapes

$$\{\hat{P}_I\} = [Q_A] \{q_A\} \tag{22}$$

normalized such that

$$Q_A{}^T M_A{}^{II} Q_A = I \quad \text{and} \quad Q_A{}^T K_A{}^{II} Q_A = \omega_A{}^2 \tag{23}$$

where $\omega_A{}^2$ denotes a diagonal matrix of the squares of the circular frequencies arranged in an increasing order of magnitude. At this point we may truncate the number of eigenvalues to be retained for representation of the subvolume. The number of modes retained in the expansion can generally be set to less than 30% of the original degrees of freedom set, thereby substantially reducing the total order, or degrees of freedom, of the system.

The reduced equations of motion for the coupled structural-acoustic system are

$$\begin{bmatrix} I & 0 & 0 \\ M_{AS}Q_S & W_A{}^{SS} & W_A{}^{SI} Q_A \\ 0 & Q_A{}^T W_A{}^{IS} & I \end{bmatrix} \begin{Bmatrix} \ddot{q}_S \\ \ddot{P}_S \\ \ddot{q}_A \end{Bmatrix} + \begin{bmatrix} 2\beta\omega_S & 0 & 0 \\ 0 & C_A(\omega) & 0 \\ 0 & 0 & 0 \end{bmatrix} \begin{Bmatrix} \dot{q}_S \\ \dot{P}_S \\ \dot{q}_A \end{Bmatrix} + \begin{bmatrix} \omega_S{}^2 & -Q_S{}^T K_{SA} & 0 \\ 0 & S_A{}^{SS} & 0 \\ 0 & 0 & \omega_A{}^2 \end{bmatrix} \begin{Bmatrix} q_S \\ P_S \\ q_A \end{Bmatrix} = \begin{Bmatrix} Q_S{}^T F \\ 0 \\ 0 \end{Bmatrix} \tag{24}$$

where the structural nodal motion is found from the expression given in Equation (15), the interior nodal pressures determined from

$$\{P_I\} = [T]\ \{P_S\} + [Q_A]\ \{q_A\} \tag{25}$$

and the surface pressures are directly P_S. The equations of motion in symmetric form are

$$\begin{bmatrix} \omega_S^2 & 0 & 0 \\ 0 & W_A^{SS} & W_A^{SI}\ Q_A \\ 0 & Q_A^T W_A^{IS} & I \end{bmatrix} \begin{Bmatrix} \ddot{q}_S \\ \ddot{P}_S \\ \ddot{q}_A \end{Bmatrix}$$

$$+ \begin{bmatrix} 2\beta_S\omega_S^3 & 0 & 0 \\ -B^T[2\beta_S\omega_S^2] & C_A(\omega) & 0 \\ 0 & 0 & 0 \end{bmatrix} \begin{Bmatrix} \ddot{q}_S \\ \ddot{P}_S \\ \ddot{q}_A \end{Bmatrix}$$

$$+ \begin{bmatrix} \omega_S^4 & -[\omega_S^2]B & 0 \\ -B^T[\omega_S^2] & S_A^{SS} + B^T B & 0 \\ 0 & 0 & \omega_A^2 \end{bmatrix} \begin{Bmatrix} q_S \\ P_S \\ \ddot{q}_A \end{Bmatrix}$$

$$= \begin{bmatrix} \omega_S^2 \\ -B^T \\ 0 \end{bmatrix} \left\{ Q_S^T F \right\} \tag{26}$$

where $B = Q_S^T K_{SA}$ and is referred to as the coupling matrix.

The <u>hardwall</u> acoustic modes are the normal mode eigenvectors of the undamped homogeneous equations;

$$\begin{bmatrix} W_A^{SS} & W_A^{SI}\ Q_A \\ Q_A^T W_A^{IS} & I \end{bmatrix} \begin{Bmatrix} \ddot{P}_S \\ \ddot{q}_A \end{Bmatrix} + \begin{bmatrix} S_A^{SS} & \\ & \omega_A^2 \end{bmatrix} \begin{Bmatrix} P_S \\ q_A \end{Bmatrix} = \begin{Bmatrix} 0 \end{Bmatrix} \tag{27}$$

and the coupled structural acoustic modes are the normal mode engenvectors of the undamped homogeneous equations;

$$\begin{bmatrix} \omega_S^2 & 0 & 0 \\ 0 & W_A^{SS} & W_A^{SI} Q_A \\ 0 & Q_A^T W^{IS} & I \end{bmatrix} \begin{Bmatrix} \ddot{q}_S \\ \ddot{P}_S \\ \ddot{q}_A \end{Bmatrix}$$

$$+ \begin{bmatrix} \omega_S^4 & -[\omega_S^2]B & 0 \\ -B^T[\omega_S^2] & S_A^{SS} + B^T B & 0 \\ 0 & 0 & \omega_A^2 \end{bmatrix} \begin{Bmatrix} q_S \\ P_S \\ q_A \end{Bmatrix} = \begin{Bmatrix} 0 \\ 0 \\ 0 \end{Bmatrix} \qquad (28)$$

We can see that the strength of the coupling matrix B determines the degree of structural-acoustic coupling in the system; as B = 0, the equations completely decouple. In the case of low frequency noise generation, the acoustic absorption of the aircraft interior trim is generally frequency independent or negligibly small in which case the absorptive term $C_A(\omega)$ may be set equal to a constant or to zero. For this case, we may expand the damped inhomogeneous equations in terms of the coupled structural-acoustic modes obtained from Equations (28). The solution of the eigenvalue problem corresponding to Equation (28) results in an associated set of eigenvectors

$$\begin{Bmatrix} q_S \\ P_S \\ q_A \end{Bmatrix} = \begin{bmatrix} \psi \end{bmatrix} \{\gamma\} = \begin{bmatrix} \psi_{SS} \\ \psi_{AS} \\ \psi_{AA} \end{bmatrix} \{\gamma\}. \qquad (29)$$

The expanded form of the damped inhomogeneous system of equations becomes

$$[I]\ \{\ddot{\gamma}\} + [C_{SA}]\ \{\dot{\gamma}\} + [\omega^2_{SA}]\ \{\gamma\} = \{F\} \qquad (30)$$

where C_{SA} is the generalized damping matrix and

$$\{F\} = [\psi^T] \begin{bmatrix} \omega_S^2 \\ B^T \\ 0 \end{bmatrix} \{Q_S^T F\} \qquad (31)$$

are the generalized externally applied forces. The generalized damping matrix has the form

$$\left[C_{SA}\right] = \left[\psi^T\right] \begin{bmatrix} \ddots\ 2\beta_S\omega_S{}^3 & \vdots & \\ \cdots\cdots & \cdots & \cdots\cdots \\ -B^T[\ddots 2\beta_S\omega_S\ddots] & \vdots & C_A \end{bmatrix} \left[\psi\right] \tag{32}$$

where it can be seen that when $C_A = 0$, there still exists a damping coupling between the structural degrees of freedom and acoustic degrees of freedom.

In the present investigation, two methods of damping representation are used. In Method 1, the damping matrix is assumed to be diagonalized by the coupled eigenvector such that

$$\left[C_{SA}\right] = \left[2\beta\omega_{SA}\right] \tag{33}$$

where β_{SA} are the coupled mode critical damping ratios. This representation has the computational advantage of completely diagonalizing the inhomogeneous system of equations. The resulting solution appears as a series of damped uncoupled single degree of freedom oscillators. The solution of the r-th degree of freedom for a forced harmonic input is

$$Y_r = \frac{\bar{F}_r\ (\omega)}{(\omega^2{}_{SA} - \omega^2) + i\ 2\beta\ \omega_{SA}\ \omega} \tag{34}$$

This approximation has been shown to be most appropriate for lightly damped systems (ref. 15). However, it requires knowledge of the coupled mode critical damping ratios.

In Method 2 it is assumed that only the structural mode critical damping ratios are known and that no acoustic absorption is presnet, i.e., $\beta = \beta_S$ and $C_A = 0$. This approximation results in a frequency dependent nondiagonal generalized damping matrix, for which a frequency by frequency solution of Equation (30) is required. The importance of the second method of representation is that only through system coupling to the structure do dominant acoustic responses maintain finite amplitudes. Analyses presented in Section V will compare the usefulness of these different damping representations.

C. Structural Finite Element Model

A structural finite element model of the Cessna Model 172 test aircraft was developed based on the structural data found in References 21 and 22, and physical measurements taken directly on the aircraft. Detailed structural

drawings of the aircraft were not available. The primary aircraft carry-through structure is provided by the channel stiffened double floor and the forward and aft door frames. The Model 172 primary fuselage structure is shown in Figure 28. The skin thickness of the various fuselage panels are shown in Figure 29. Due to the symmetry of the fuselage, a symmetric half-plane model was sufficient to represent the structure. The aircraft was modeled using three dimensional beam elements for the primary fuselage structure and shell elements for the fuselage skin panels. Various lumped masses were employed to represent nonstructural fuselage members. These included the battery, fuel system, rudder controls, instrumentation, landing gear, J-box, tail cone end fixture, and miscellaneous cables and pulleys.

Rather than attempt to model all localized plate motion, only those panel sections which were found to produce significant responses during the modal sweep tests were modeled in detail. The analysis range of primary interest in this initial investigation was just past the second propeller tone or out to approximately 150 Hz. It was determined that the following panel regions were of primary importance:

(1) Tail cone side panels
(2) Doors
(3) Cabin roof
(4) Side windows and windshield
(5) Rear cabin side panels.

These modeling considerations resulted in a finite element model consisting of 146 nodes, 165 beam elements, 200 shell elements, 20 lumped masses, and 767 dynamic degrees of freedom. The model was generated using EASE2 a finite element structural program maintained by Engineering Analysis Corporation and accessed through McDonnell Douglas Automation Company. The structural finite element model of the fuselage showing the beam element distribution and complete structure is given in Figure 30. By comparison of the fuselage assembly views shown in Figure 28 and the finite element model given in Figure 30, the level of attention to structural detail on the model can be assessed. All modeling inputs were generated in the conventional aircraft construction English system of units.

The half fuselage modeled weight was 1009.7 N (227 lb_f) with a center of gravity location at Body Station 48.4, Butt Line 0.0, and Water Line -2.7. The aircraft engine and engine mount, weighing approximately 1779 N (400 lb_f), was not included in this model.

Results from a dynamic analysis of the model and comparisons to laboratory measured responses are given in Section V.

D. Acoustic Finite Element Model

Two finite element acoustic models of the fuselage were developed; a full fuselage model which physically occupied the volume prescribed by the structural symmetric half-plane model, and a cabin-only model which considered the interior bulkhead at Body Station 108 to be rigid thereby terminating at that point. Many of the surface acoustic node points were coincident with the structural nodes. The basic division of acoustic nodes followed the structural model shown in Figure 30b. In Figure 31, the distribution of acoustic node points at major fuselage stations are given to indicate the density of acoustic interior node points within the fuselage. The acoustic model consisted of a total of 124 surface nodes and 74 interior nodes throughout the half-plane model. In the full fuselage model, 90 of the surface nodes were considered elastically active. The remainder of 108 were considered stationary. The model had a total of 9.16 $meter^2$ (14,200 $inch^2$) of surface area of which 5.88 $meter^2$ (9,111 $inch^2$), or approximately 64%, was considered active in the structural acoustic coupled fuselage model. Out of the 5.88 $meter^2$ of active area, 1.59 $meter^2$ (2,465 $inch^2$) occupied the side wall surface of the tail cone aft of B.S. 108. The acoustic model parameters are summarized in Table 9, and a summary of the active panel areas in the structural-acoustic model is given in Figure 32.

The acoustic finite element analysis program used to develop the acoustic models and carry out the coupling and solution procedures required for this investigation was developed at Southwest Research Institute under an internally funded program, SwRI Project 02-9193. The software was limited in representation to 150 dynamic degrees of freedom which limited the acoustic model definition. Through the use of an acoustic subvolume analysis technique (ref. 15), the software could, however, accommodate a total of 200 acoustic nodal degrees of freedom.

TABLE 9. ACOUSTIC MODEL PARAMETERS

	Digital Computer Code	Cabin Only	Full Fuselage
No. of Nodes	NAN	124	198
No. of Active Surface Nodes	NSN	61	90
No. of Interior Nodes	NIN	63	108
No. of Acoustic Elements	NAE	80	124
No. of Active Surface Elements	NSE	77	106

V. COMPARISON OF ANALYTICAL AND EXPERIMENTAL RESULTS

In the sections to follow, predicted results from the fuselage structural and acoustic models, described in Section IV, will be compared to the experimental data given in Section III. The primary objective of the data comparisons is to demonstrate modeling requirements for predicting structural-borne noise in a lightweight, single engine aircraft structure.

A. Resonant Frequencies and Mode Shapes

Thirty-six elastic modes were retained from an eigenvalue analysis of the fuselage finite element structural model described in Section IV.C. The aircraft rigid body support frequencies were sufficiently low (below 11 Hz) such that they were decoupled from the aircraft elastic response. These modes were not retained in the model. A comparison of the resulting modal frequencies and experimentally determined frequencies is given in Table 10. As can be seen, the predicted frequencies are in quite good agreement with the measured responses. The predicted responses at 104 and 112 Hz could not be identified with any particular part of the structure; however, they are not fuselage bending modes. The primary fuselage vertical bending modes were predicted to be at 56.4 and 119 Hz. The first vertical bending response precisely agreed with the measured response. Higher fuselage bending mode responses were not identified in the laboratory. Panel responses up through 100 Hz also compared well to measured values.

The structural modal density of the aircraft is shown in Figure 33. The computed modal density for the modeled range, up to 150 Hz, is shown to be 0.3 mode/Hz while thereafter a falloff occurs to a density of 0.15 mode/Hz. Recall that in the generation of the model, panels were modeled only for responses up to approximately 150 Hz. Due to the lack of representation in the nodal degrees of freedom in the model, the density in higher modal responses falls off as indicated in the modal density plot. The fuselage high structural modal density limited the analysis to 32 elastic modes, or an upper frequency range of 200 Hz. While modes up to 200 Hz are included in the analysis, it is to be noted that a lack of representation exists in the frequency range above 150 Hz. We can see from the plot given in Figure 33 that a finite element model representation of the aircraft for modal responses beyond 200 Hz may well become impractical, and other less deterministic modeling approaches may need to be employed.

TABLE 10. COMPARISON OF PREDICTED AND MEASURED FUSELAGE FREQUENCIES.

Mode No.	Location, Description	Analytical Freq. (Hz)	Experimental Freq. (Hz)
1	A1F, Lower Door Panel	26.6	30
2	A3D, Tail Cone Side @ Station 160.0	39.3	44
3	A3C, Tail Cone Side @ Station 124.0	41.9	44
4	A1E, Door Window	42.1	45
5	Vertical Bending	56.4	56.4
6	A1G, Side Window @ Station 76.9	61.5	60
7	A1E & A1F, Door	67.9	(63)*
8	A2F, Roof @ Station 76.9	72.9	73
9	A2F, Roof @ Station 76.9	76.0	73
10	A2D, Roof @ Station 50.4	81.4	80
11	A2G, Side Panel @ Station 76.9	82.5	(80)
12	A3A, Side Panel @ Station 98.3	95.4	(100)
13	A3F, Tail Cone Top @ Station 160.0	100	(90)
14		104	
15	A2F, Roof @ Station 76.9	108	98
16		112	
17	A3D, Tail Cone Side @ Station 160.0	115	(125)
18	Vertical Bending	119	
19	A3A, Side Panel @ Station 98.3	123	(100)
20	A3G, Tail Cone Bottom @ Station 160.0	129	
21	A3G, Tail Cone Bottom @ Station 160.0	129	
22	A1B, Firewall	132	(125,160)
23	A3D, Tail Cone Side @ Station 160.0	145	(160)
24	A1E & A1F, Door	149	
25	A3A, Side Panel @ Station 98.3	153	

* ( ) Center frequencies of the 1/3 Octave Band Spectral Distribution of Accelerometer Peak Response.

MODE DENSITY 0.17 MODES/HZ BEYOND 150 HZ

Acoustic hardwalled modes were computed for both the cabin-only and full fuselage acoustic models. Frequencies and cabin centerplane node line plots are given in Figures 34 and 35. The fundamental cabin-only hardwalled mode was computed to be 71.6 Hz as compared to 62.0 Hz measured in the laboratory (ref. Table 2) for the cabin with the rigid bulkhead at B.S. 108. Likewise, the full fuselage fundamental responses were predicted to be 40.0 and 72.7 Hz, while laboratory results showed responses at 35.0 and 64.0 Hz for the interior removed configuration. As expected, the frequencies were higher than the measured results which is attributed to the hardwalled boundary assumption.

The effect of wall flexibility on the predicted cabin-only modal responses can be seen by comparison of the hardwall modes given in Figure 34 to the coupled structural-acoustic responses given in Figure 36. All computed coupled mode responses exhibit structural-acoustic coupling to some degree. However, by examination of the node line plots we can see that the fundamental acoustic cabin resonance dropped from 71.6 Hz in the hardwalled model to 66.0 Hz in the coupled model. Likewise, in the full fuselage coupled model prediction, given in Figure 37, the fundamental acoustic responses dropped from 40.0 and 72.7 Hz, to 31.6 and 68.9 Hz when wall flexibility was taken into account. A summary listing of predicted normal mode frequencies is given in Table 11. Examination of this data with comparison to the measured responses given in Table 2 clearly show that including wall flexibility improved agreement between predicted and measured results.

B. Transfer Functions

Forced harmonic sweep data were obtained in the laboratory as described in Sections II.B. Typical data results were given in Section III.A.3. These data form the base for comparisons to analytically predicted forced harmonic response calculations using the previously described normal mode models of the aircraft.

The sweep tests were performed by exciting the aircraft, in the longitudinal direction, individually at each of the four motor mount-to-fuselage attach points with a constant 88.96N (20.0 lbs) rms force. For the purpose of comparison of results to the symmetric half-plane model, the unsymmetric test configuration was modeled as a sum of a symmetric and antisymmetric configuration as shown in the following sketch. For comparison of interior noise levels,

TABLE 11. SUMMARY OF PREDICTED NORMAL MODE FREQUENCIES

Mode No.	HARDWALLED MODES		ENGINE DETACHED		
	Cabin	Fuselage	Structure Alone	Cabin + Structure	Fuselage + Structure
1	71.6	40.0	26.61	28.04	25.40
2	131.5	72.7	39.26	39.25	31.61
3	160.5	104.1	41.95	41.94	40.07
4	188.0	138.0	42.16	42.46	42.89
5	222.8	159.0	56.38	56.37	52.13
6	234.5	178.5	61.52	57.91	56.76
7	284.2	197.2	67.86	66.01	60.67
8	304.9	229.9	72.92	68.27	67.48
9	327.3	236.0	75.98	73.44	68.94
10			81.37	77.01	73.22
11			82.52	80.67	77.04
12			95.40	83.84	79.93
13			100.46	96.42	83.79
14			103.91	100.69	96.46
15			107.65	103.41	99.86
16			112.49	108.17	103.22
17			115.47	112.08	104.93
18			119.10	115.44	109.32
19			123.13	117.13	112.31
20			128.69	121.48	114.97
21			129.27	128.06	117.93
22			132.16	129.07	122.06
23			144.84	132.16	128.43
24			148.87	134.81	129.38
25			152.99	144.68	132.16
26			158.74	148.44	141.08
27			170.83	152.35	145.76
28			176.74	156.82	148.36
29			189.49	163.30	152.73
30			191.10	171.55	157.43

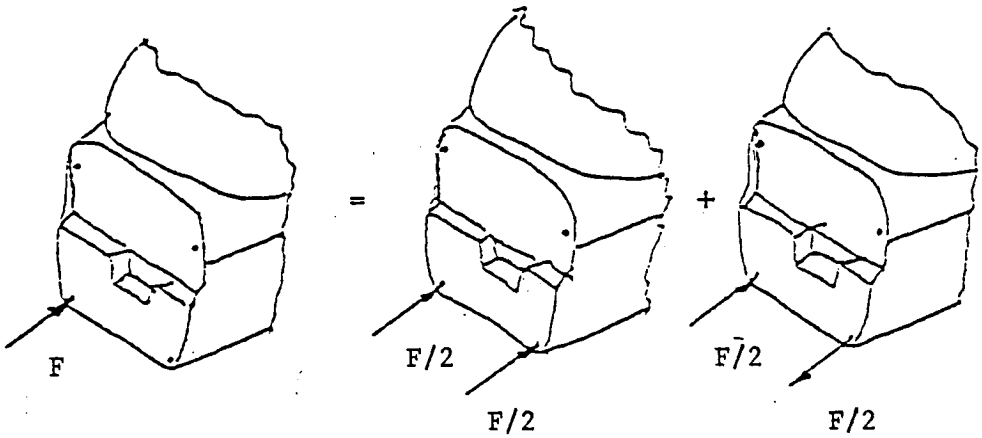

Unsymmetric Symmetric Antisymmetric

the antisymmetric configuration theoretically should not participate until the first transverse cabin mode becomes active; this would be around 160 Hz.

Since laboratory data were obtained while driving at both right and left side engine mount attach point locations, the laboratory data were combined to yield the maximum response in either of the driving positions. Interior responses were measured at several locations near the pilot's normal head position. These microphone responses were similarly combined to yield a maximum response. Thus, the data used in the following comparisons represent maximum expected responses. Likewise, in the analytical model results, large variations in interior SPL due to location of modal node lines were eliminated by obtaining the maximum response from three interior microphone locations. The three locations are denoted in the node line plots given in Figure 36. The predicted fuselage acceleration responses are taken at model nodes nearest to the measured response location.

The following nomenclature is used to denote the various input locations, output responses, and models used in the forced harmonic response results.

(1) - Lower engine-to-fuselage attach point, longitudinal direction.

(2) - Upper engine-to-fuselage attach point, longitudinal direction.

A2E - Acceleration response aft door frame vertical, top center of cabin.

A1F - Acceleration response center lower door panel, lateral

MIR - Maximum SPL in area of pilot's head position, maximum of nodes 35, 53, and 74 (see Figure 36).

E - Experimental results

SA - Structure alone, modal damping $\beta_S = 0.02$, no acoustic coupling.

CF - Full fuselage coupled structural acoustic model, $\beta_{SA} = 0.02$ if not so stated.

CC - Cabin only coupled structural acoustic model, $\beta_{SA} = 0.02$ if not so stated.

In the majority of the forced harmonic response calculations discussed in this section, the damping approximation used is Method #1, reference Equation (33) of Section IV.B. The nominal critical damping ratio was chosen to be $\beta_{SA} = 0.02$ and was applied to all coupled modes. Limited results using the coupled damping matrix approach, denoted as Method #2, are also presented. In Method #2, critical damping ratios are applied to only the structural mode responses and structural-acoustic coupling distributes damping throughout the system. This latter method of damping representation requires approximately ten (10) times the computational effort over that of the diagonal damping matrix approximation.

Typical comparisons of predicted versus measured forced harmonic fuselage acceleration responses, while driving the fuselage in the longitudinal direction with 44.48N (10.0 lbs) rms force at the lower and/or upper engine mount attach points, are given in Figures 38 through 40. Effectively, the driving point impedances of the fuselage upper and lower engine mount attach points are given in Figure 38. By comparison of the curves marked E for Experimental and SA for Structure-Alone responses, we see that the responses at the driving point indicate that the fuselage local stiffness is much less than that represented in the structural model. However, responses at major frame members such as at the aft door frame location, A2E, are in much better agreement as is shown in Figure 39. Responses at the center door panel are given in Figure 40. Here we see that increased compliance of the panel would be necessary for better agreement between measured and predicted responses.

In Figures 38 through 40, the curves marked CF correspond to the predicted fuselage response when employing the coupled fuselage model. As can be seen, the acoustic volume does not appreciably affect the driving point response; however, it does add measurable compliance to frame and panel responses in the lower frequencies.

In Figure 41, a comparison of predicted to measured sound pressure level responses near MIR are given for the coupled fuselage, CF, and coupled cabin, CC, models. For input at the fuselage lower engine mount attach point, reference Figure 41a, both models tend to be conservative in the 50 through 80 Hz and 160 through 200 Hz range, and nonconservative in the 100 to 150 Hz range. As expected, the full fuselage model supports a lower frequency response while the cabin-only model exhibits very little response below 40 Hz. Driving at the upper engine mount attach point, reference Figure 41b, shows the models, in general, to be nonconservative, except within narrow resonant bands out to 150 Hz; thereafter a slight conservatism exists.

In general, the comparison of predicted to measured transfer functions of fuselage acceleration and interior SPL response indicates that an improvement in the model is desirable for a conservative analysis. Close examination of the trends of predicted to measured responses, excluding the driving point accelerations, indicate physically consistent trends, i.e., a low SPL response corresponds to low fuselage acceleration responses. One way to alter the system response is to change system damping; however, system damping generally only controls resonant response, which is the case for the present system. This can be seen by the data given in Figure 42, wherein predicted SPL responses at fixed node 35, for damping values of $\beta_{SA} = 0.01$ and 0.02 are given. As can be seen, for a factor of two decrease in damping, a corresponding increase in SPL response of approximately 6 dB occurs at each of the system resonances. However, note that by comparison of the predicted to measured trends shown in Figure 41, adjusting the coupled mode damping values of the various modes would not result in consistent improvements in response at both of the driving point inputs.

To validate the diagonal damping representation, Method #1, with respect to the more exact representation of a coupled damping matrix, Method #2, the responses presented in Figure 43 were generated. In Figure 43, the curve marked CC-1 is the response for a diagonal damping matrix for $\beta_{SA} = 0.02$, and

the curve marked CC-2 is the predicted response for the coupled damping matrix wherein only the structural responses are assigned a damping value, $\beta_S = 0.02$. We see that from these predictions, structural damping alone controls the lower frequency region due to structural-acoustic coupling. Above, say 120 Hz, the coupling is not as strong and responses begin to increase. Thus, it appears that the diagonal damping representation is valid for the low frequency region.

From the system resonant frequency and transfer function data comparisons, it was concluded that the modeling procedures employed were correct, and to further improve the correspondence between measured and predicted results would require increasing both the structural definition of the fuselage and increasing the nodal definitions of the acoustic volume. This could have been accomplished with additional expansion of the analysis software and at considerable additional computational expense; however, it was felt that the degree of correlation obtained with the present model was sufficient to allow further numerical investigation using the measured engine forces.

C. Engine Alone Contributions

The measured engine mount strut forces at each engine 1/2 rpm harmonic out to 200 Hz were given in Figure 27 for an engine speed of 2160 rpm. Similar levels were recorded at the lower engine speeds as well. Symmetric fuselage input forces were calculated from the measured engine strut forces and the known engine mount geometry (ref. Cessna Aircraft Drawing No. 0551014). A plot of the force components for engine speeds of 1920 and 2160 rpm are given in Figure 44. The subscript 1 denotes the lower engine mount attach point, and 2 the upper engine mount attach point. Forces in the longitudinal direction are subscripted with an x, and in the vertical direction with a z. In the analysis, the force components F_{x_1}, F_{z_1}, F_{x_2}, and F_{z_2} were applied individually to the fuselage model. The total interior response was then computed using the SRSS (square root of the sum of the squares) method, Thus,

$$SPL_T = 10. * \log_{10} \left(\sum_{i=1}^{4} 10^{(SPL_i/10)} \right)$$

where SPL_i is the interior response due to one of the four load cases, and SPL_T is the total expected response. The engine mount forces were applied to the cabin-only model and the results compared to the measured engine-alone

mean one-third octave level results. The predictions were converted to one-third octave responses by direct addition of all tones residing in a given one-third octave band, while responses occurring at the band limits were split evenly into the adjacent bands.

In Figure 45 model results using the engine driving forces are compared to measured results at an engine speed of 1920 rpm. Predicted sound pressure levels at MIR are shown for damping on all coupled modes set at $\beta_{SA} = 0.01$ and $\beta_{SA} = 0.02$, and for $\beta_S = 0.01$ assigned to only the structural modes while using the more elaborate damping coupling analysis method. In the measured results, given by the bar levels, acoustic cabin resonances give rise to the high response in both the 31.4 and 63 Hz bands since the bare fuselage exhibited fundamental acoustic resonances at 35.0 and 64.0 Hz. Recall that for the interior installed configuration, the lower resonance was highly damped, reference Table 2, which is reflected in the larger difference in the interior installed and interior removed measured responses (note the solid line denotes the interior removed level and the dashed line the interior installed level). We see that these resonant conditions are not displayed in the predicted levels; however, one should not expect the lower resonance to exist in the cabin-only model. The predicted cabin-only model first acoustic resonant mode occurred at 71.6 Hz for the hardwalled cabin and dropped to 66.0 Hz for the coupled response. Thus, we should expect a resonant condition in the model for an equivalent engine speed of 1980 rpm. The data given in Figure 46 confirms the resonant condition wherein additional predictions are given for the 1980 and 2040 rpm conditions. For these results the engine force levels at 1920 rpm were used as inputs and only the spectral content was shifted to appropriately account for the shift in engine rpm.

Predicted results for the 2160 rpm condition are given in Figure 47. The predicted levels in the 50 Hz band appear to belong to the 63 Hz band; however, this is not the case. First, the response at the propeller tone (at 72 Hz) experimentally shows up in both the 63 Hz and 80 Hz bands due to small fluctuation in engine speed since the band limit between the 63 Hz and 80 Hz bands is at 70.8 Hz. If we combine the levels in these two bands, an increase of approximately 1 dB would result. Second, the predicted response in the 50 Hz band is due to excitation of the 56.4 Hz engine detached structural bending mode. The predicted acoustic response due to excitation of the

fuselage bending mode shows the model to be highly conservative. This is attributed to the failure of the analytical model to completely cancel apparent "rigid body" motion between active floor and roof panels.

In general, the one-third octave predictions for the sound pressure levels at MIR are in good agreement with the measured results. Basically, the predictions tend to be somewhat nonconservative in the lower frequencies and conservative in the higher frequencies. However, based on these results, it was felt taht the model sufficiently well represents the physical system to allow preliminary noise control investigations.

VI. NOISE CONTROL MEASURES

Structural-borne noise control for the test aircraft in the low frequency region of interest in the present investigation would be most likely best accomplished by modification at the source. However, program funds available during this initial effort would not allow detailed evaluation of the engine mount dynamics. However, initial investigations into the effects of modal damping and contributions of various fuselage panels have been carried out. A thorough evaluation of structural-borne noise control measures for the test aircraft is the subject of a continuation effort.

A. Effect of Modal Damping

From the data presented in Figure 44, it appears that a factor of two decrease in modal damping results in an increase in interior response of approximately 6 dB at the various system resonances. To what degree a change in modal damping would affect interior noise levels in the test aircraft will depend on the spectral content of the source. If the source harmonics coincide with many of the coupled system resonances, damping would play an important role in noise control.

By examination of the data presented in Figures 45 through 47, the effect of reducing the damping from $\beta_{SA} = 0.02$ to $\beta_{SA} = 0.01$ on the interior sound pressure levels at MIR can be seen. The resulting change in SPL in each of the one-third octave analysis bands are given in Figure 48 for analyses at engine speeds of 1920, 1980, and 2160 rpm. The data for the 1920 and 1980 rpm configurations use the measured forces taken at the 1920 rpm condition with appropriate adjustment in spectral content to reflect the change in engine rpm. Recall that in the 1980 rpm configuration a resonant condition in the 63 Hz band occurred wherein the fundamental cabin acoustic mode was highly excited (ref. Figure 46). This accounts for the 6.1 dB change in SPL in the 63 Hz band at 1980 rpm and also for the apparently odd behavior of the response in the adjacent 80 Hz, which shows a decrease in response of 1.8 dB for a decrease in damping. In this case, the cabin resonance at 66 Hz was strong enough to control response out into adjacent bands where an increase in peak response resulted in a narrowing of the response thereby decreasing sideband levels. The data at 1920 rpm in the 100 and 125 Hz bands indicate that response in these bands are also controlled by system resonance. The mean of the data show the change

in response to gradually increase with increasing frequency to approximately the 6 dB level. This trend appears to be the result of increased modal density in the higher frequencies which gives rise to increased source coalescence with system resonances.

B. Contributions of Various Panel Groups

The cabin-only model was used to investigate the sensitivity of interior noise levels to various panel groups in the aircraft. In this investigation it was assumed that the structural compliance of the fuselage remained unchanged while various panel sections were individually activated. Mathematically, this required altering the coupling matrix B (reference Equation (28), Section IV.B) to allow coupling motion only for the active panel group of interest; effectively all other panels were then rigid. Reference is made to Figure 32 for the respective areas of the floor, roof, door, and aft side panel groups used in this investigation. The areas of the panel groups varied from 1.02 meter^2 to 1.15 meter^2.

Separate coupled cabin models were generated with the four panel groups individually active. A summary of the first twenty coupled mode frequencies are given in Table 12. By inspection of the variation in the individual coupled modal frequencies, we can detect where coupling influences are most dominant. For example, Mode 1 at 28.04 Hz is basically a door panel mode, and Mode 6 at 59.91 Hz is primarily an aft panel mode.

The effect of each of the panel groups on the sound pressure level near MIR (maximum response at nodes 35, 53, or 74) for a constant $F_{z_1} = 44.48$N rms force is shown in Figure 49. The response for all panels active is flagged as CC, where FL, RF, DR, and AS denote, respectively, floor, roof, door, and aft side panels. Upon inspection of this data, it can be seen that in certain frequency regions, several of the panel groups produce higher interior responses acting alone than when all groups act collectively. This is most pronounced for the floor panel and aft side panel responses given in Figures 49a and 49d. From this data we also note that for the given input, the door panels appear to be the least active group, while overall the aft side panels appear to be the most active group in generation of interior noise at MIR. These results are based only on data generated for vertical excitation at the lower engine mount to fuselage attach point.

TABLE 12. PANEL SENSITIVITY STUDY: COUPLED MODES, CABIN-ONLY MODEL

MODE NO.	PANEL GROUPS - FREQUENCY - Hz				
	ALL	FLOOR	ROOF	DOOR	AFT SIDE
1	28.04	26.61	26.61	28.23	26.61
2	39.25	39.26	39.26	39.26	39.25
3	41.94	41.95	41.95	41.95	41.94
4	42.46	42.16	42.16	42.63	42.16
5	56.37	56.28	56.01	56.38	56.06
6	59.91	61.47	61.43	61.51	59.73
7	66.01	67.81	66.86	67.44	67.70
8	68.27	71.50	67.94	71.85	69.46
9	73.44	73.05	75.45	72.84	73.02
10	77.01	75.98	76.24	75.92	76.66
11	80.67	81.37	81.04	80.96	81.37
12	83.84	82.53	82.45	82.48	83.76
13	96.42	95.35	95.40	95.39	96.84
14	100.69	100.46	100.47	100.46	101.71
15	103.41	103.87	103.26	103.67	103.86
16	108.17	107.63	107.21	107.56	107.75
17	112.08	112.35	112.40	112.31	112.36
18	115.44	115.46	115.46	115.47	115.46
19	117.31	119.01	118.78	118.55	118.31
20	121.48	123.10	123.12	123.11	121.41

In Figure 50, the one-third octave noise levels generated by the applied engine forces are given for each of the panel groups. In general, the data shows similar trends as those obtained for the single input force. We see that the cabin resonance in the 63 Hz band for the 1980 rpm (1920 rpm experimental) condition requires collective panel responses to obtain the response generated when all panels are active. On the other hand, the response at the propeller tone in the 80 Hz band for the 2160 rpm condition shows that the floor panels alone far exceed the response produced by all panels acting collectively. Inspection of the coupled mode frequencies given in Table 12, indicates that the propeller tone at 72 Hz for the 2160 rpm condition may easily excite Modes 8 and 9 to varying degrees, depending on the particular panel group in question. Likewise, a slight change in engine rpm would tend to serve the same purpose; that is, force coincidence with a system resonance.

While it appears that for a fixed source, i.e., at a fixed rpm, one panel group may respond more than other panel groups, it must be realized that the aircraft will operate over a rather broad rpm range. In flight, the test aircraft engine rpm can vary from 2100 to 2700 rpm. Thus, overall broad band response must be considered. For example, the propeller tone during flight conditions can vary from 70 to 90 Hz. With a number of system resonances within this range, the individual responses can be controlled by application of damping materials to the appropriate panel groups. However, changes in the structural mass or stiffness properties can remove the occurrence of coupled resonances from the highly excited frequency bands. From the data presented in the previous section, the application of damping treatment appears favorable. No studies to date have been carried out to determine the structural changes necessary to remove system resonances in the critical response bands.

VII. CONCLUSIONS

Cabin noise, fuselage vibration, and engine force and acceleration data were recorded during ground tests of a single engine general aviation aircraft. Analysis of the data taken from various engine-attached/engine-detached, and interior-installed/interior-removed configurations support the following conclusions.

(1) Engine induced structural-borne noise can be a primary interior noise source for single engine aircraft.

(2) All spectra associated with the aircraft are complex periodic consisting of engine 1/2 rpm harmonics.

(3) Cabin noise and fuselage vibration levels are highly influenced by responses at the propeller tone. The A-weighted noise levels are mainly generated by responses in the 800 to 1200 Hz range; however, response at the propeller tone becomes increasingly more important with increasing engine rpm (horsepower).

(4) Cabin acoustic resonances can greatly influence overall noise levels when lying within the frequency range of the propeller tone.

(5) Standard cabin interior trim provides some structural-borne noise control throughout the spectrum; however, it is most effective in the higher frequency range.

Analytical finite element coupled models of the test aircraft structure and acoustic volume were developed for the purpose of determining modeling requirements for the prediction of structural-borne noise in lightweight, single engine aircraft type structures. Comparison of predicted results to laboratory measured aircraft response and to engine running data in the frequency range below 200 Hz support the following conclusions.

(1) Structural-acoustic coupling, i.e., wall flexibility, has a strong influence on fundamental cabin acoustic resonances.

(2) The lightweight fuselage structure has a high modal density which will limit the application of deterministic modeling procedures to the aircraft structure.

(3) Coupled structural-acoustic analysis procedures using finite element models of the fuselage structure and cabin acoustic volume are appropriate for the prediction of structural-borne noise when applying known engine input forces.

(4) The effectiveness of the application of damping materials to the fuselage structure for the reduction of structural-borne noise is mainly limited to resonant response.

REFERENCES

1. Catherines, J. J.; and Mayes, W. H.: Interior Noise Levels of Two Propeller-Driven Light Aircraft. NASA TM X-72716, 1975.

2. Rupf, J. A.: Noise Effects on Passenger Communications in Light Aircraft. Paper No. 770446 presented at SAE Business Aircraft Meeting, Wichita, Kansas, 1977.

3. Broner, N.: The Effects of Low Frequency Noise on People - A Review. Jour. of Sound Vib., Vol. 58, No. 4, 1978.

4. Catherines, J. J.; and Jha, S. K.: Sources and Characteristics of Interior Noise in General Aviation Aircraft. NASA TM X-72839, 1976.

5. Jha, S. K.; and Catherines, J. J.: Interior Noise Studies for General Aviation Types of Aircraft, Part I: Field Studies. Jour. of Sound Vib., Vol. 58, No. 3, 1978.

6. Jha, S. K.; and Catherines, J. J.: Interior Noise Studies for General Aviation Types of Aircraft, Part II: Laboratory Studies. Jour. of Sound Vib., Vol. 58, No. 3, 1978.

7. Mixson, J. S.; Kearney, Barton C. ; and Vaicaitis, R.: Interior Noise Analysis and Control for Light Aircraft. Paper No. 770445 presented at SAE Business Aircraft Meeting, Wichita, Kansas, 1976.

8. Unruh, J. F.; and Scheidt, D. C.: An Investigation of Structural-Borne Noise in General Aviation Aircraft - Data Report. NASA Langley Research Center, Contract No. NAS1-14861, SwRI Project 02-4860, 1978.

9. Craggs, A.; The Transient Response of a Coupled Plate - Acoustic System Using Plate and Acoustic Finite Elements, Jour. Sound Vib., 15 (4), 1971, pp 509-528.

10. Craggs, A.: The Use of Simple Three-Dimensional Acoustic Finite Elements for Determinining the Natural Modes and Frequencies of Complex Shaped Enclosures, Jour. Sound Vib., 23 (3), 1972, pp 331-339.

11. Shuka, T.; and Ishihara, K.: The Analysis of the Acoustic Field in Irregularly Shaped Rooms by the Finite Element Method, Jour. Sound Vib. 29, (1), 1973, pp 67-76.

12. Petyt, M.; Lea, J.; and Koopmann, G. H.: A Finite Element Method for Determining the Acoustic Modes of Irregular Shaped Cavities, Jour. Sound Vib., 45 (4), 1976, pp 497-502.

13. Craggs, A.: An Acoustic Finite Element Approach for Studying Boundary Flexibility and Sound Transmission Between Irregular Enclosures, Jour. Sound Vib., 30 (3), pp 343-357.

14. Nefske, D.J.; and Howell, L.J.: Automobile Interior Noise Reduction Using Finite Element Methods, Paper No. 780365, presented at SAE Congress and Exposition, Detroit, Mich., Feb. 1978.

15. Unruh, J. F.: A Finite Element Subvolume Technique for Structural-Borne Interior Noise Prediction. Paper No. 79-0585 presented at AIAA 5th Aeroacoustics Conference, Seattle, Washington, 1979.

16. Zienkiewicz, O. C.: The Finite Element Method in Engineering Science, McGraw Hill, 1971.

17. Morse, P. M.; and Ingard, K. U.: Theoretical Acoustics, New York: McGraw Hill, 1968.

18. Finlayson, B. A.: The Method of Weighted Residuals and Variational Principles, Academic Press, New York, 1972.

19. Karamcheti, K.: Principles of Ideal-Fluid Aerodynamics, John Wiley and Sons, 1966.

20. Hurty, W. C.; and Rubinstein, M. F.: Dynamics of Structures, Prentice Hall, 1964.

21. Wittlin, G.; Gamon, M. A.; and LaBarge, W. L.: Full Scale Crash Test Experimental Verification of a Method of Analysis for General Aviation Airplane Structural Crashworthiness. Lockheed- California Company, FAA-RD-77-188, U. S. Dept. of Transportation, Federal Aviation Administration, Washington, D.C., 1976.

22. Cessna Aircraft: Detailed Fuselage Section Properties Developed Under Subcontract to Lockheed- California Company for Structural Model Used in Reference 21.

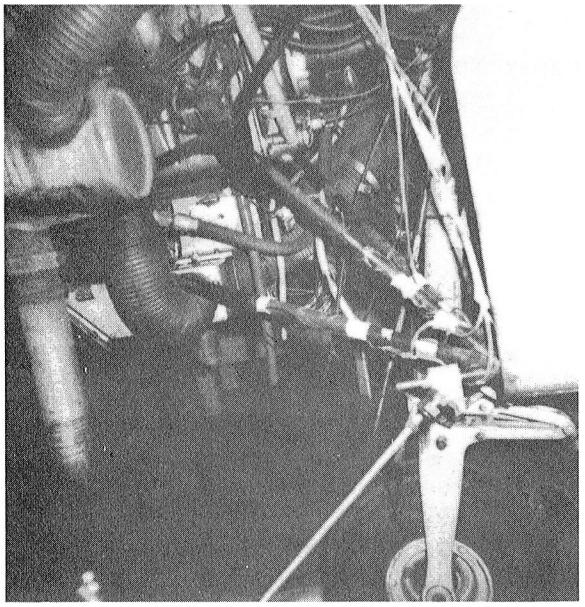

SHAKER ATTACHED TO ENGINE MOUNT - POSITION #2

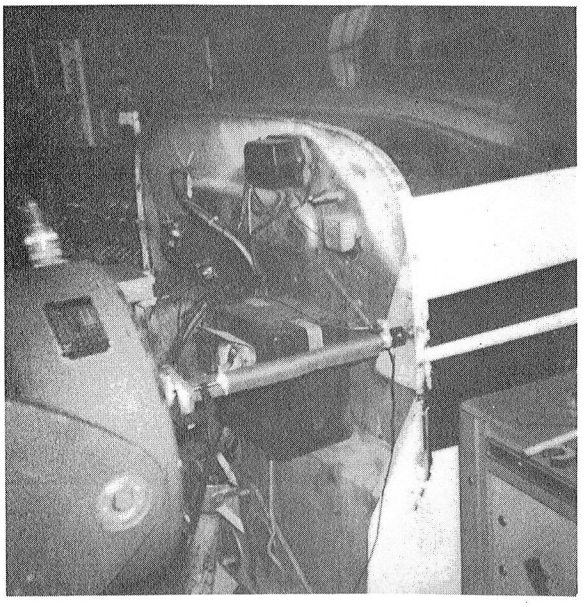

SHAKER ATTACHED TO FUSELAGE - POSITION #1

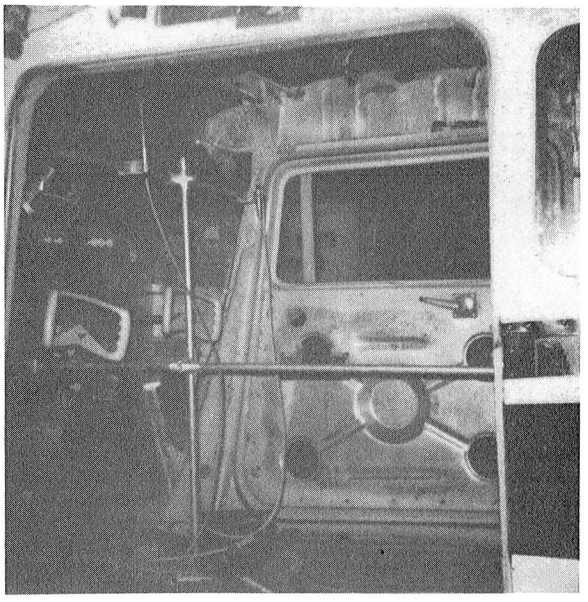

MICROPHONE SUPPORT

FIGURE 1. ELECTRODYNAMIC SHAKER AND FIXED MICROPHONE SUPPORT

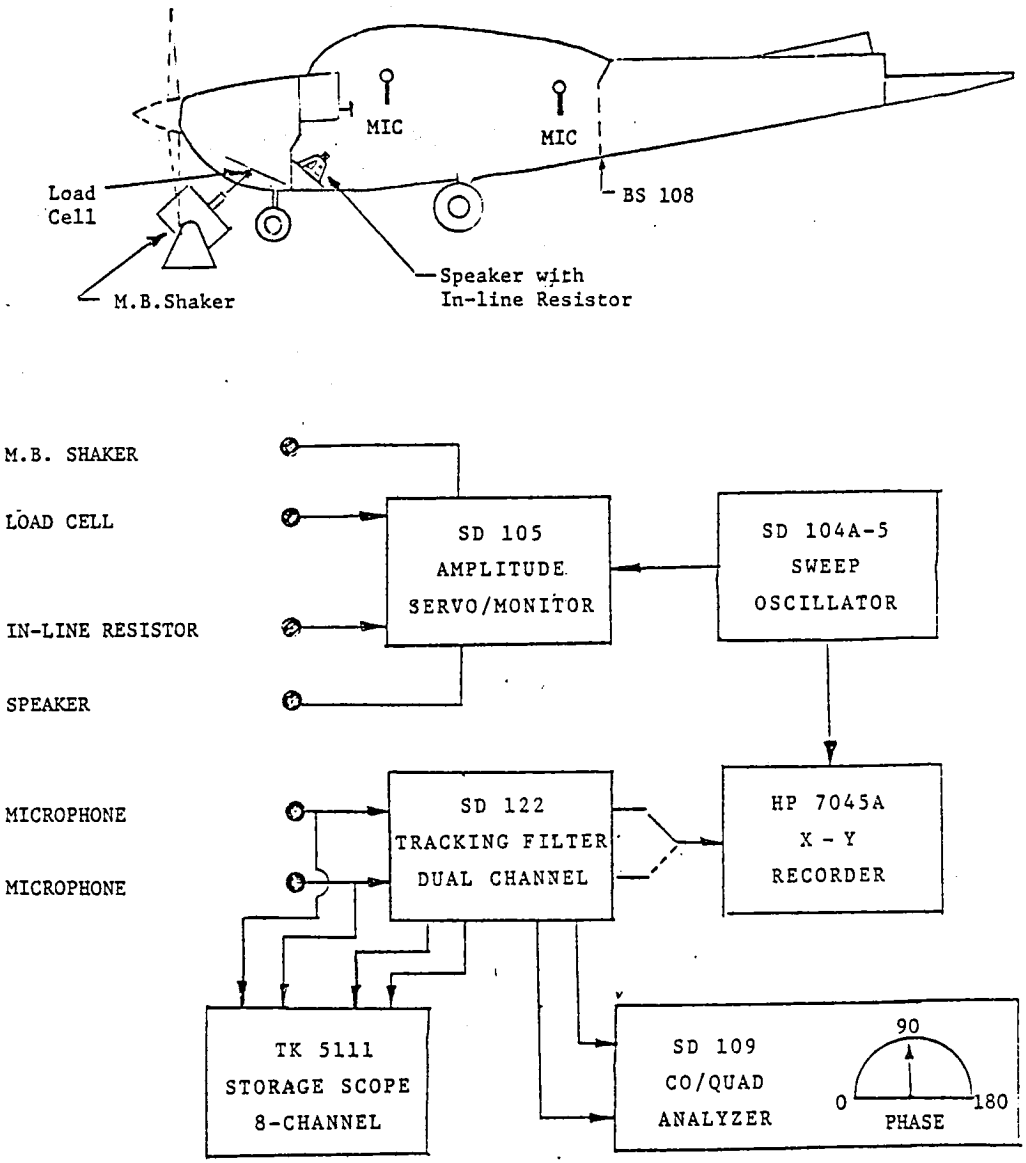

SD - Spectral Dynamics, TK - Tektronix, HP - Hewlett-Packard

FIGURE 2. INSTRUMENTATION AND DATA ACQUISITION SYSTEM FOR INTERIOR ACOUSTIC MODAL SURVEYS.

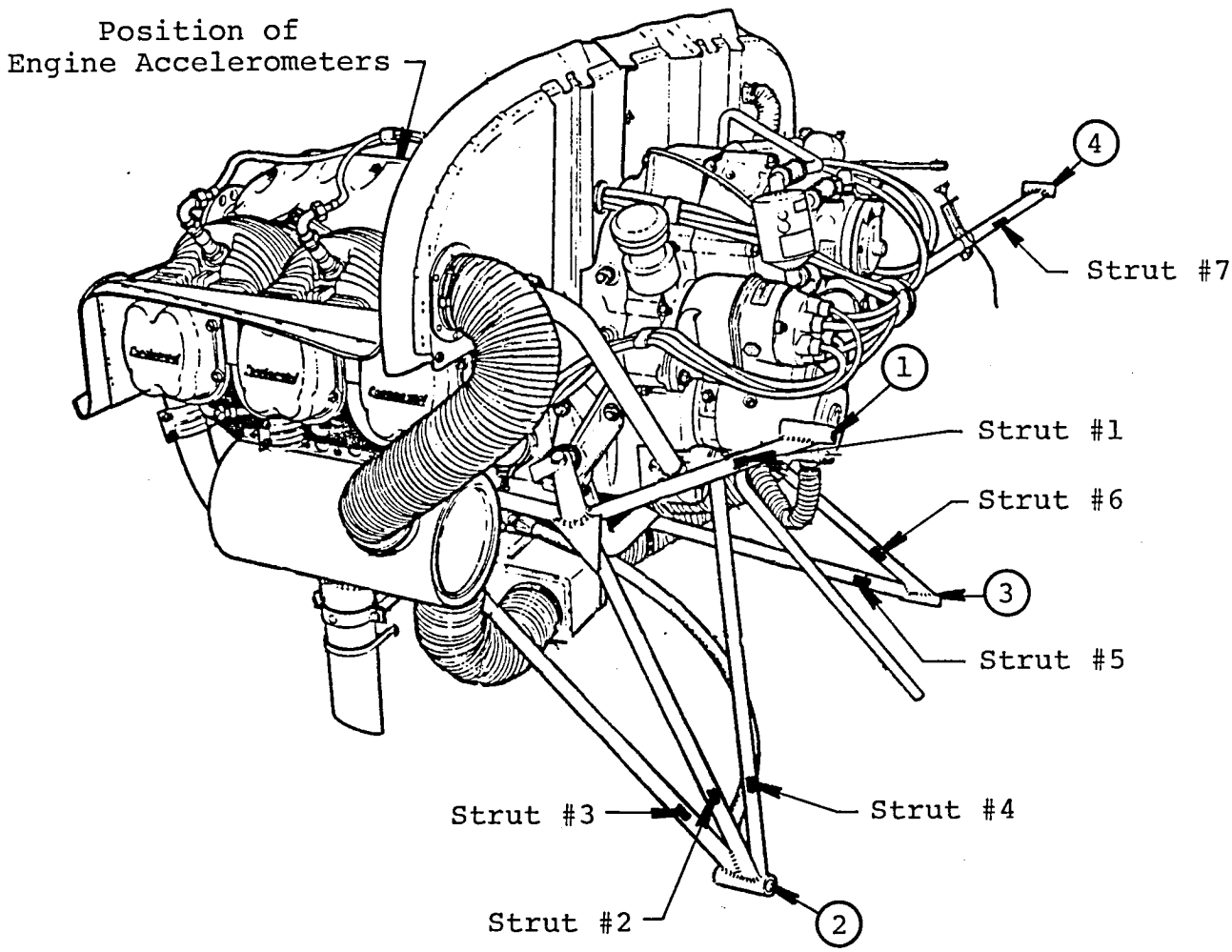

(X) Engine to Fuselage Attach Point

FIGURE 3. ENGINE MOUNT AND STRUT NUMBERING SEQUENCE.

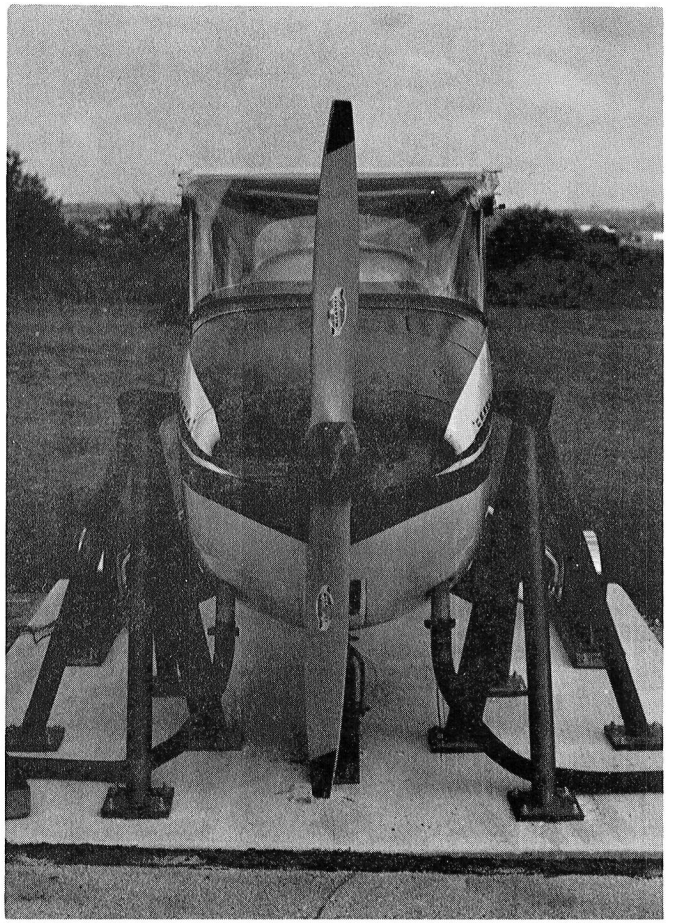

(a)

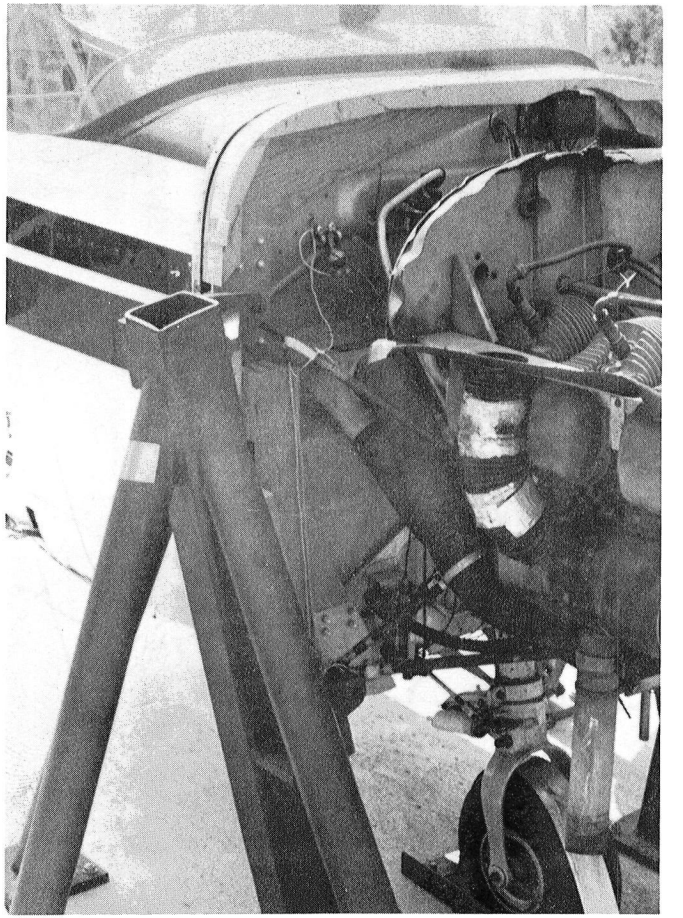

(b)

FIGURE 4. ENGINE SUPPORT SYSTEM AND FALSE FIREWALL FOR COWL SUPPORT.

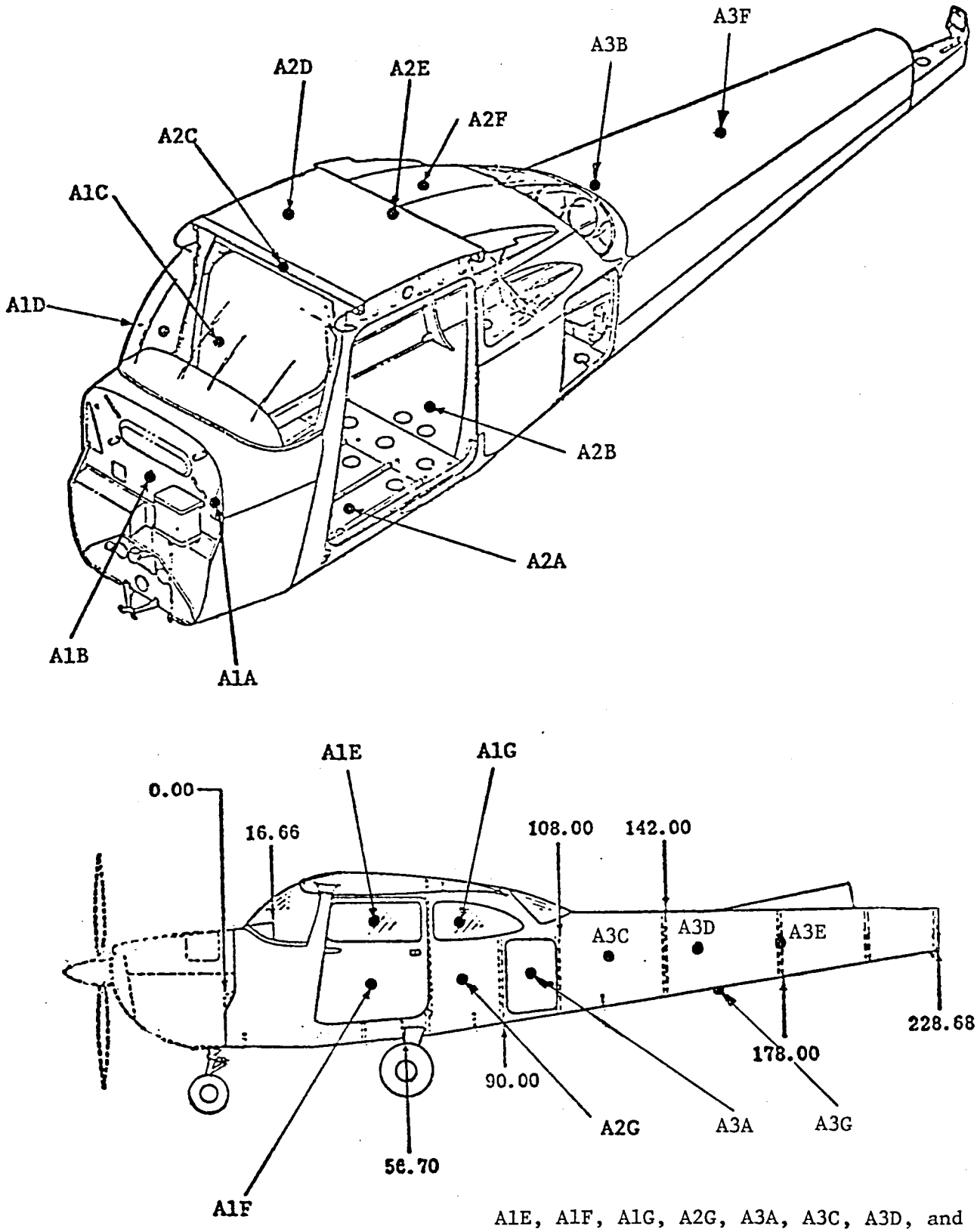

A1E, A1F, A1G, A2G, A3A, A3C, A3D, and A3E on opposite side of aircraft.

FIGURE 5. MODEL 172 ACCELEROMETER LOCATIONS

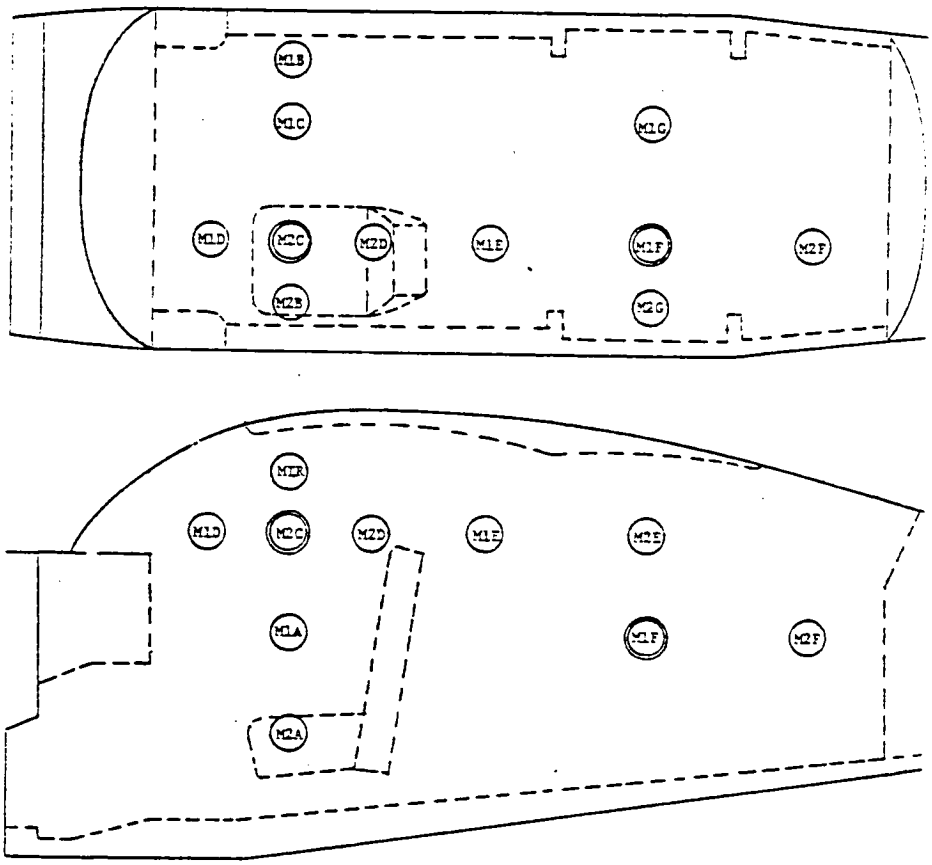

FIGURE 6. MICROPHONE LOCATIONS

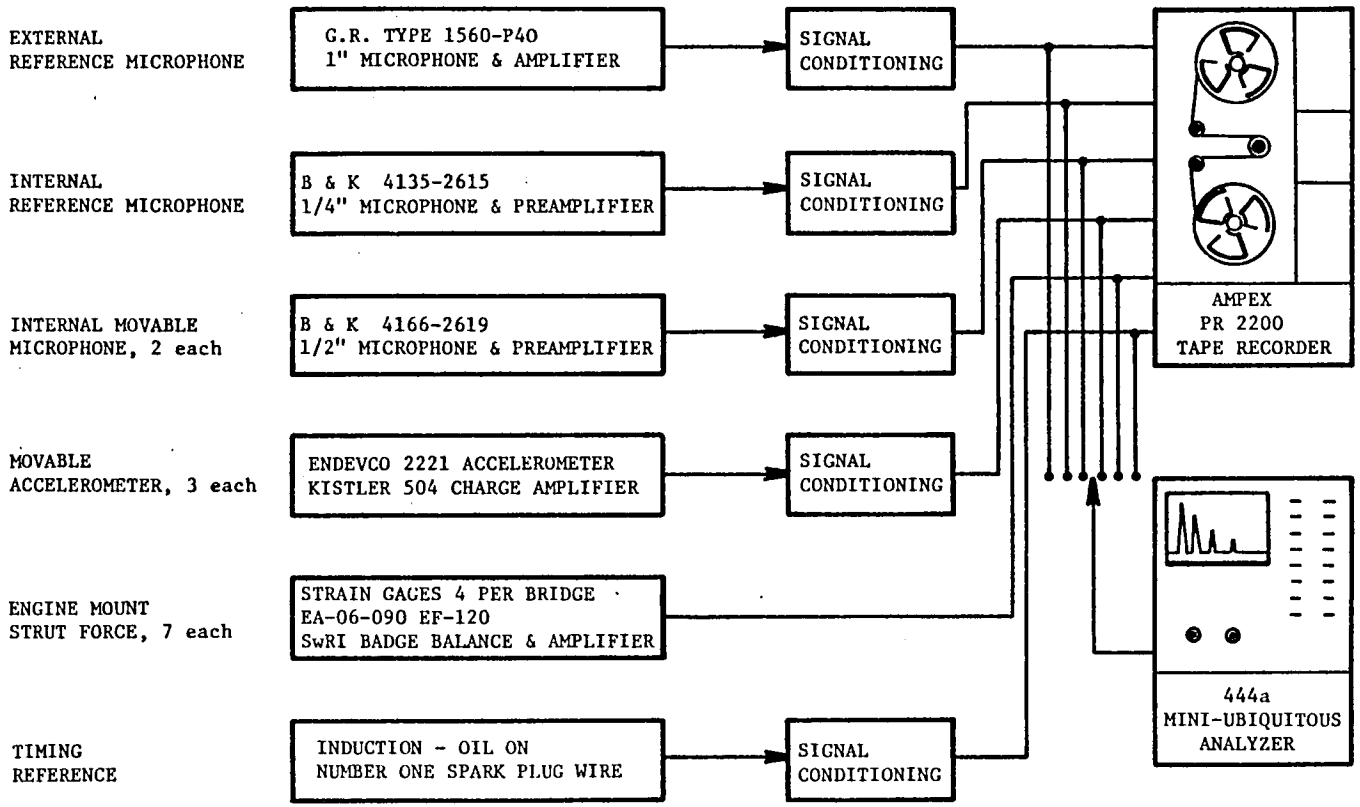

FIGURE 7. INSTRUMENTATION USED DURING ENGINE RUNNING TESTS.

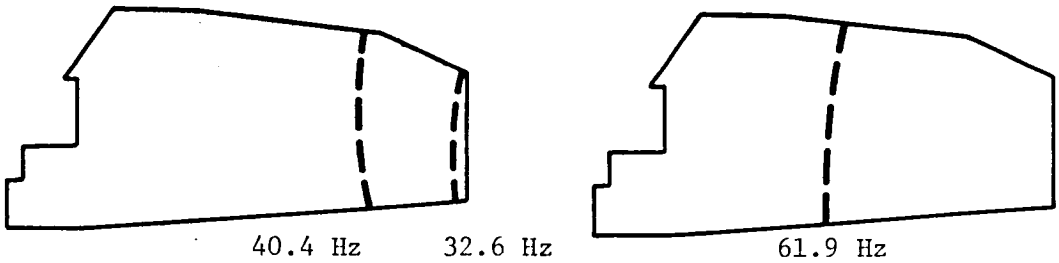

(a) Interior Installed - Bulkhead at B.S. 108 Flexible

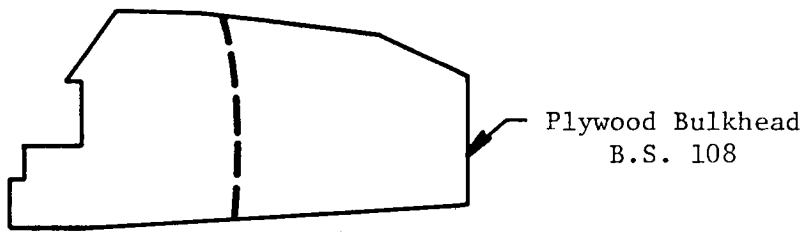

(b) Interior Installed - Bulkhead at B.S. 108 Rigid

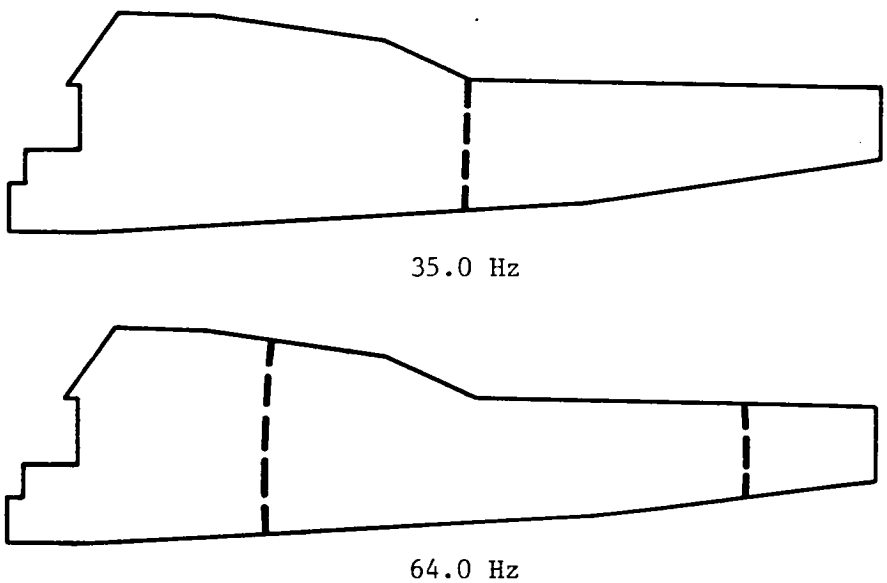

(c) Interior Removed

FIGURE 8. MEASURED ACOUSTIC RESONANCES AND NODE LINES.

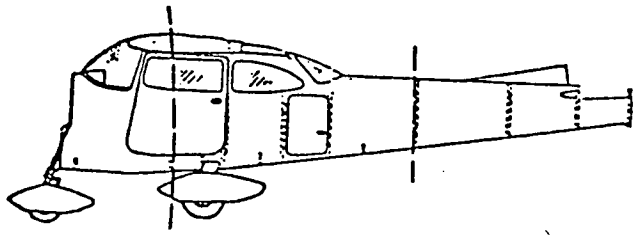

(a) FUSELAGE VERTICAL BENDING, ENGINE DETACHED, 56.4 Hz

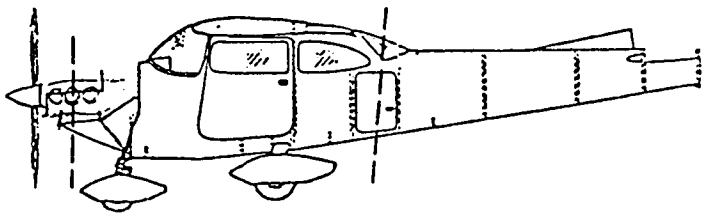

(b) FUSELAGE VERTICAL BENDING, ENGINE ATTACHED, 14.4 Hz

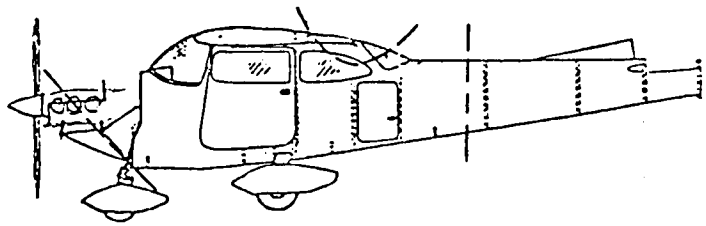

(c) FUSELAGE VERTICAL BENDING, ENGINE ATTACHED, 47.0 Hz

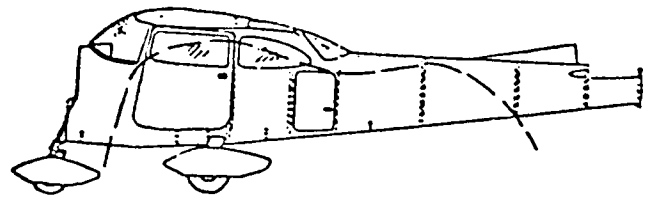

(a) FUSELAGE SIDE BENDING, ENGINE DETACHED, 53.0 Hz

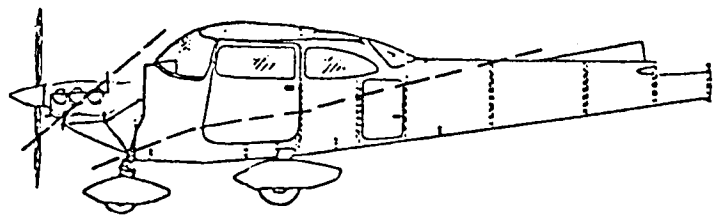

(b) FUSELAGE SIDE BENDING, ENGINE ATTACHED, 16.0 Hz

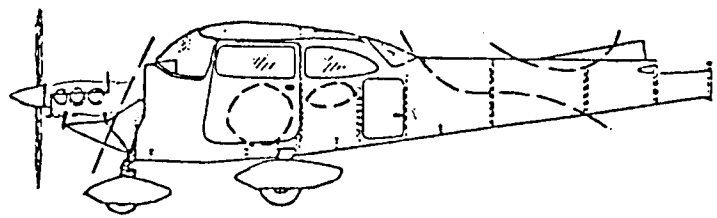

(c) FUSELAGE SIDE BENDING, ENGINE ATTACHED, 43.0 Hz

FIGURE 9. FUSELAGE PRIMARY BENDING MODES.

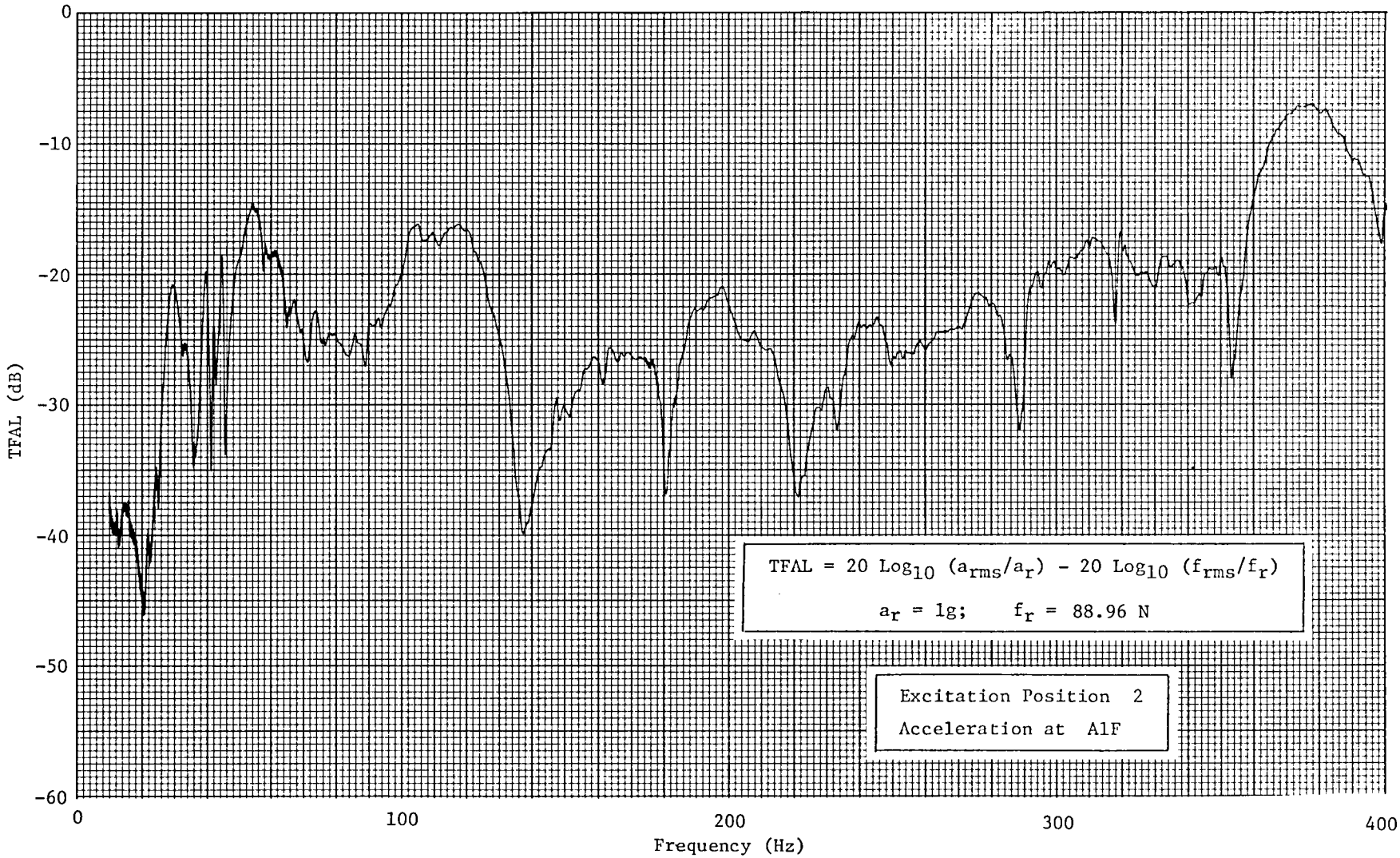

FIGURE 10. TRANSFER FUNCTION FOR FIREWALL EXCITATION TO FUSELAGE VIBRATION RESPONSE

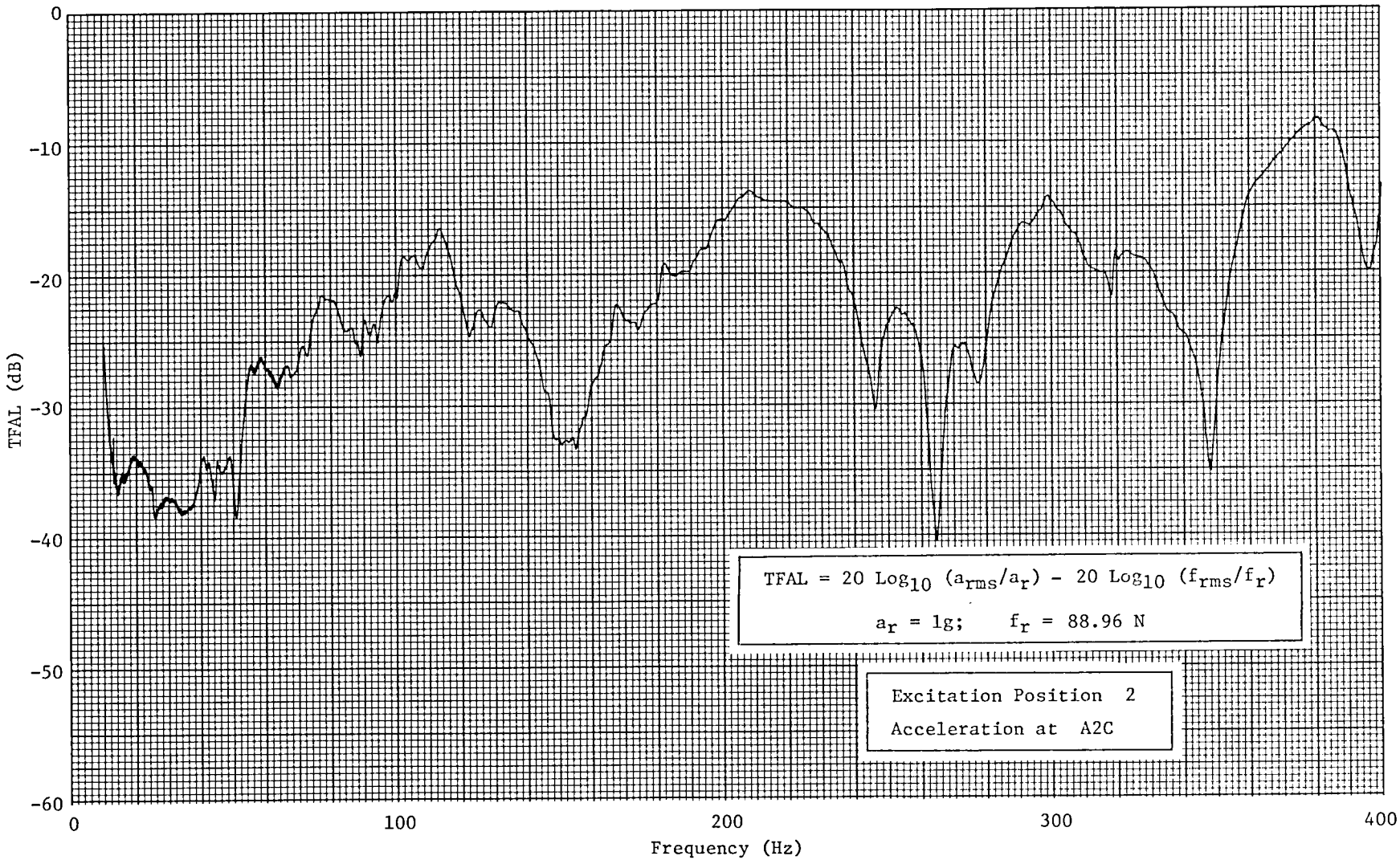

FIGURE 11. TRANSFER FUNCTION FOR FIREWALL EXCITATION TO FUSELAGE VIBRATION RESPONSE

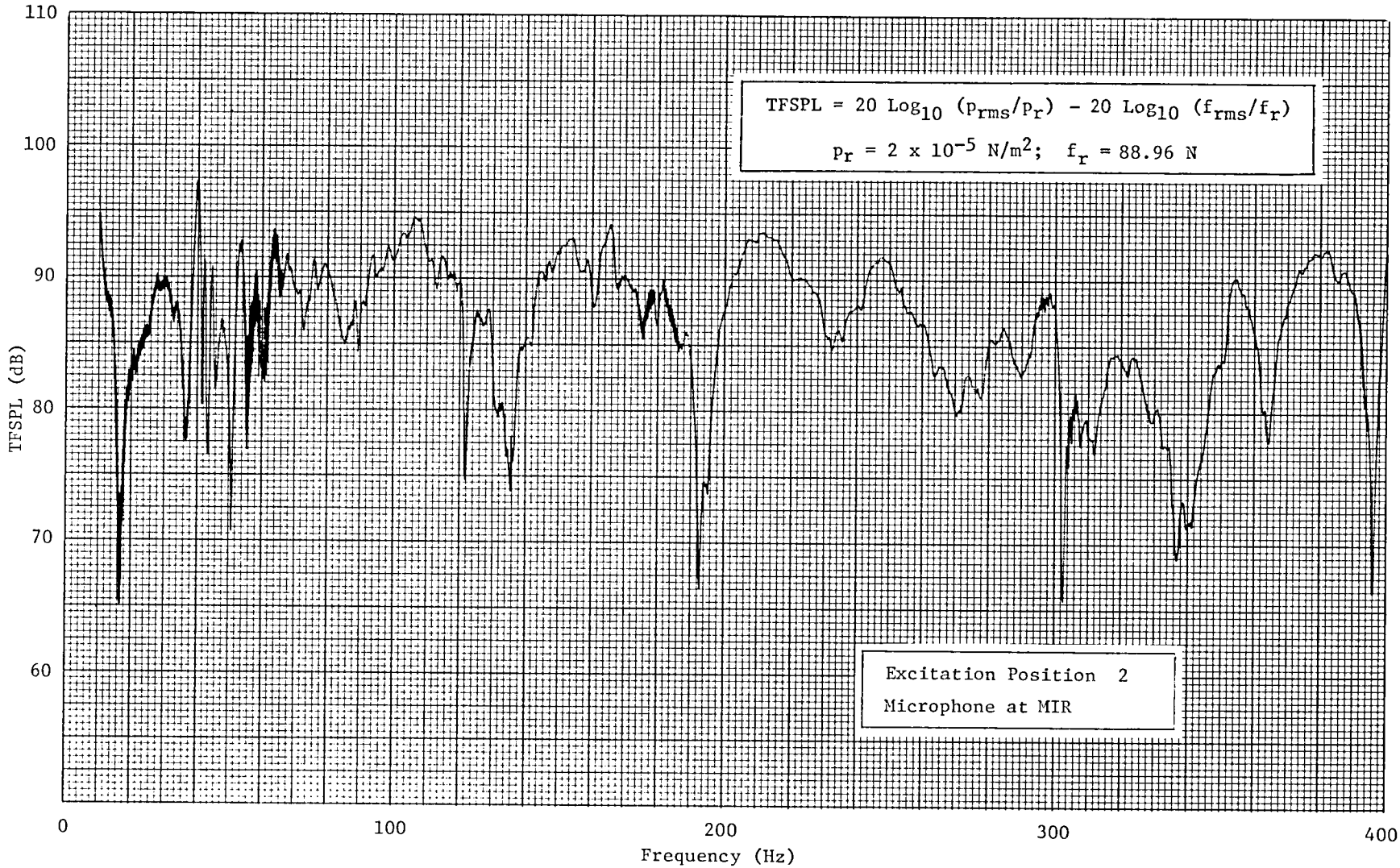

FIGURE 12. TRANSFER FUNCTION FOR FIREWALL EXCITATION TO INTERIOR NOISE RESPONSE

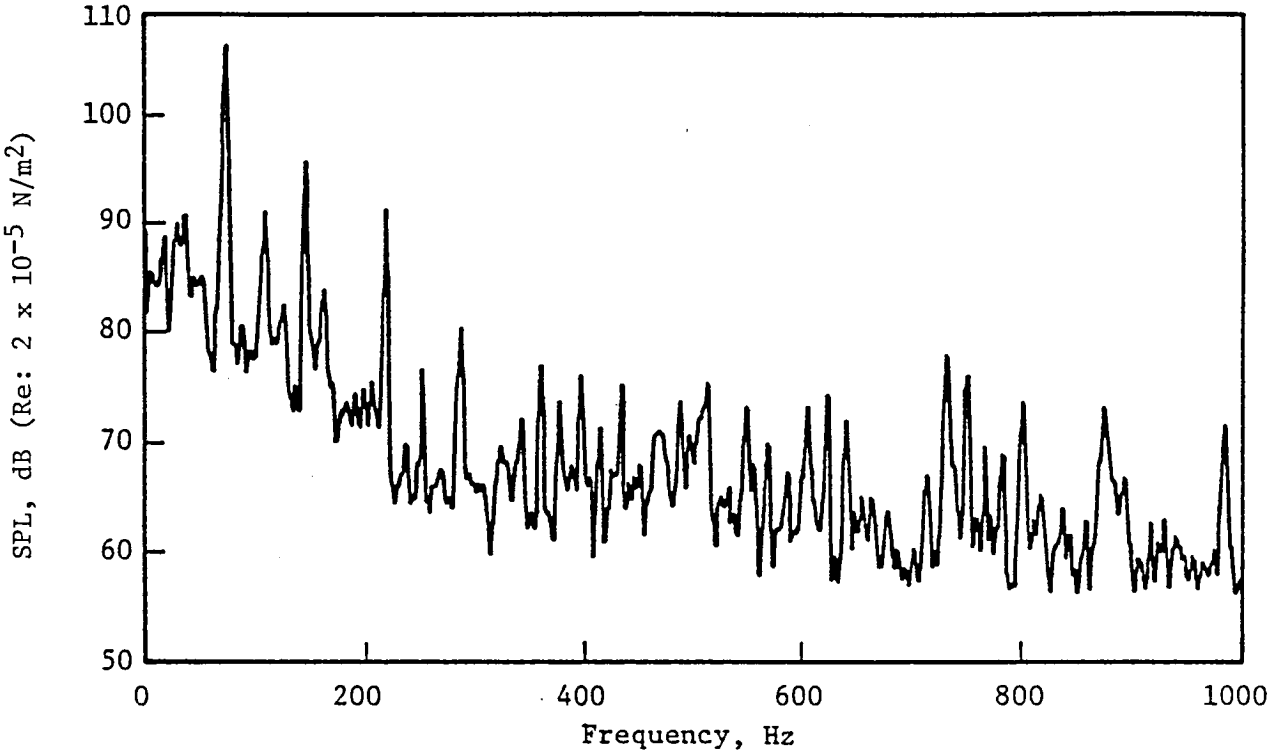

(1) Engine Attached

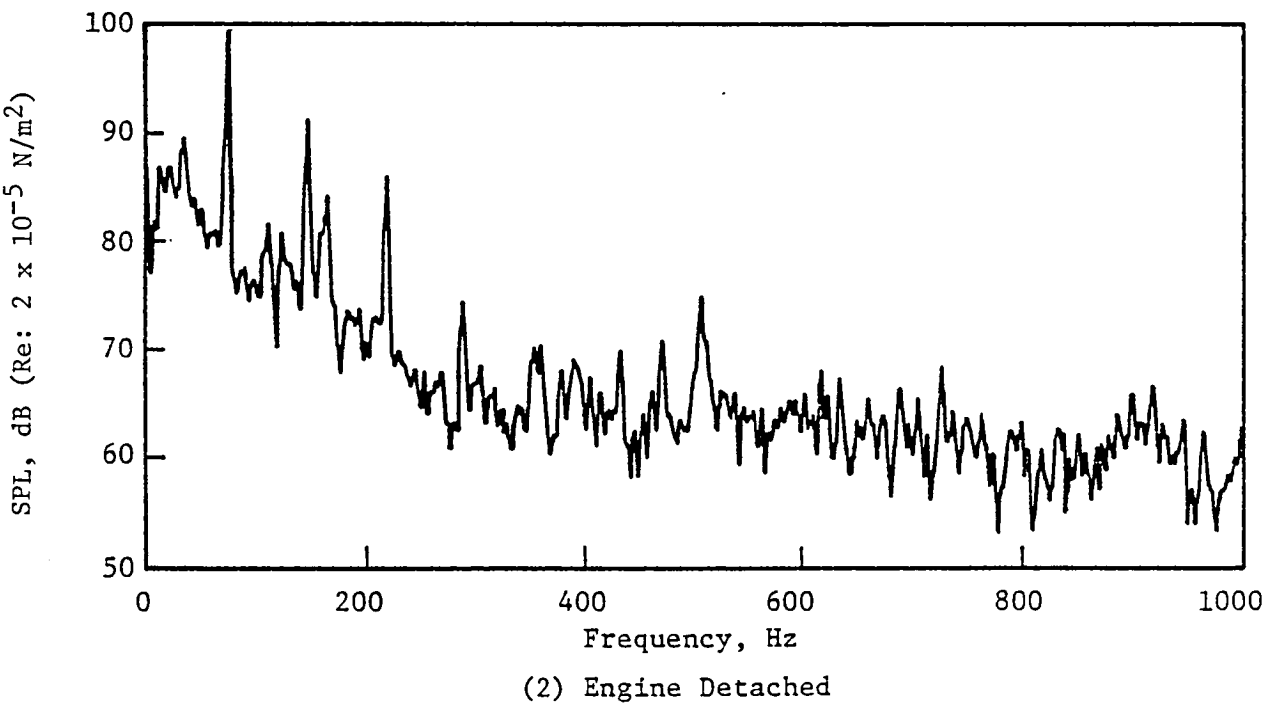

(2) Engine Detached

(a) Spectra of Interior Noise at MIR; Interior Installed

FIGURE 13. TYPICAL NARROW BAND SPECTRA, 2160 RPM, BANDWIDTH 3.0 Hz,

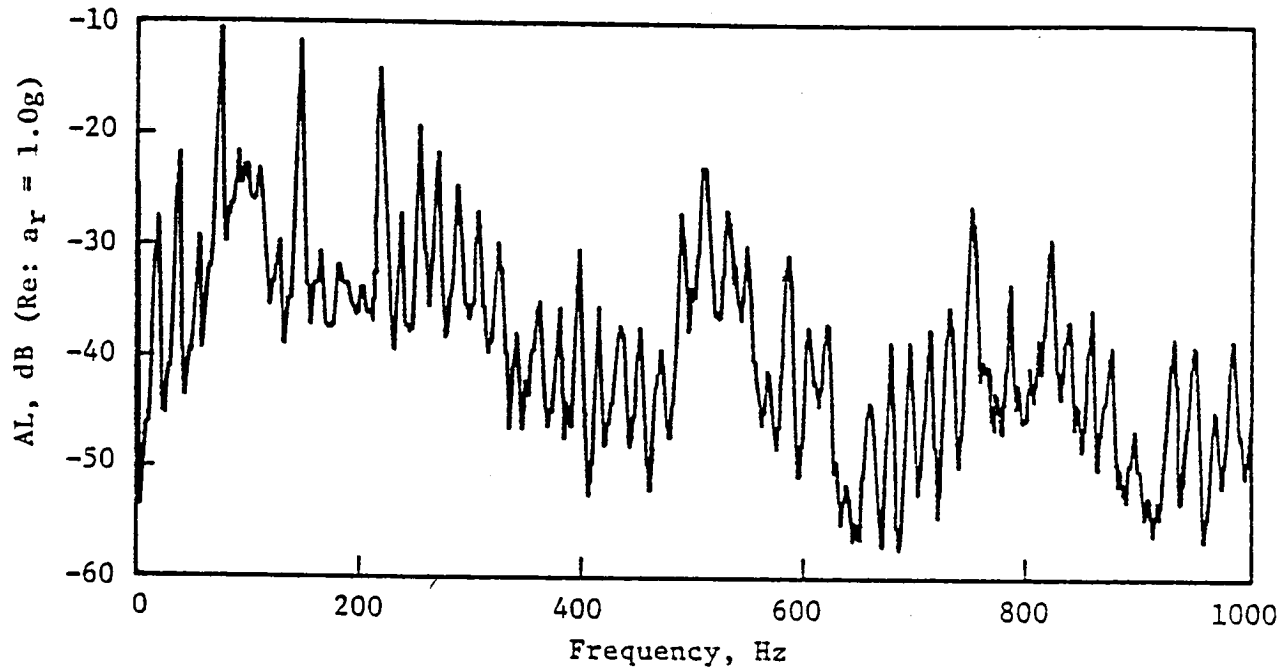

(1) Engine Attached

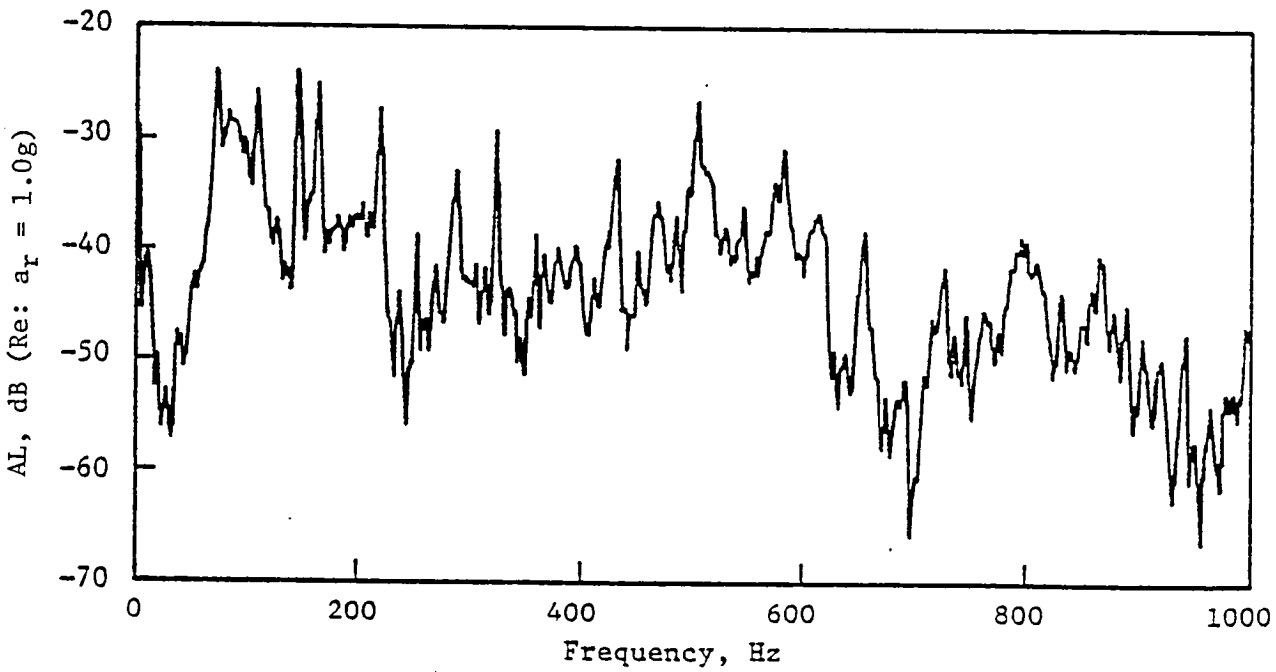

(2) Engine Detached

(b) Spectra of Fuselage Acceleration Levels at A2A; Interior Installed

FIGURE 13 CONT. TYPICAL NARROW BAND SPECTRA, 2160 RPM, BANDWIDTH 3.0 Hz.

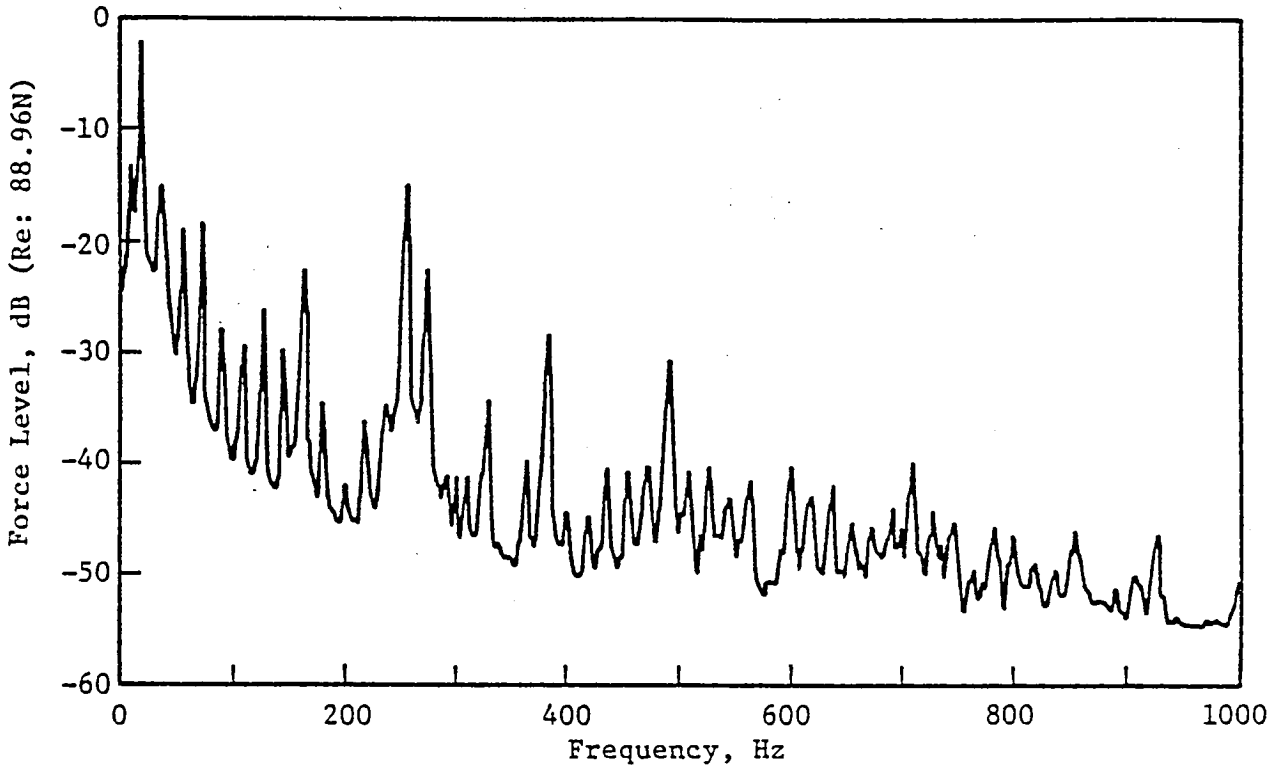

(c) Spectrum of Force Levels in Strut #1

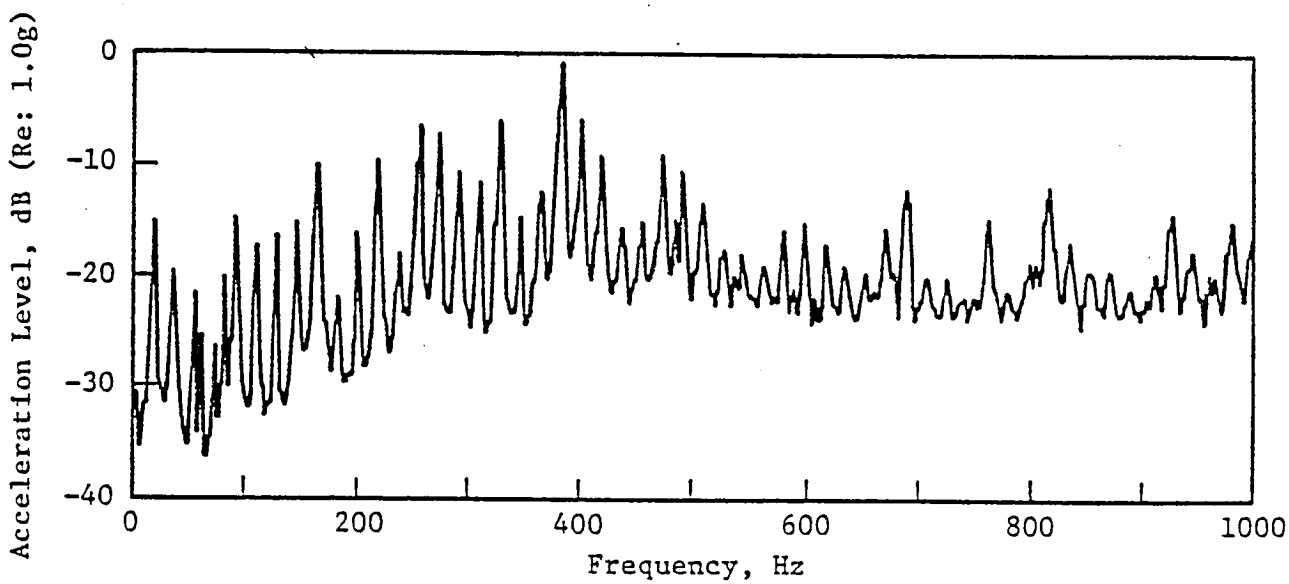

(d) Spectra of Engine Lateral Acceleration

FIGURE 13 CONT. TYPICAL NARROW BAND SPECTRA, 2160 RPM, BANDWIDTH 3.0 Hz.

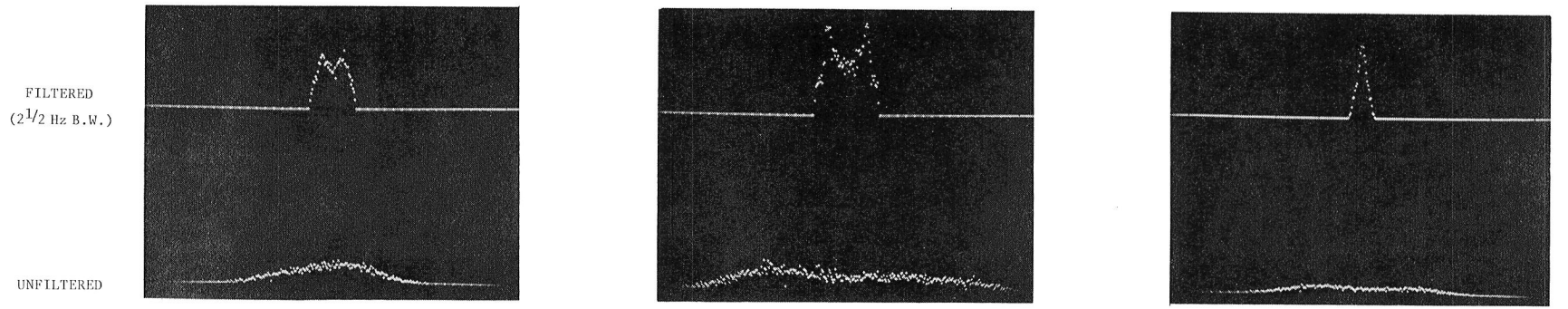

1680 RPM - 56 Hz

1920 RPM 64 Hz

2160 RPM - 72 Hz

(a) FIRST PROPELLER

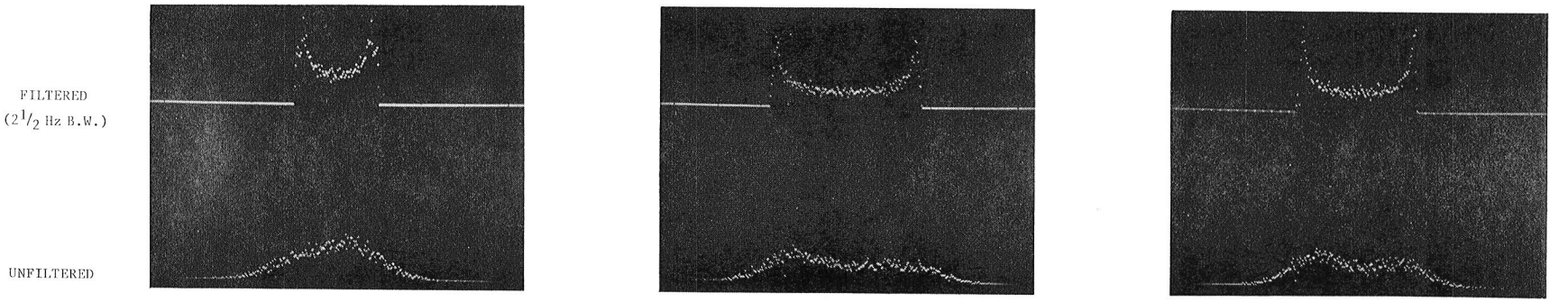

1680 RPM - 102 Hz

1920 RPM - 128 Hz

2160 RPM - 144 Hz

(b) SECOND PROPELLER

FIGURE 14. PROBABILITY DENSITY FUNCTIONS AT INTERNAL MICROPHONE MIR

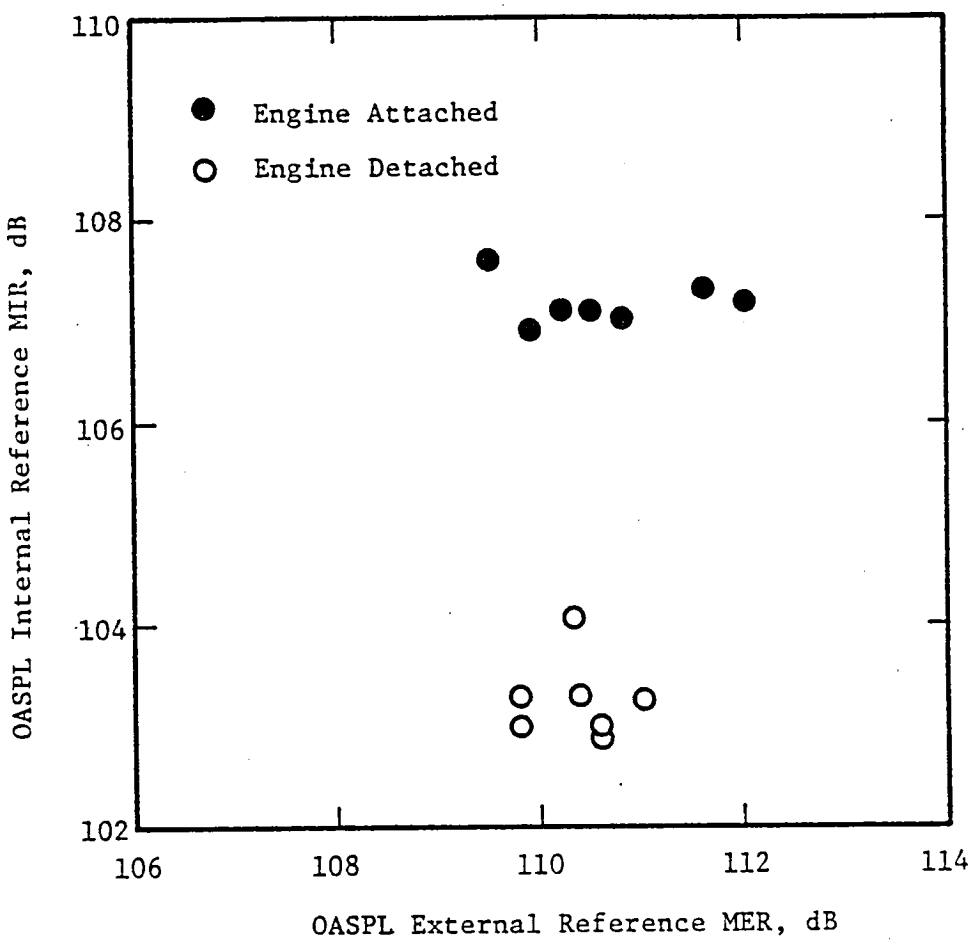

FIGURE 15. CORRELATION OF SPL AT MIR AND MER, INTERIOR INSTALLED, 2160 RPM.

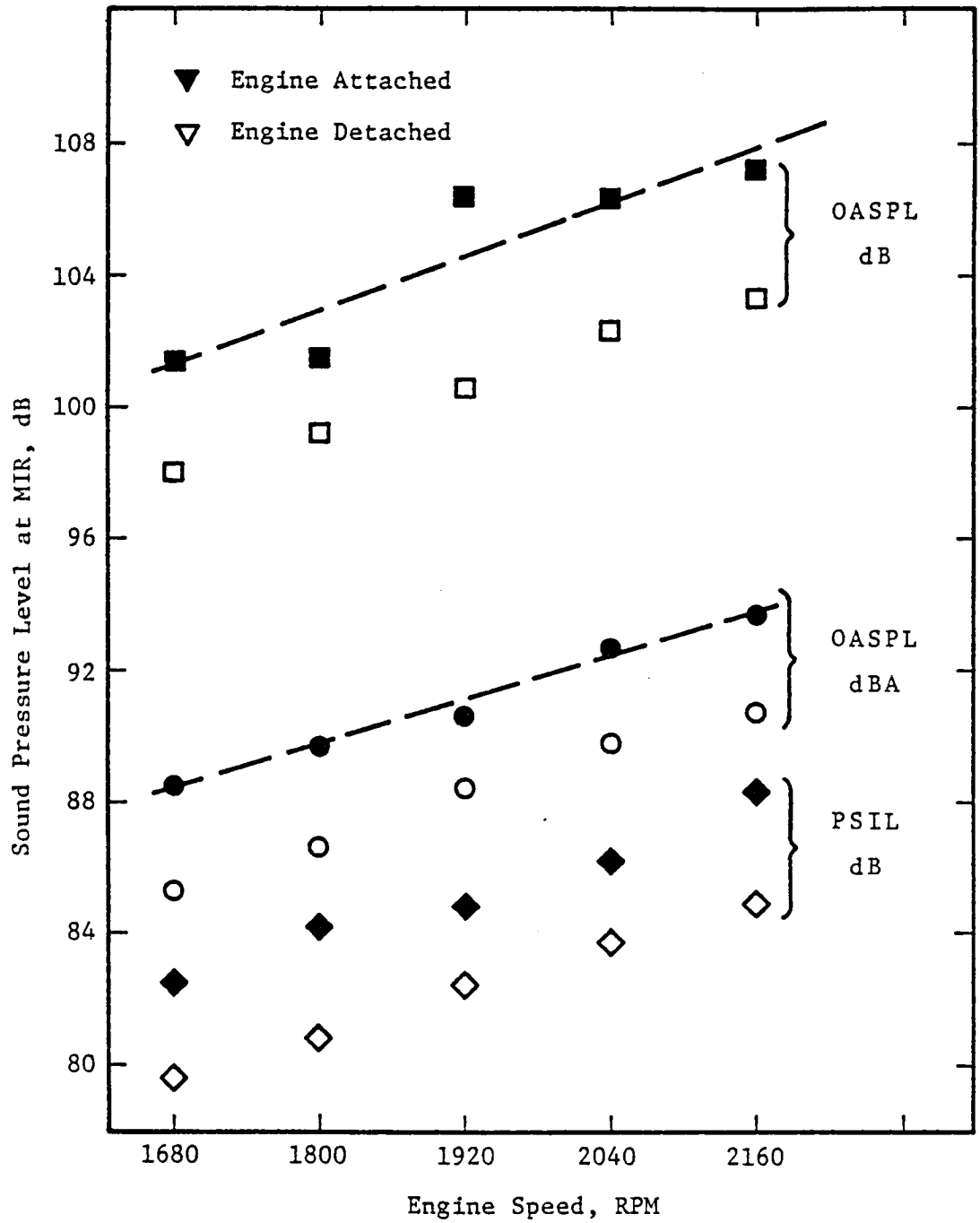

FIGURE 16. VARIATION OF SOUND PRESSURE LEVEL AT MIR WITH ENGINE SPEED, INTERIOR INSTALLED.

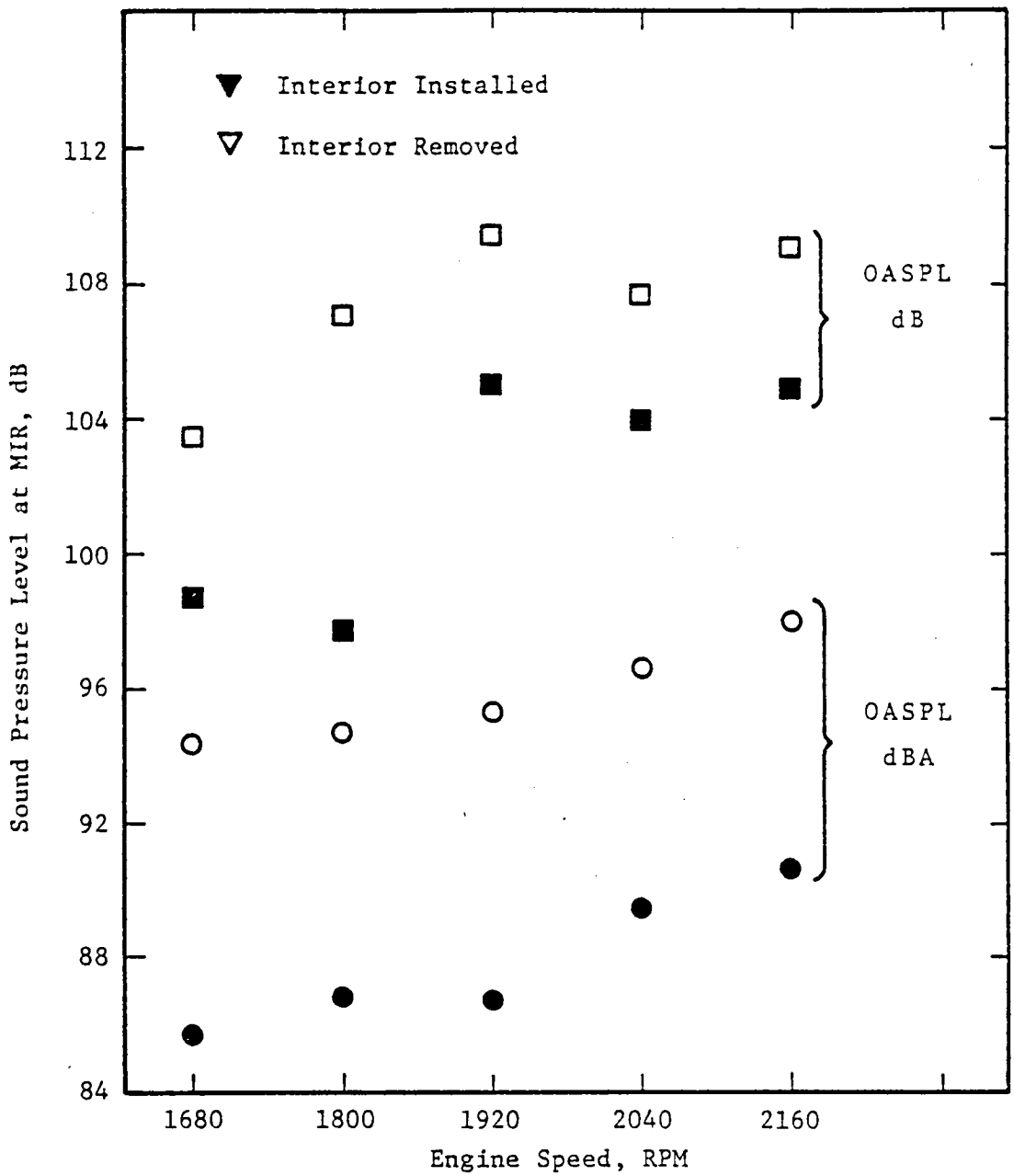

FIGURE 17. VARIATION OF THE ENGINE ALONE CONTRIBUTION TO THE SOUND PRESSURE LEVEL AT MIR WITH ENGINE SPEED.

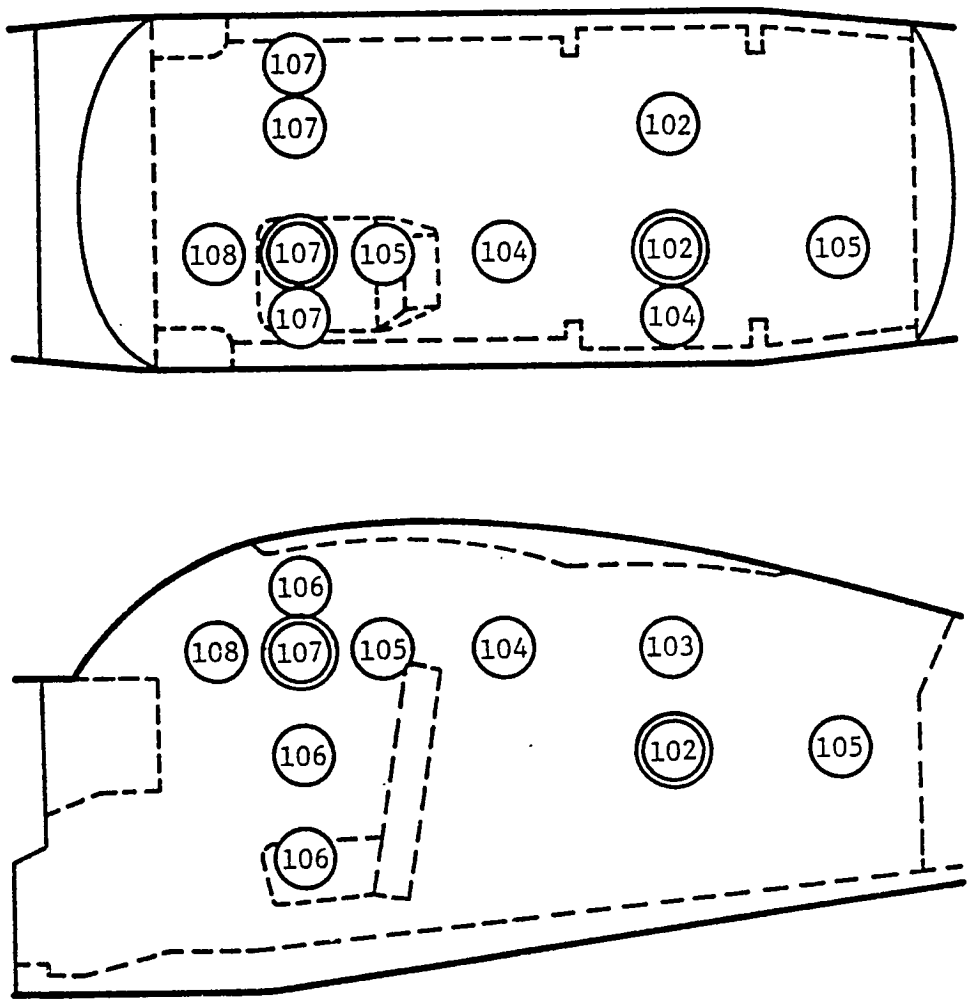

FIGURE 18. DISTRIBUTION OF OASPL, dB, AT CABIN RESONANCE, INTERIOR INSTALLED, ENGINE ATTACHED, 1920 RPM.

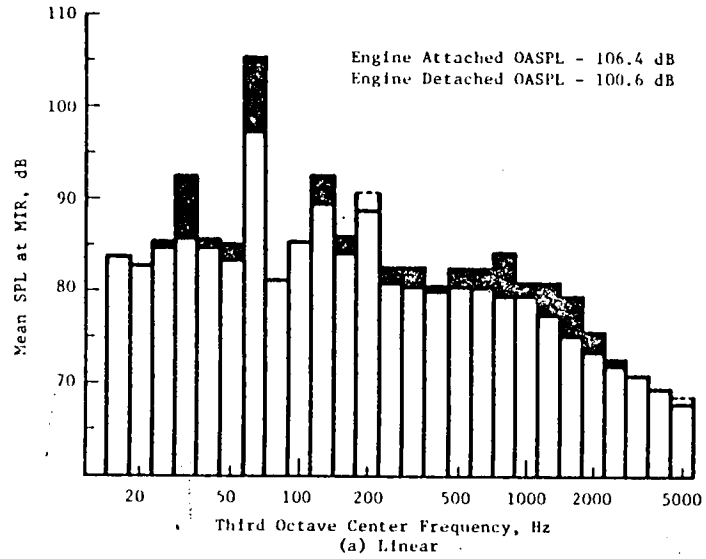

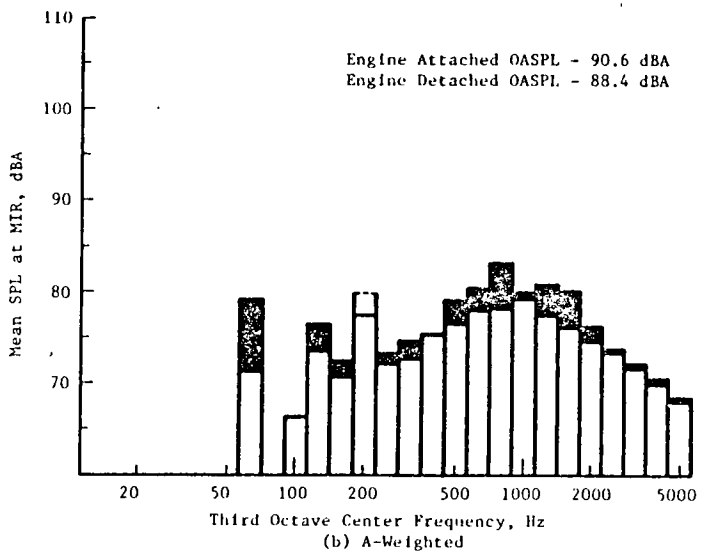

FIGURE 19. ONE-THIRD OCTAVE SPECTRA OF NOISE LEVELS AT MIR: INTERIOR INSTALLED; 1920 RPM.

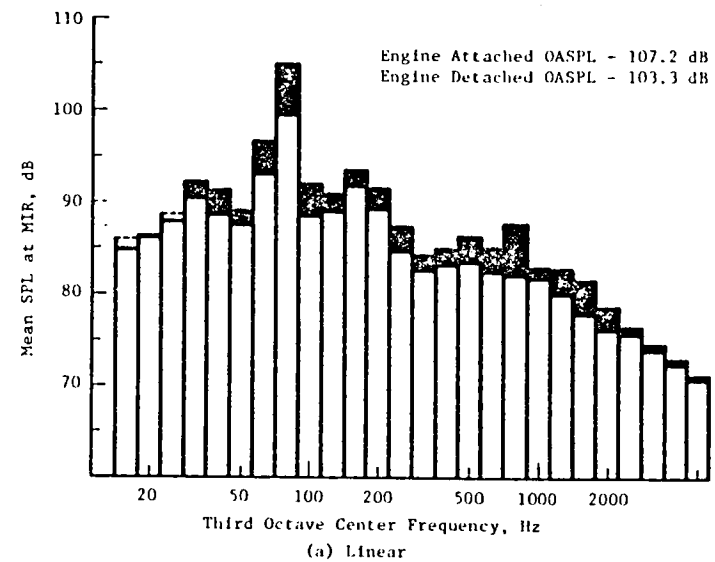

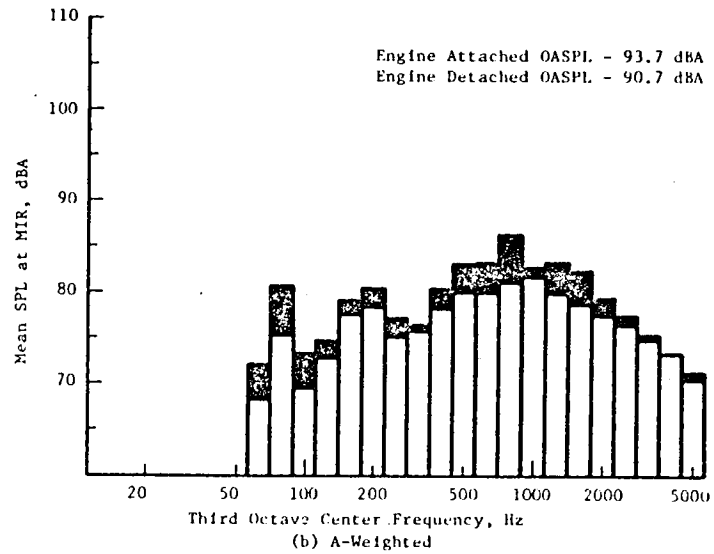

FIGURE 20. ONE-THIRD OCTAVE SPECTRA OF NOISE LEVELS AT MIR; INTERIOR INSTALLED; 2160 RPM.

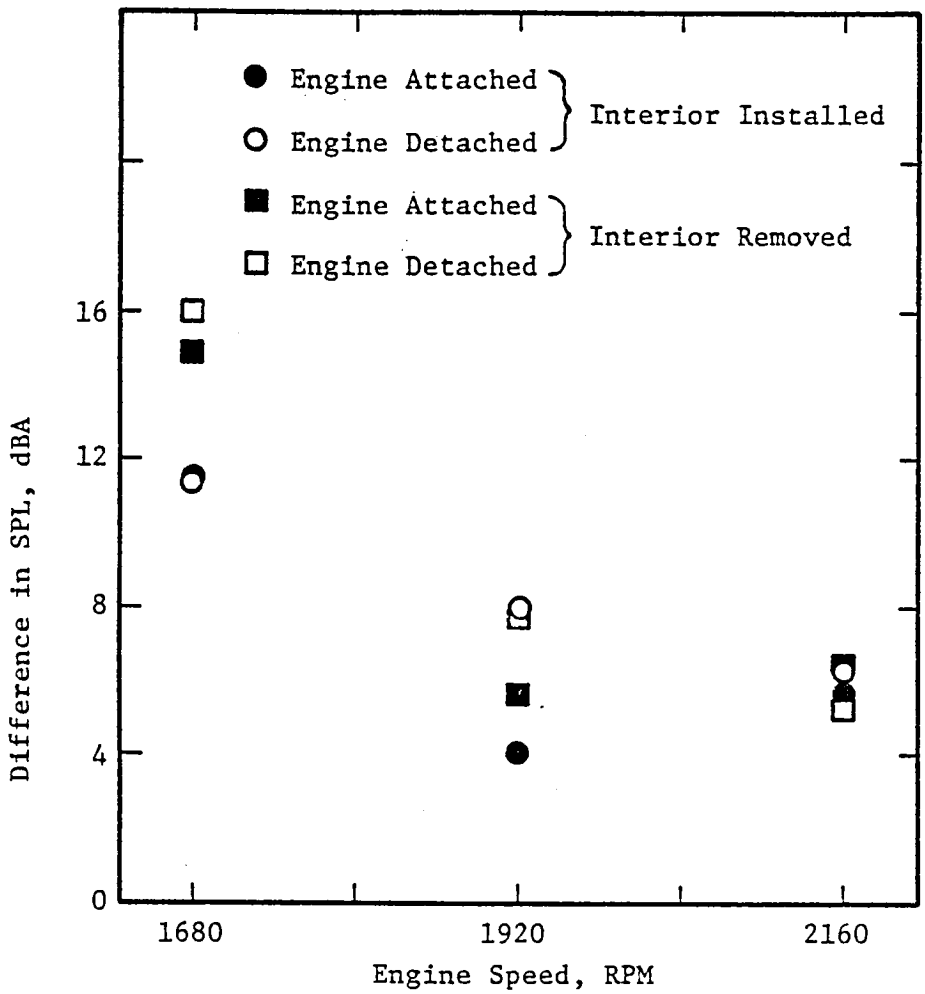

FIGURE 21. DIFFERENCE IN A-WEIGHTED ONE-THIRD OCTAVE PEAK LEVEL AND ONE-THIRD OCTAVE LEVEL CONTAINING THE PROPELLER TONE VERSUS ENGINE SPEED.

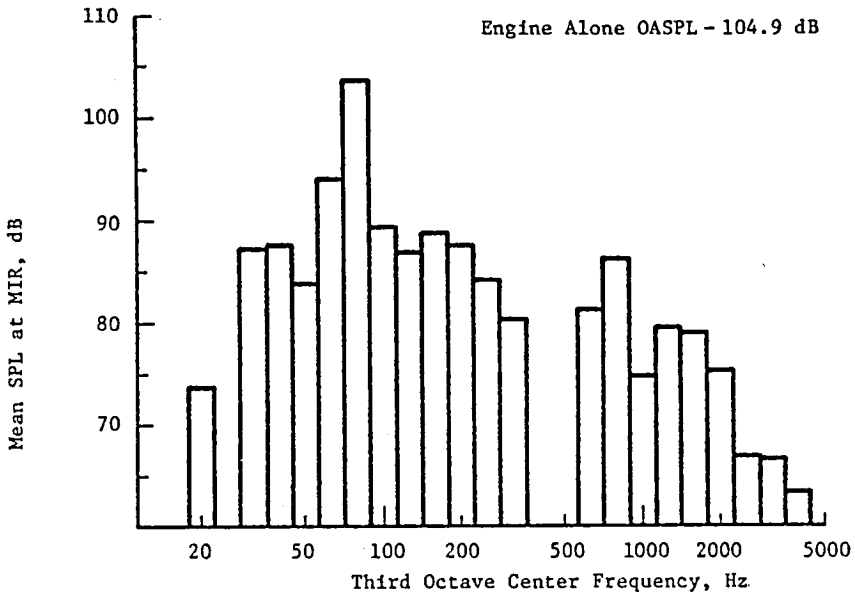

a) Interior Installed

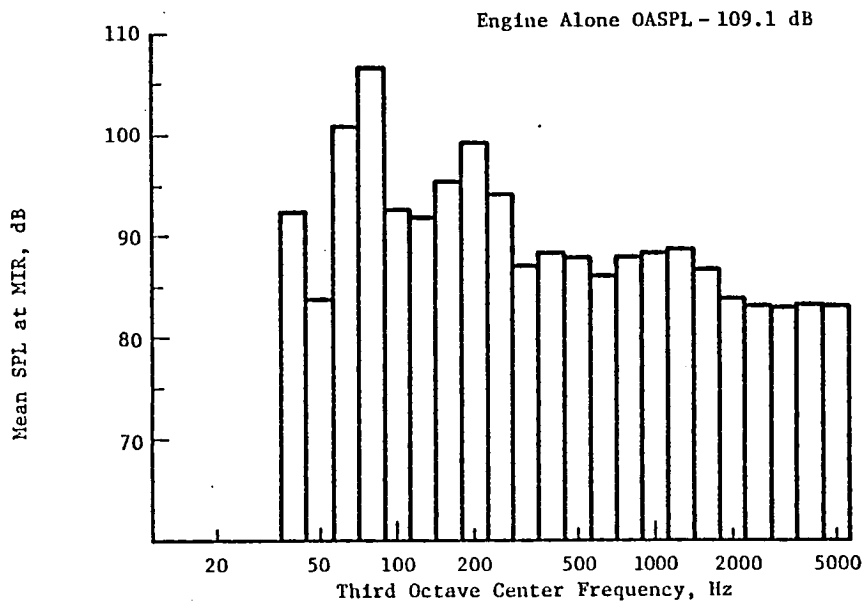

b) Interior Removed

FIGURE 22. ENGINE ALONE ONE-THIRD OCTAVE SPECTRA AT MIR, 2160 RPM.

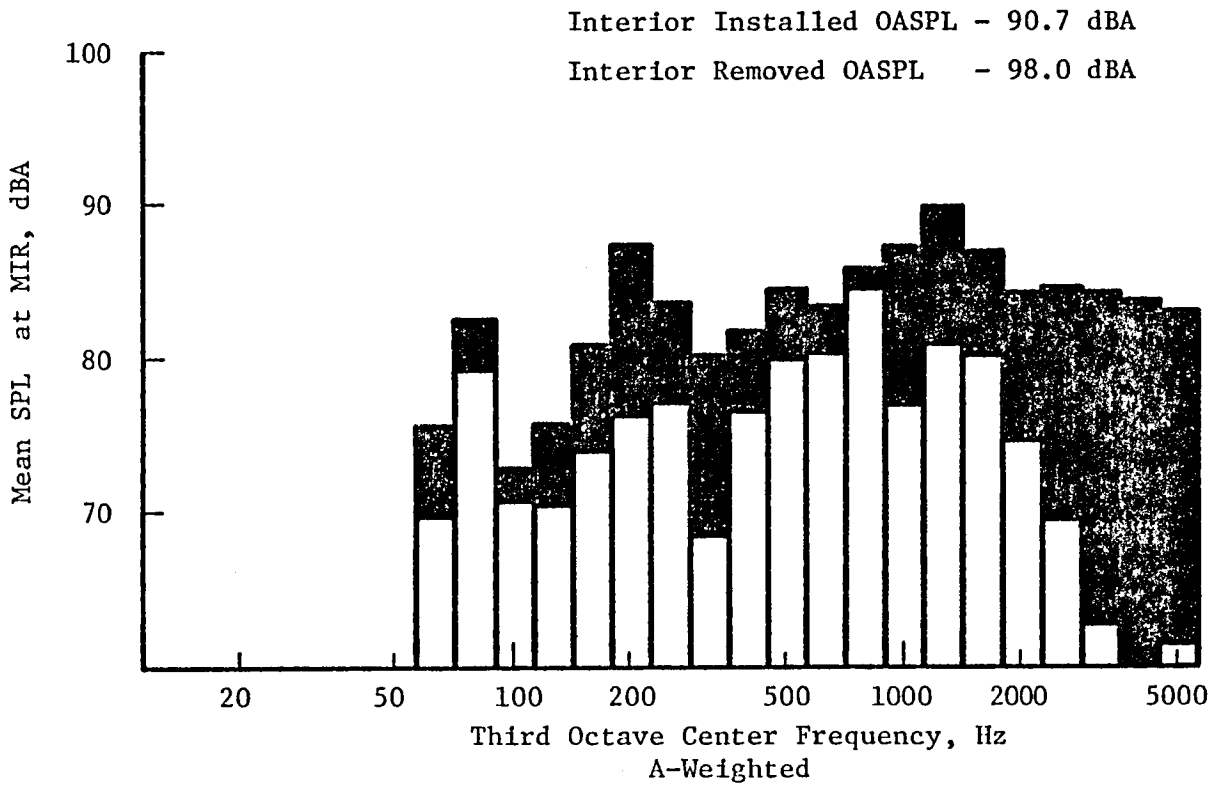

FIGURE 23. ENGINE ALONE A-WEIGHTED ONE-THIRD OCTAVE SPL AT MIR, 2160 RPM.

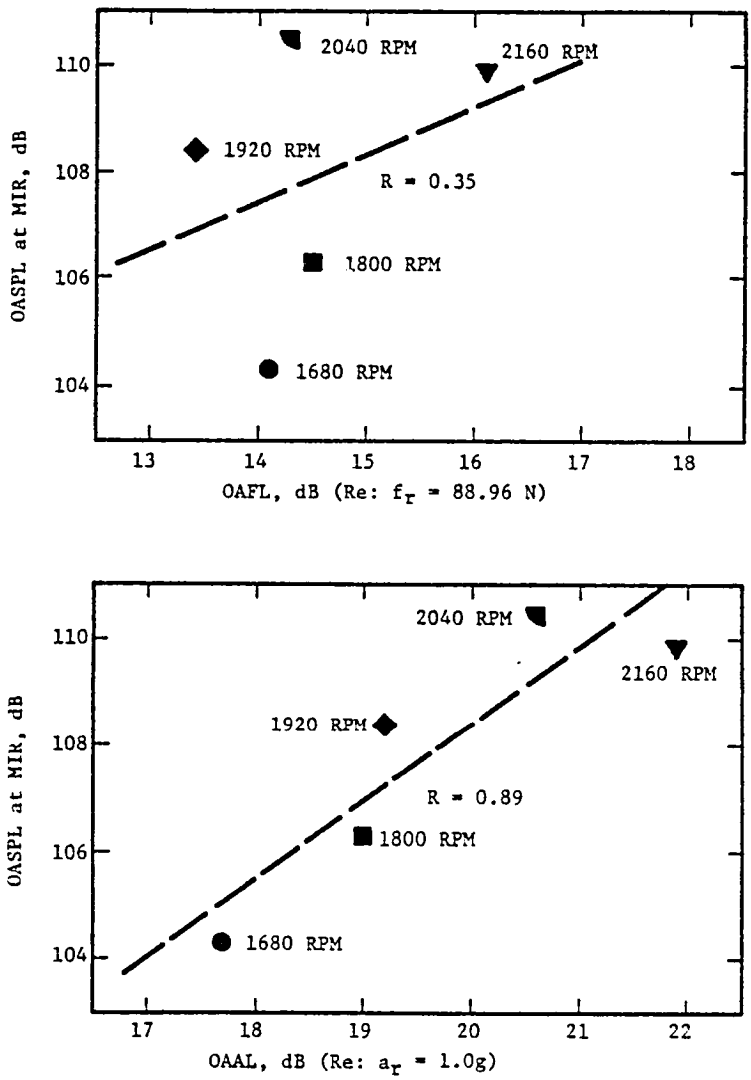

FIGURE 24. CORRELATION OF OASPL AT MIR TO OVERALL ENGINE FORCE AND ACCELERATION LEVELS.

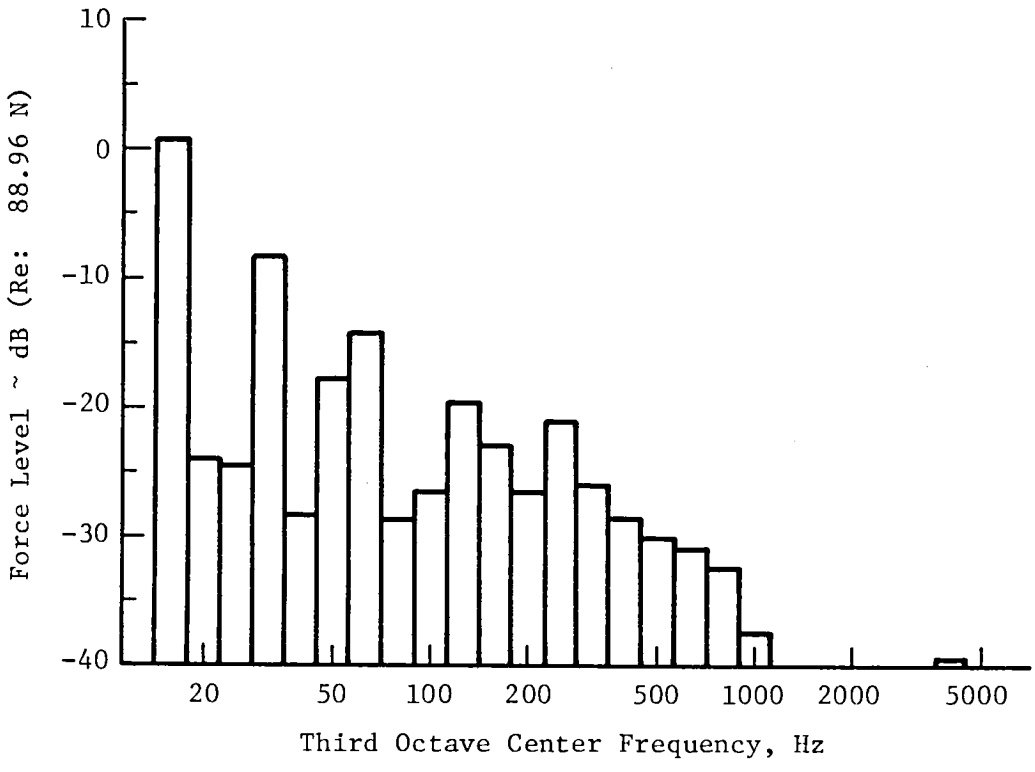

(a) 1920 rpm

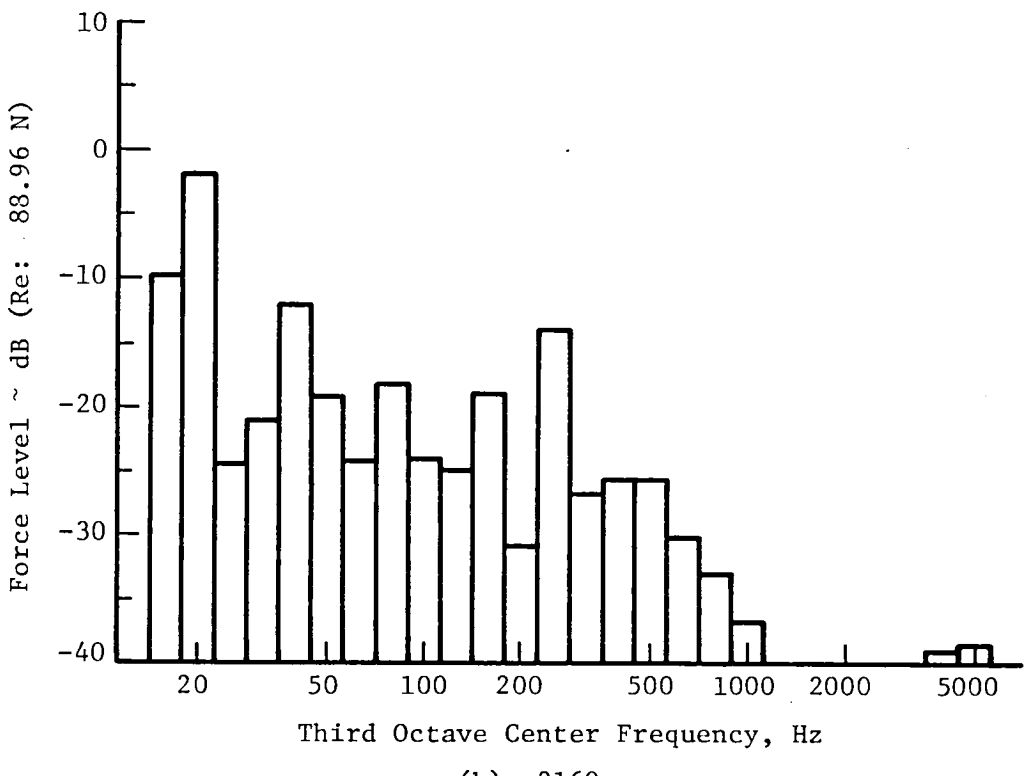

(b) 2160 rpm

FIGURE 25. ONE-THIRD OCTAVE FORCE LEVELS IN STRUT #1, 1920 AND 2160 RPM.

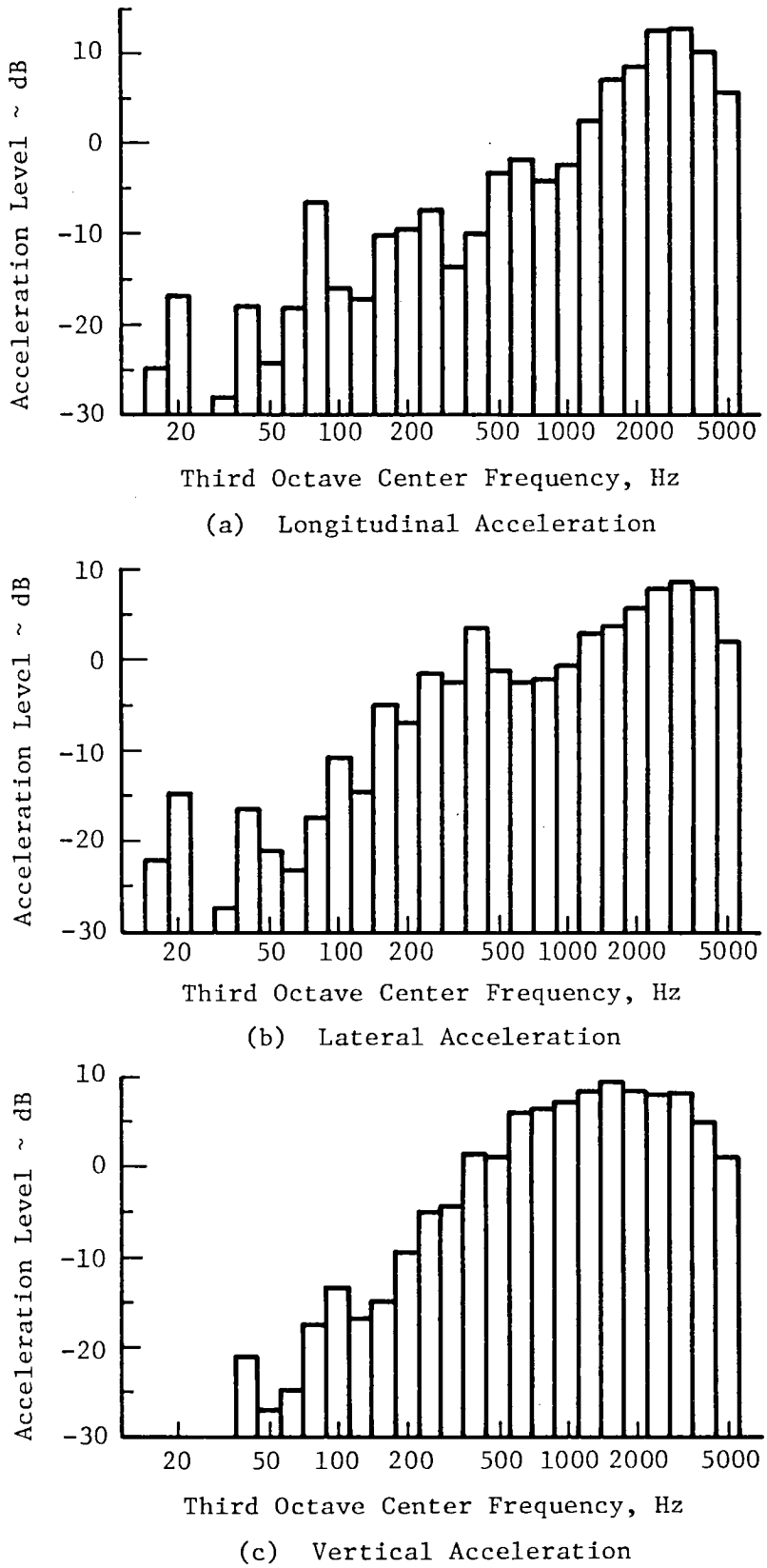

FIGURE 26. ENGINE ONE-THIRD OCTAVE ACCELERATION SPECTRA, 2160 RPM.

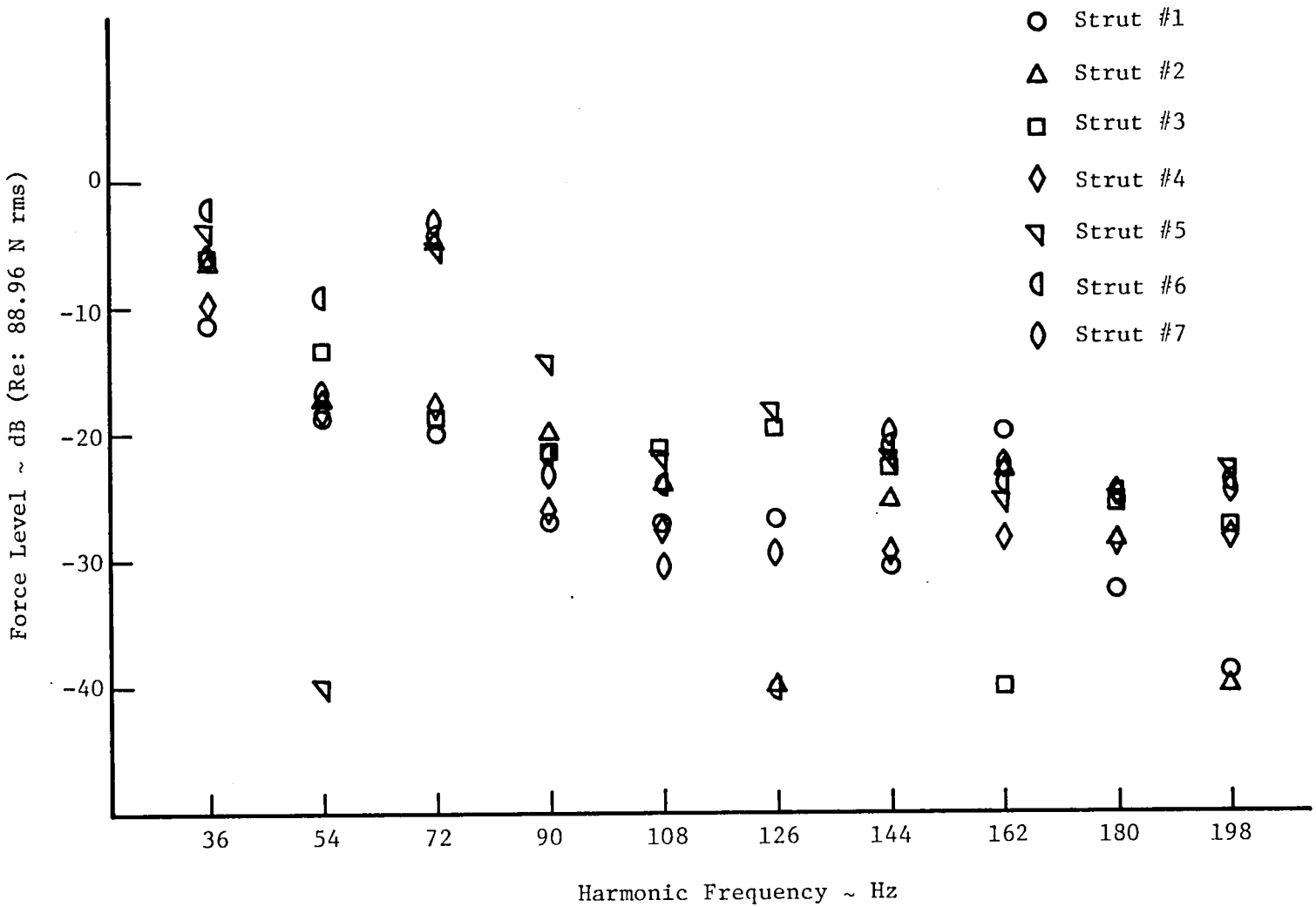

FIGURE 27. ENGINE MOUNT STRUT FORCES, 2160 RPM.

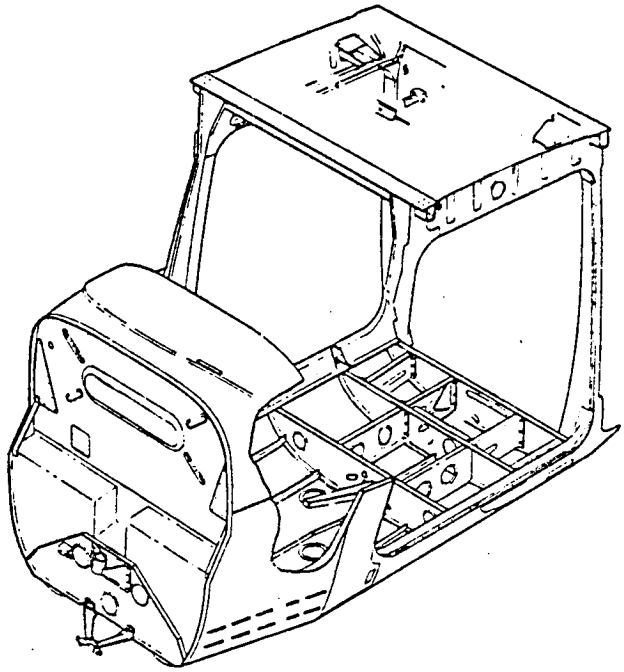

a) Front and Center Section Assembly

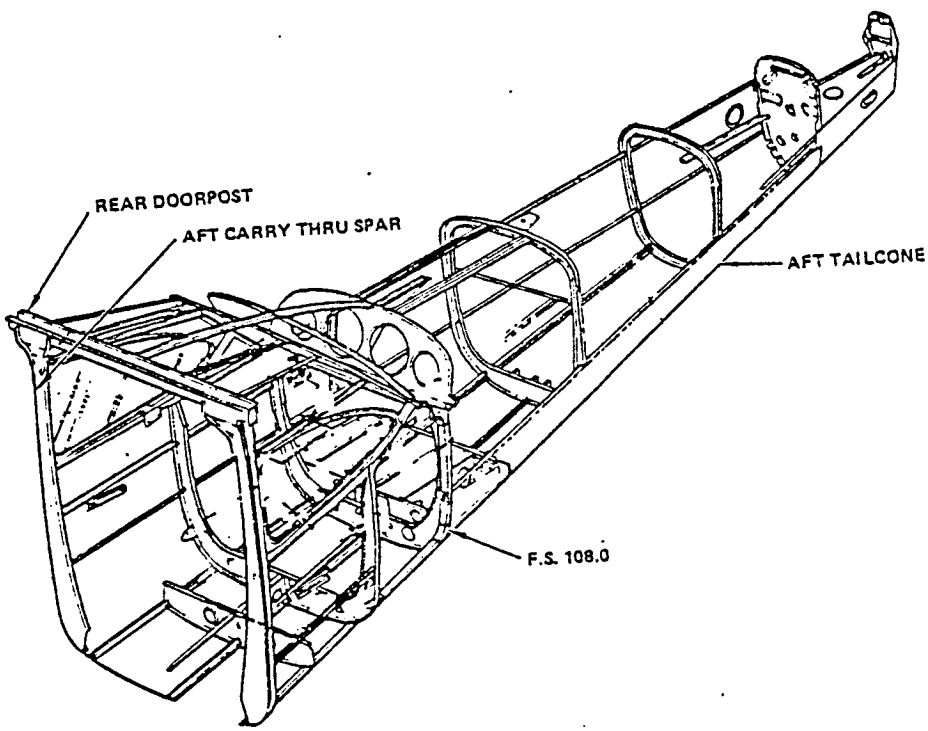

b) Aft Cabin and Tailcone Assembly

FIGURE 28. MODEL 172 PRIMARY FUSELAGE STRUCTURE

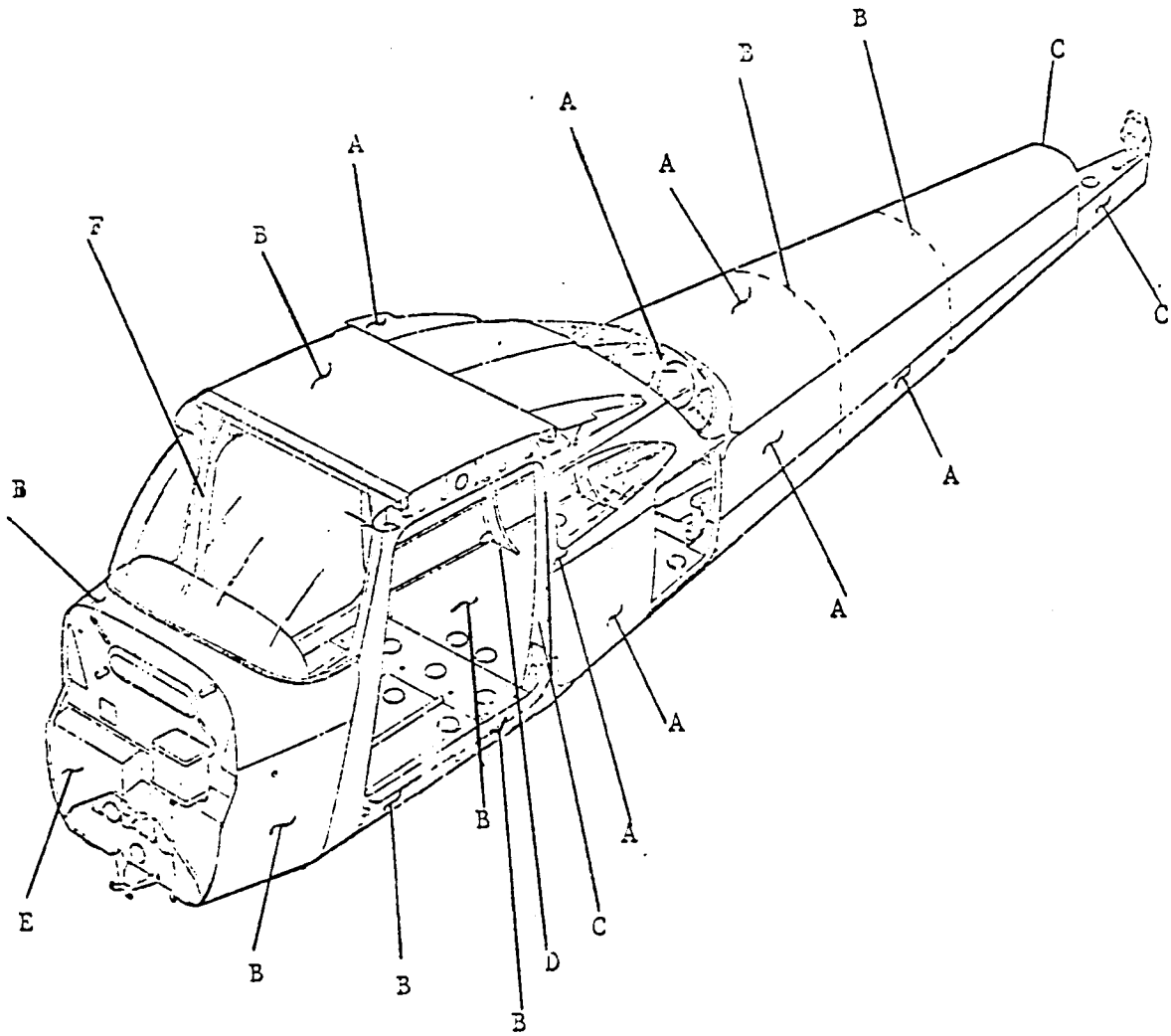

	Skin Thickness (cm)	(in.)	Material
A	0.0635	(0.025)	Aluminum
B	0.0813	(0.032)	Aluminum
C	0.1016	(0.040)	Aluminum
D	0.1295	(0.051)	Aluminum
E	0.0457	(0.018)	Steel
F	0.2032	(0.080)	Plexiglass

FIGURE 29. FUSELAGE SKIN THICKNESS DISTRIBUTION.

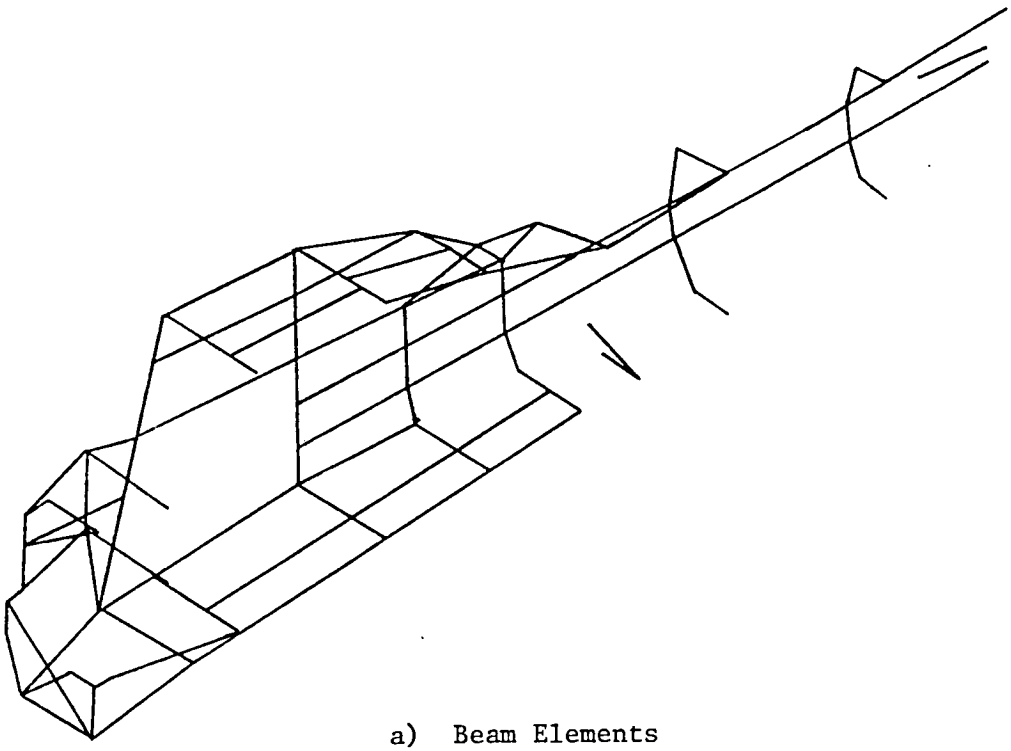

a) Beam Elements

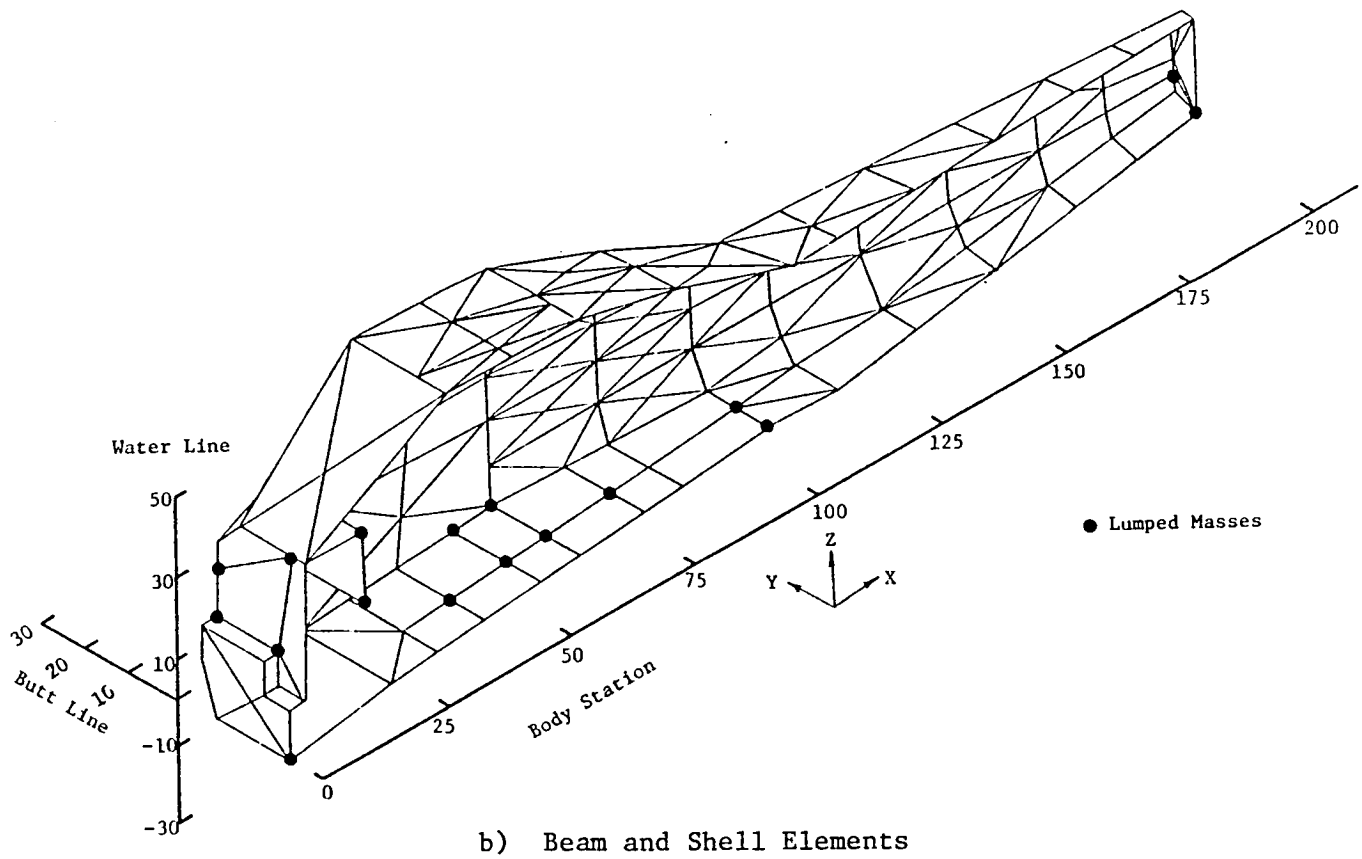

b) Beam and Shell Elements

FIGURE 30. STRUCTURAL FINITE ELEMENT MODEL OF CESSNA MODEL 172 FUSELAGE.

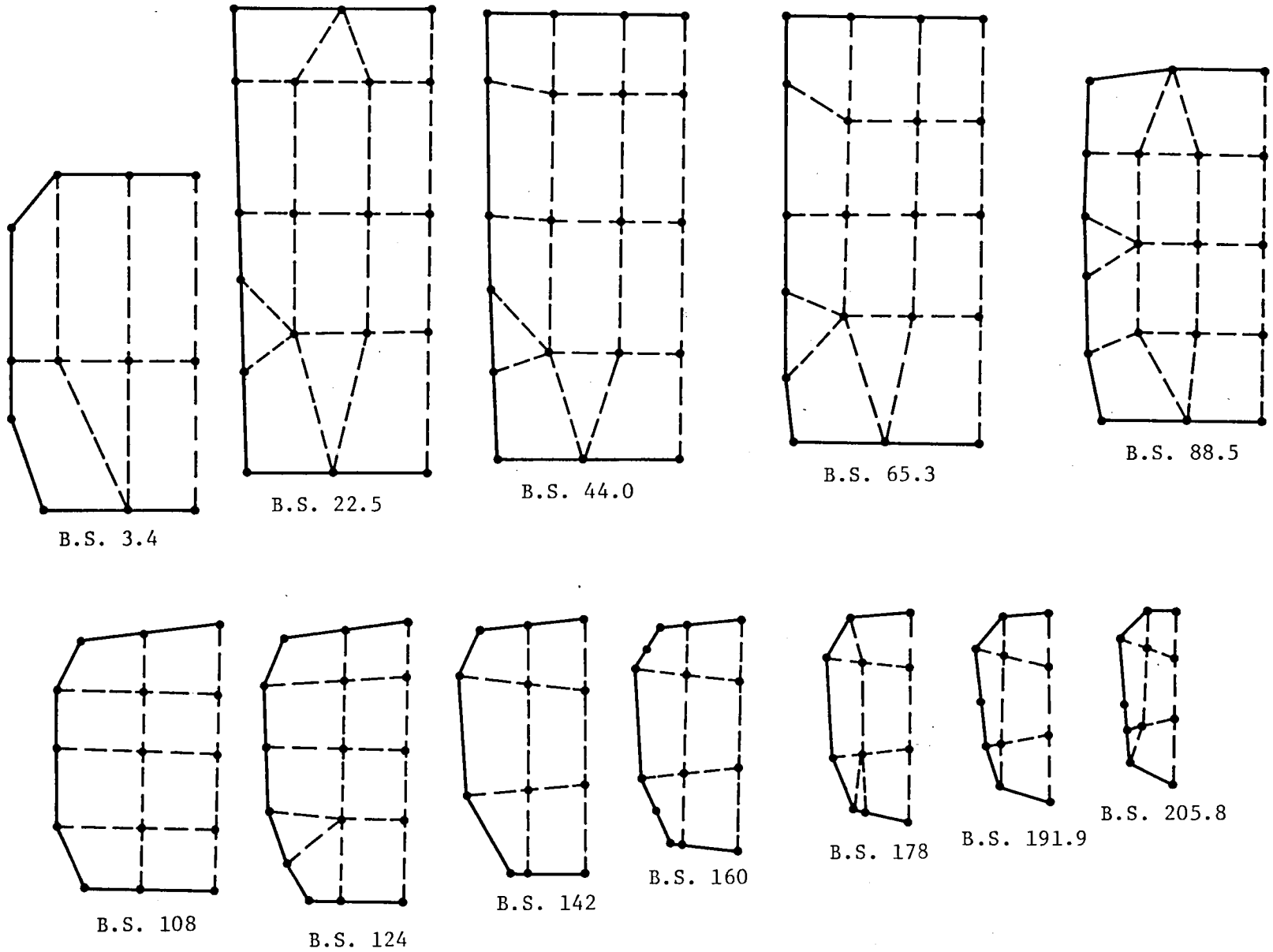

FIGURE 31. DISTRIBUTION OF ACOUSTIC NODE POINTS AT MAJOR FUSELAGE STATIONS.

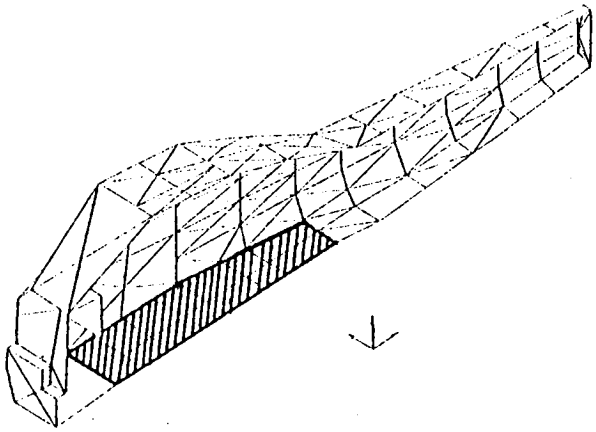

(a) Floor Panels, 1.04 meter^2

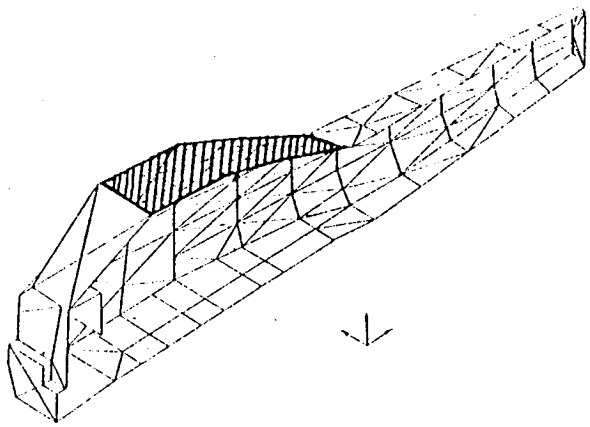

(b) Roof Panels, 1.02 meter^2

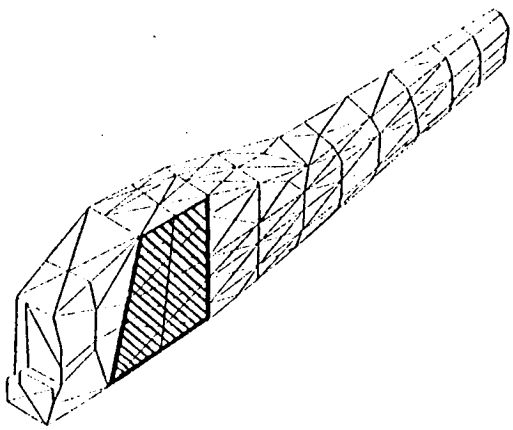

(c) Door Panels, 1.15 meter^2

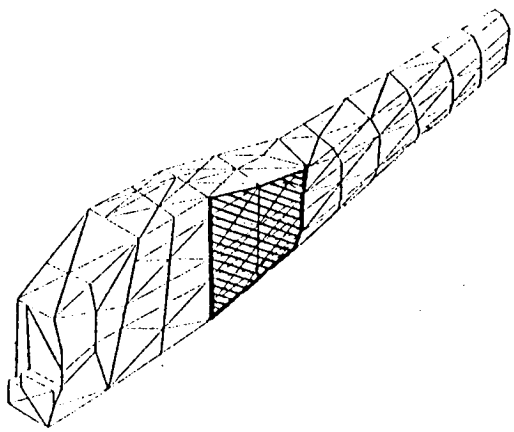

(d) Aft Side Panels, 1.07 meter^2

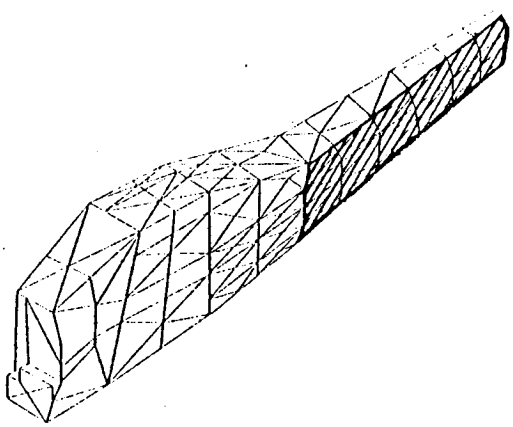

(e) Tail Cone Panels, 1.59 meter^2

FIGURE 32. FUSELAGE STRUCTURAL-ACOUSTIC MODEL ACTIVE PANEL AREAS.

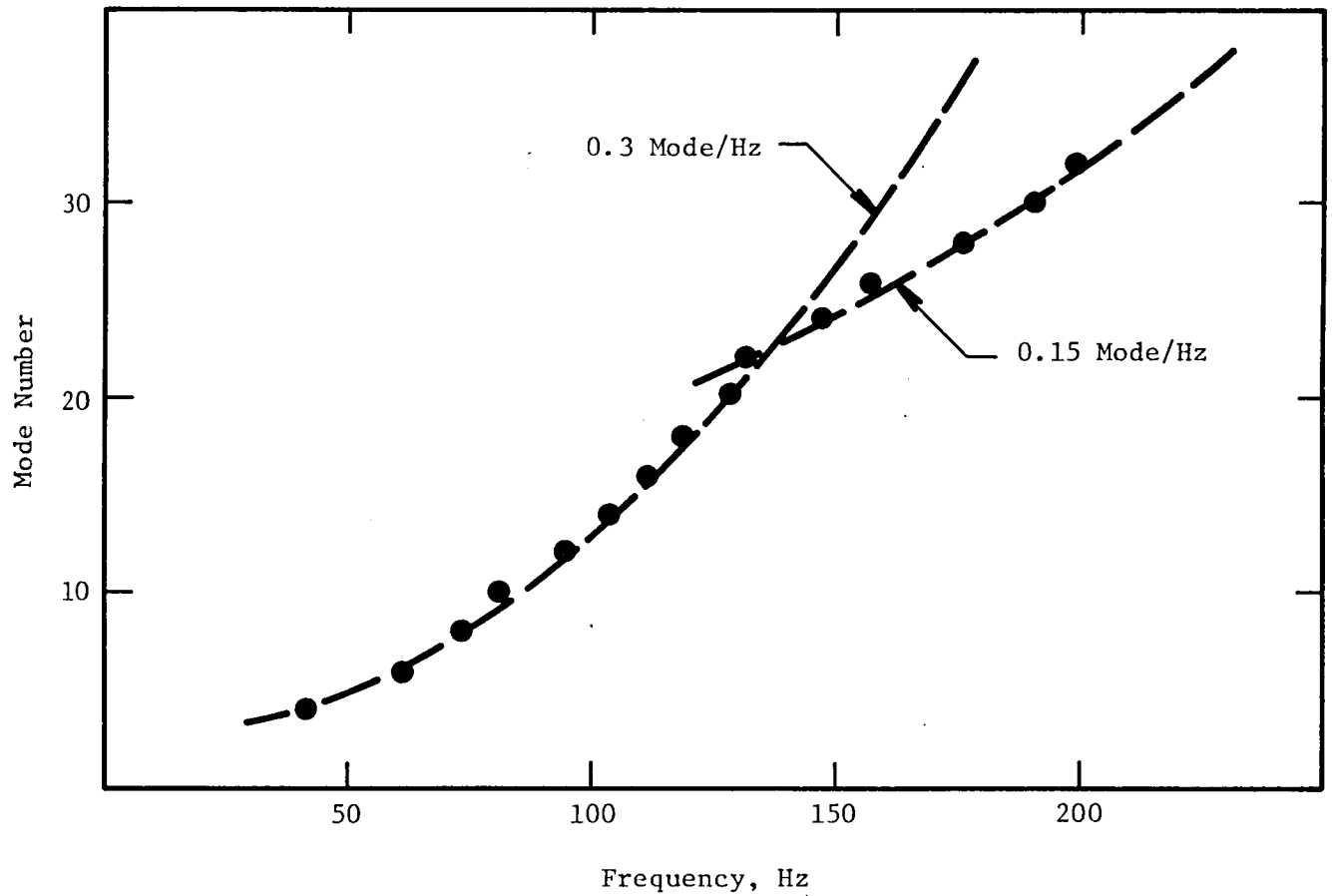

FIGURE 33. STRUCTURAL MODAL DENSITY.

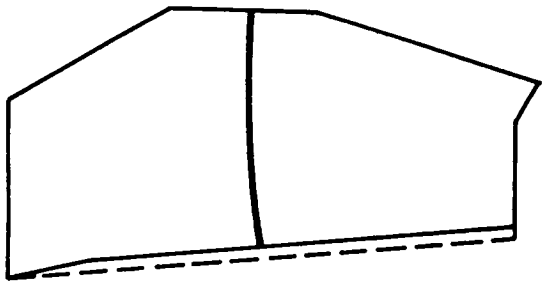

71.6 Hz

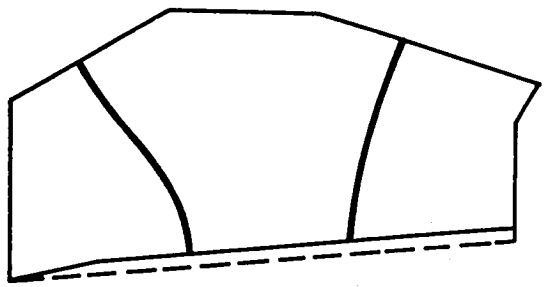

131.5 Hz

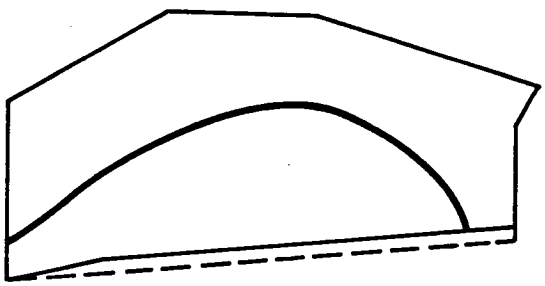

160.5 Hz

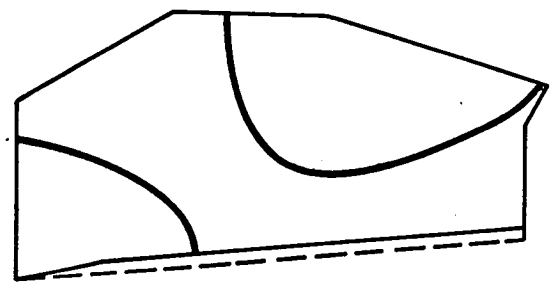

188.0 Hz

FIGURE 34. PREDICTED CABIN ONLY ACOUSTIC HARDWALLED MODES.

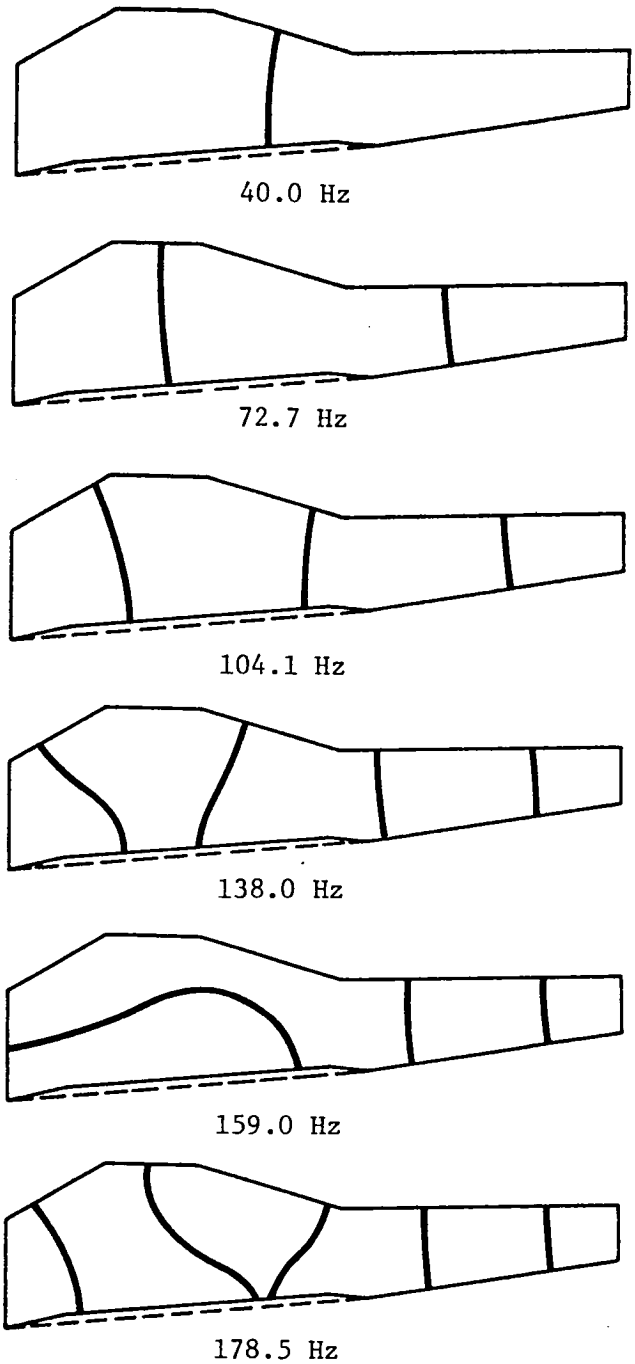

FIGURE 35. PREDICTED FULL FUSELAGE ACOUSTIC HARDWALLED MODES.

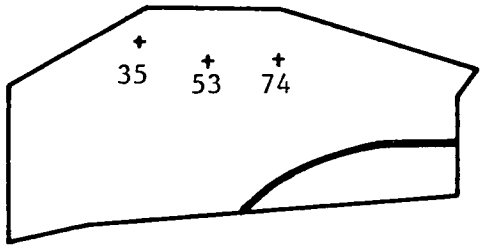

39.3 Hz

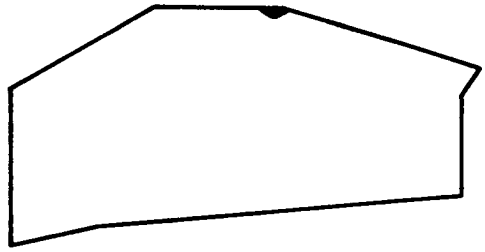

41.9 Hz

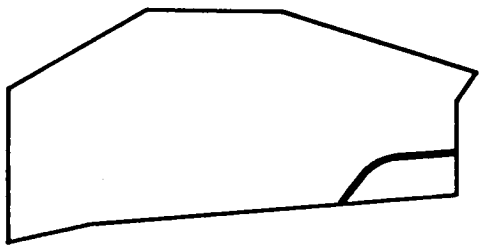

56.4 Hz

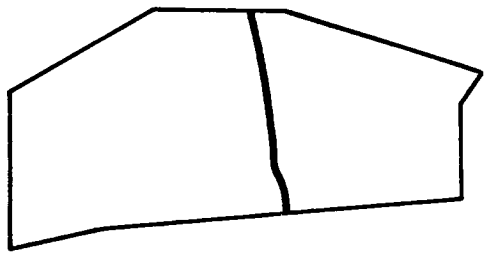

59.9 Hz

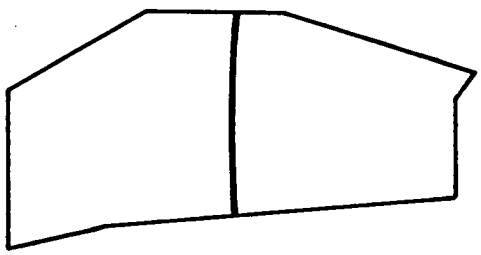

66.0 Hz

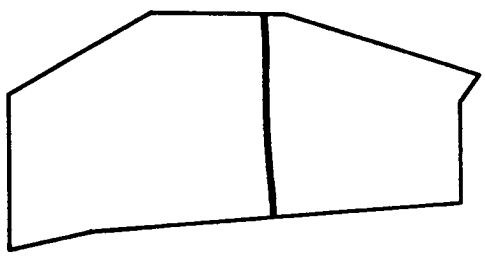

68.3 Hz

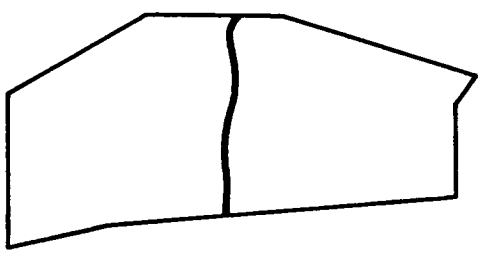

73.4 Hz

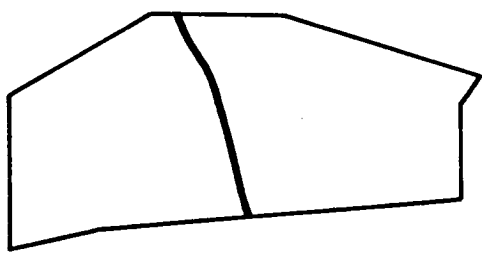

77.0 Hz

FIGURE 36. PREDICTED CABIN ONLY COUPLED STRUCTURAL-ACOUSTIC MODES.

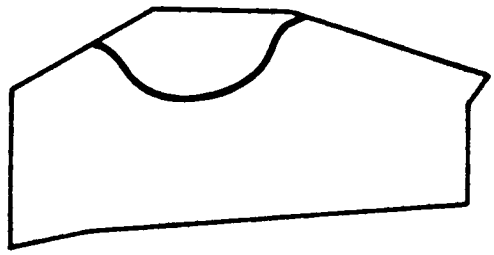

80.7 Hz

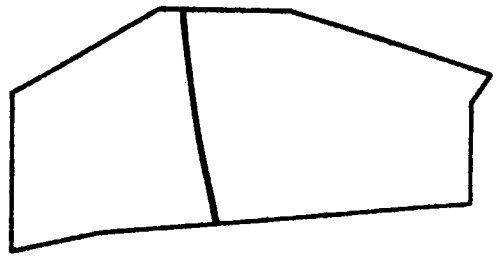

83.8 Hz

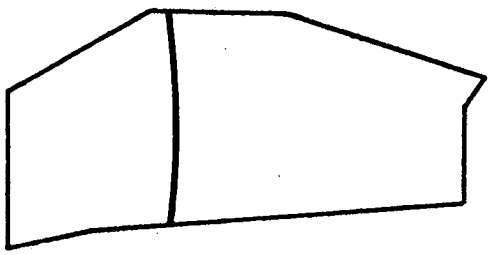

96.4 Hz

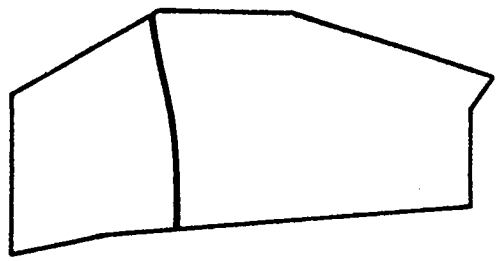

100.7 Hz

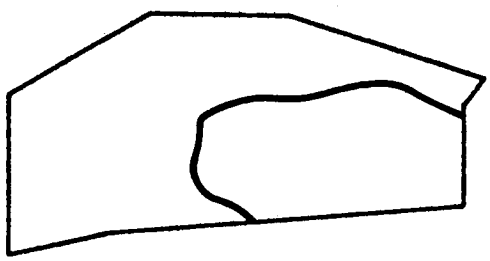

103.4 Hz

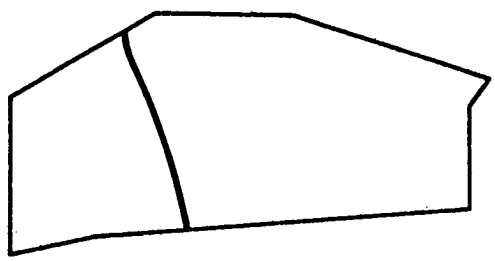

108.2 Hz

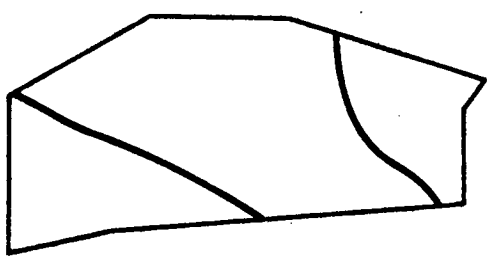

112.1 Hz

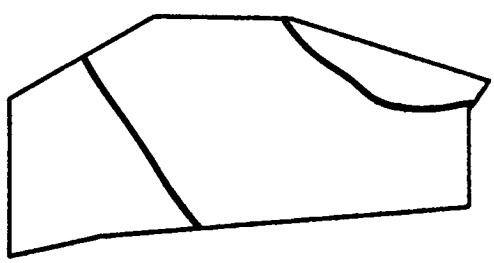

115.4 Hz

FIGURE 36 (CONT.). PREDICTED CABIN ONLY COUPLED STRUCTURAL-ACOUSTIC MODES.

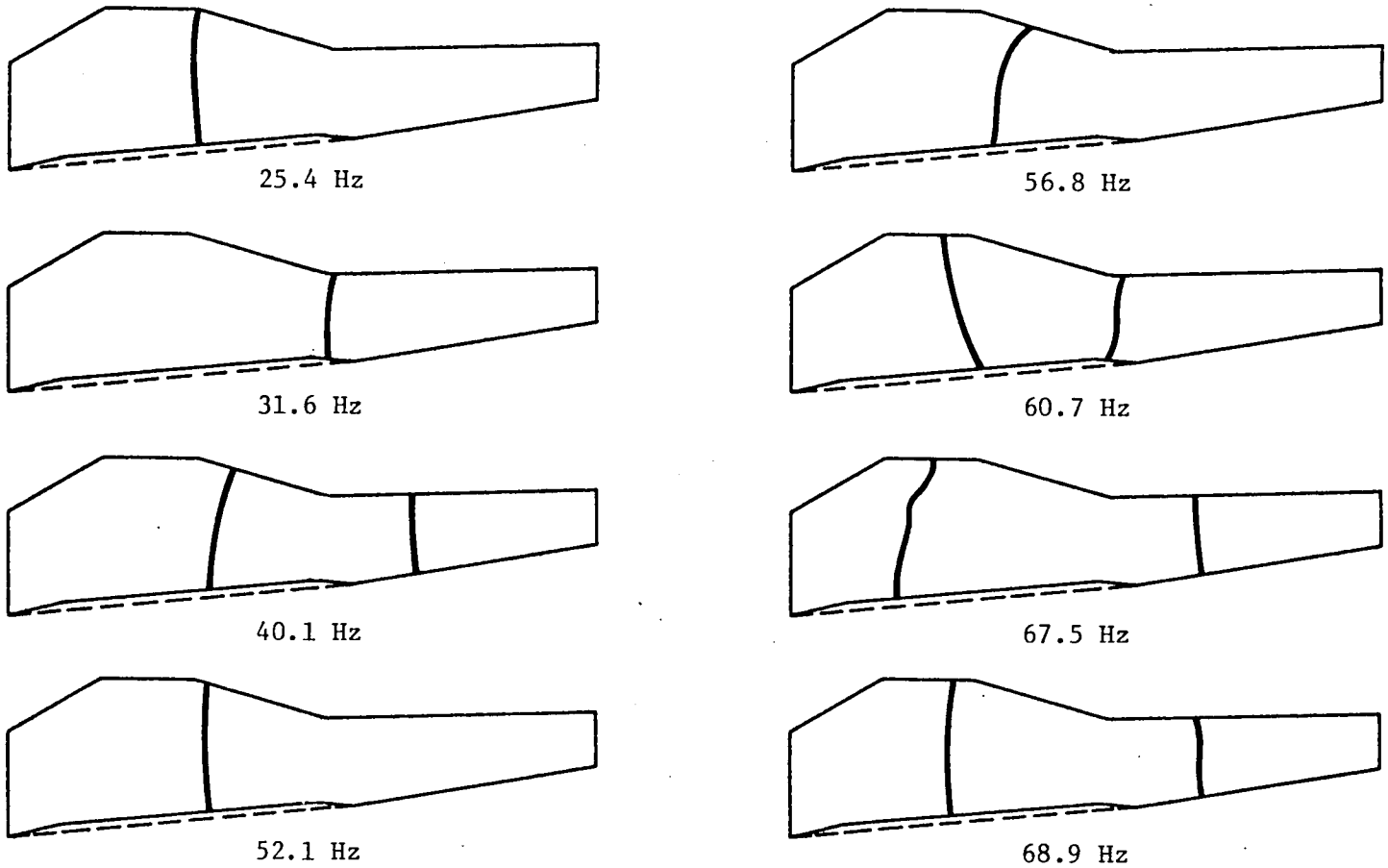

FIGURE 37. PREDICTED FULL FUSELAGE COUPLED STRUCTURAL-ACOUSTIC MODES.

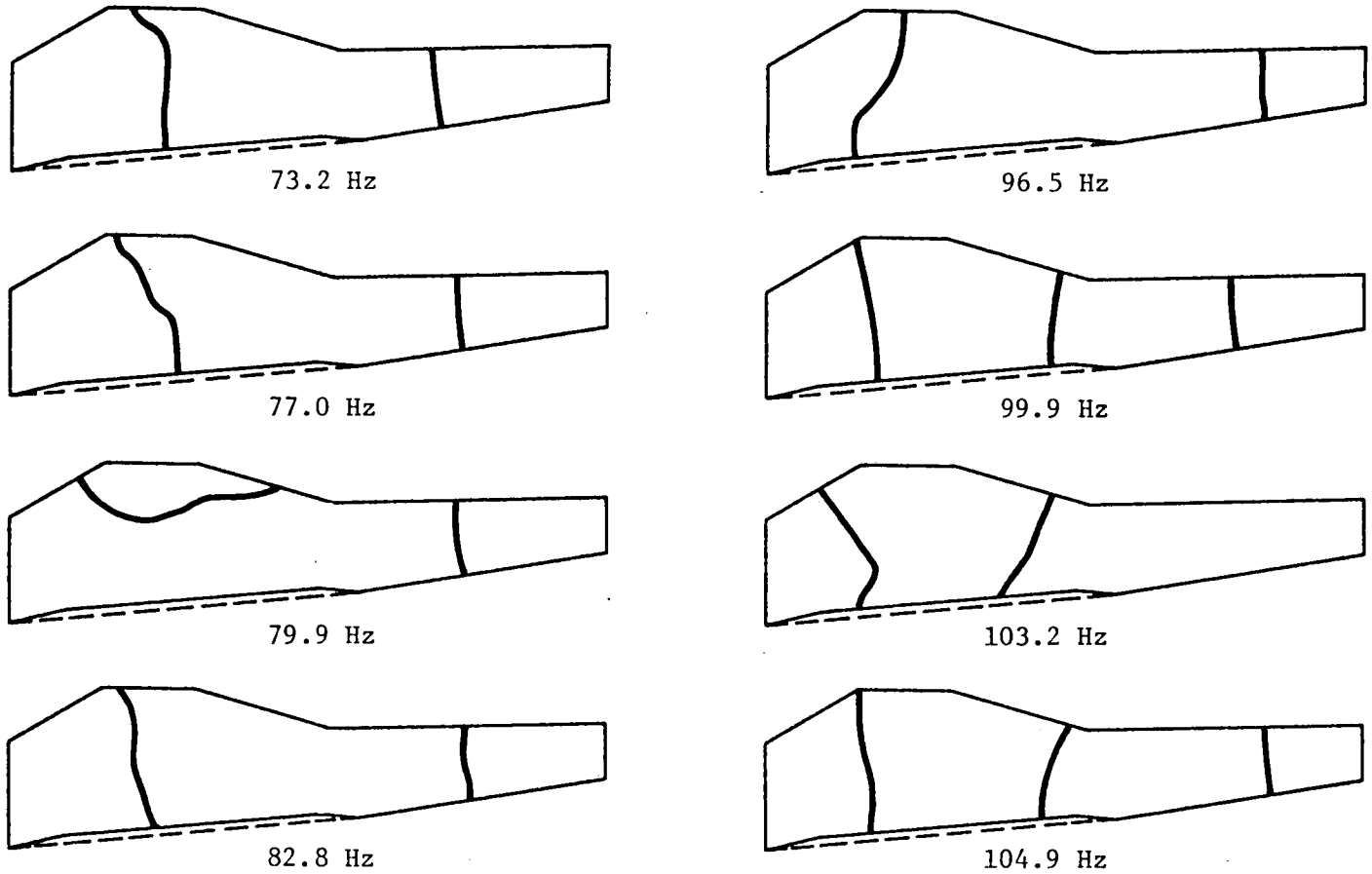

FIGURE 37 (CONT.). PREDICTED FULL FUSELAGE COUPLED STRUCTURAL-ACOUSTIC MODES.

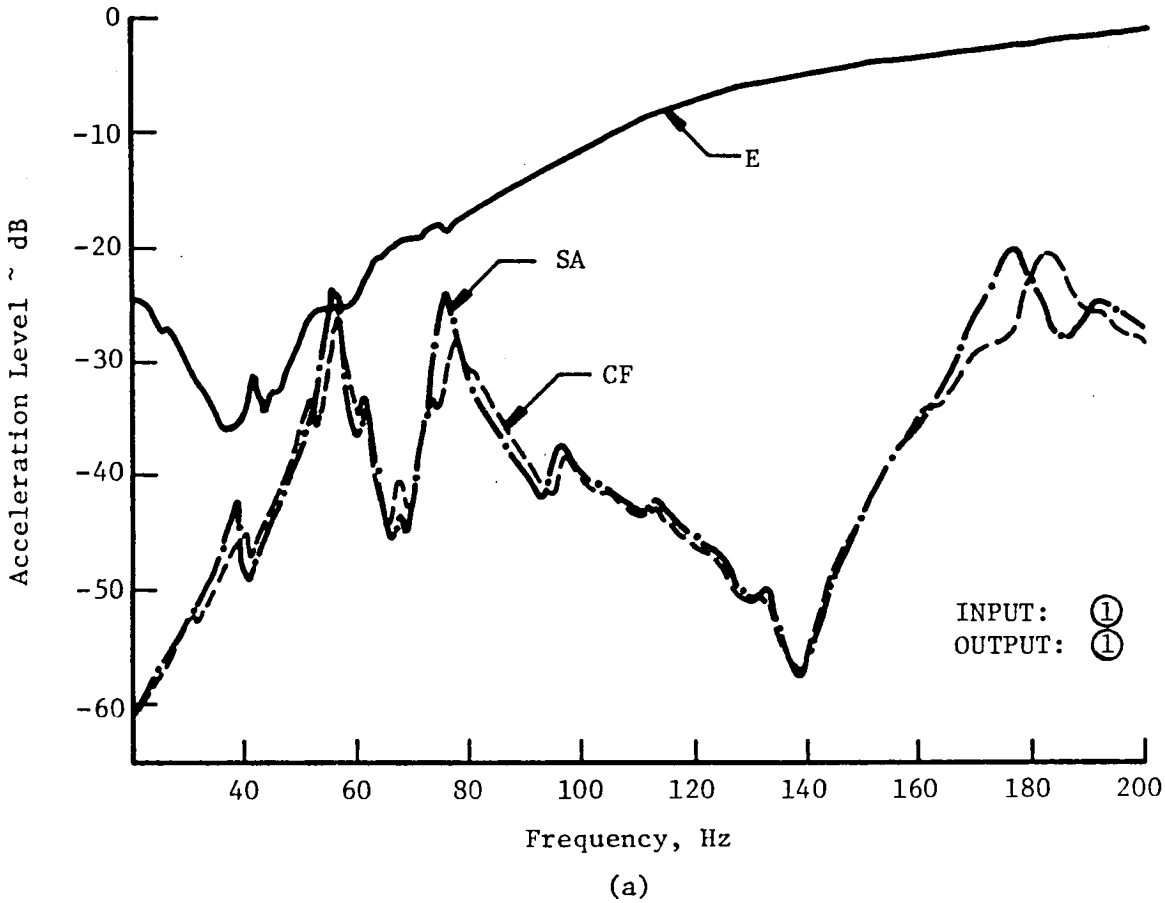

(a)

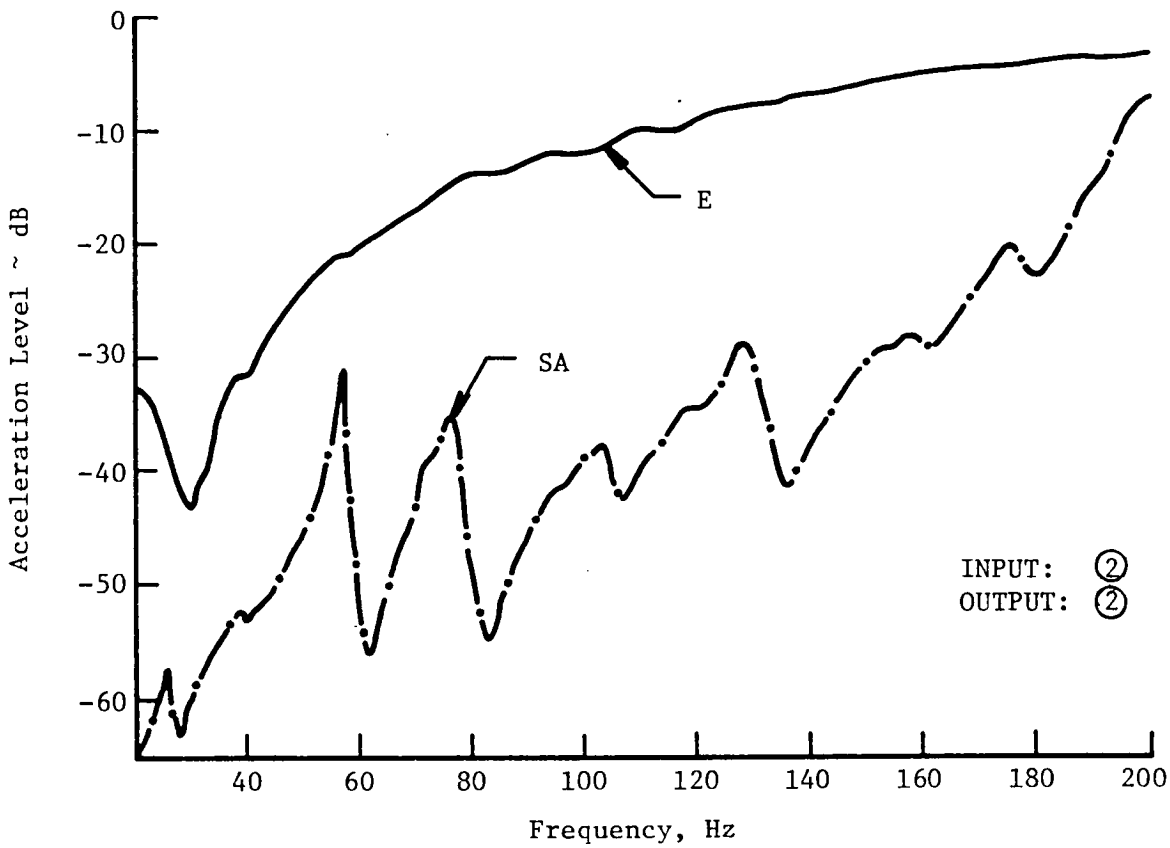

(b)

FIGURE 38. DRIVING POINT ACCELERATION RESPONSES FOR LONGITUDINAL HARMONIC INPUT OF 44.48 N RMS.

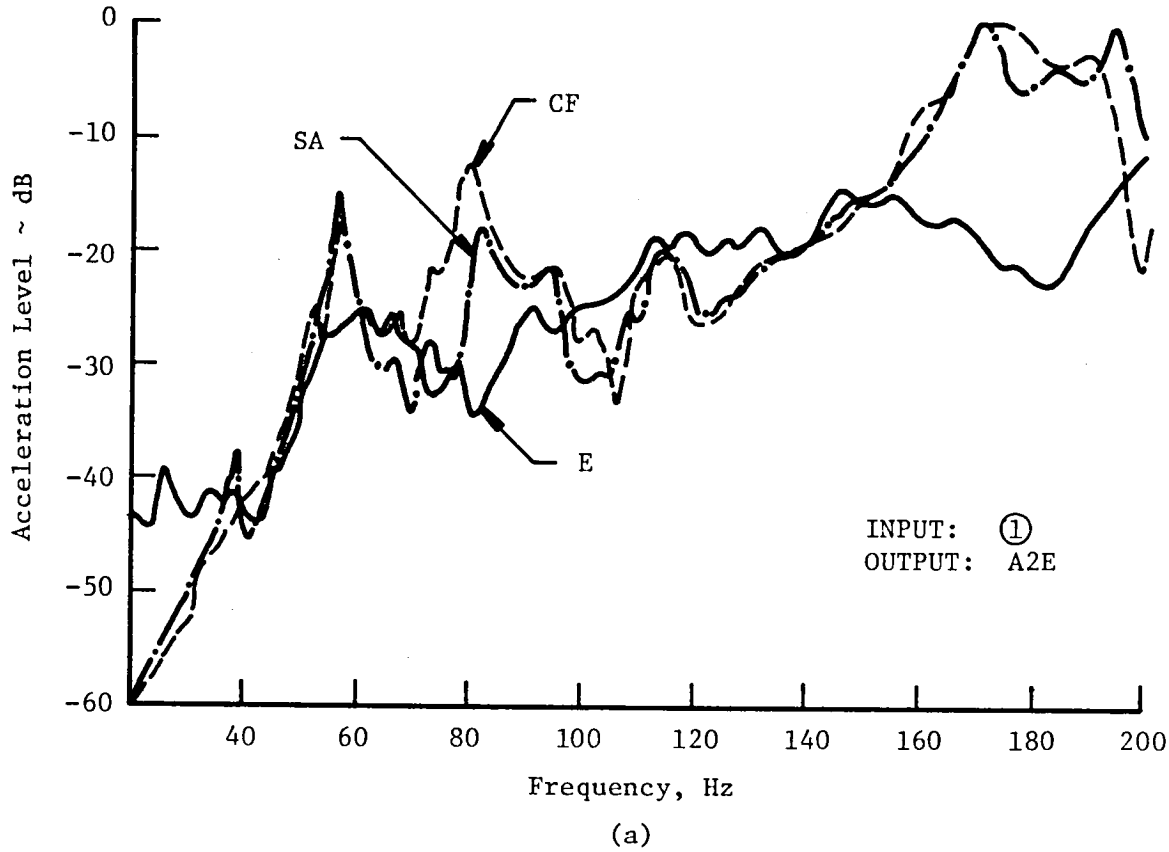

(a)

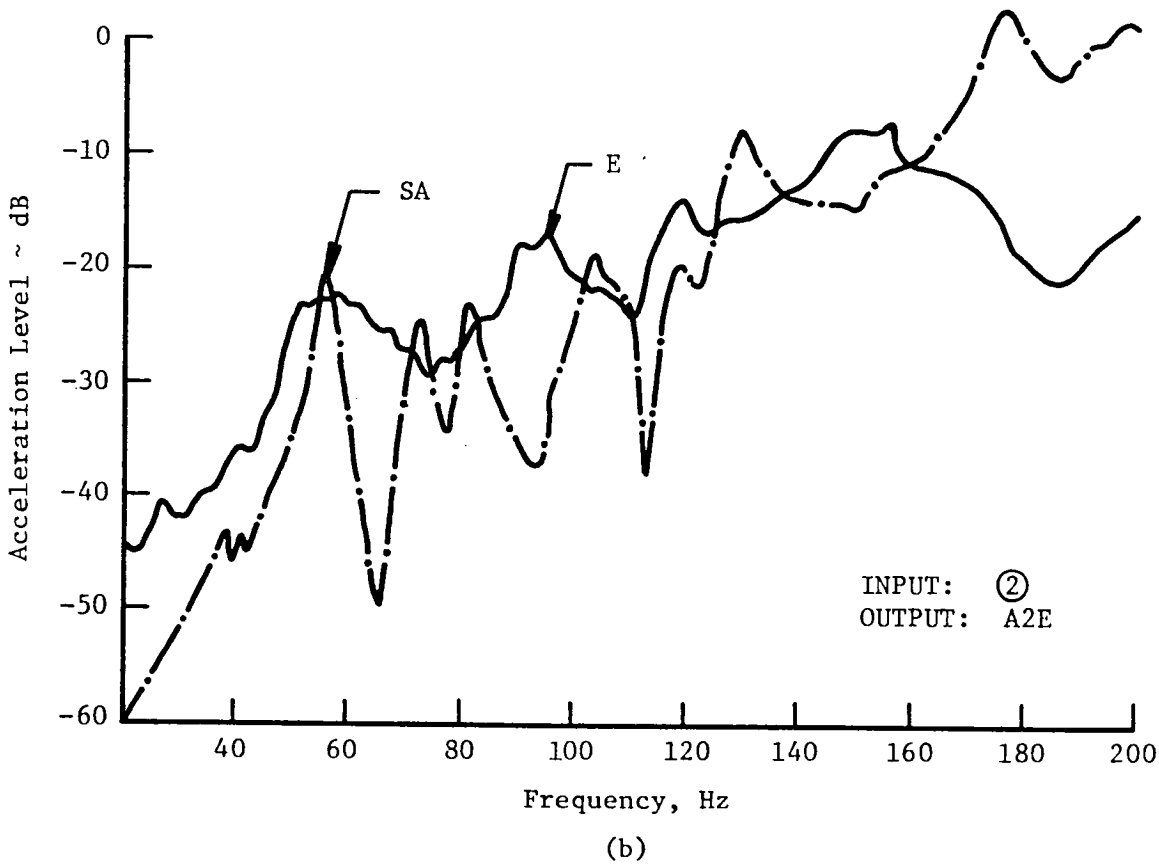

(b)

FIGURE 39. VERTICAL ACCELERATION RESPONSE AT A2E FOR LONGITUDINAL HARMONIC INPUT OF 44.48 N RMS.

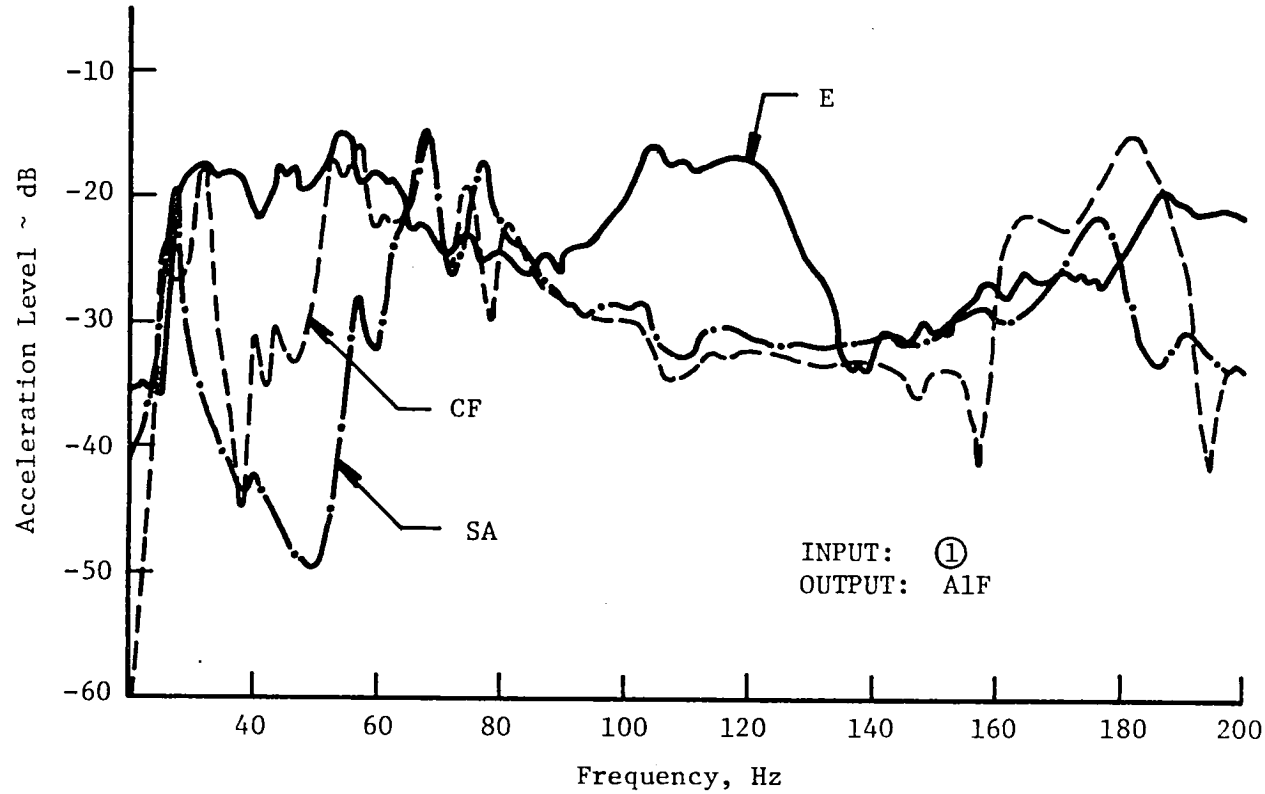

(a)

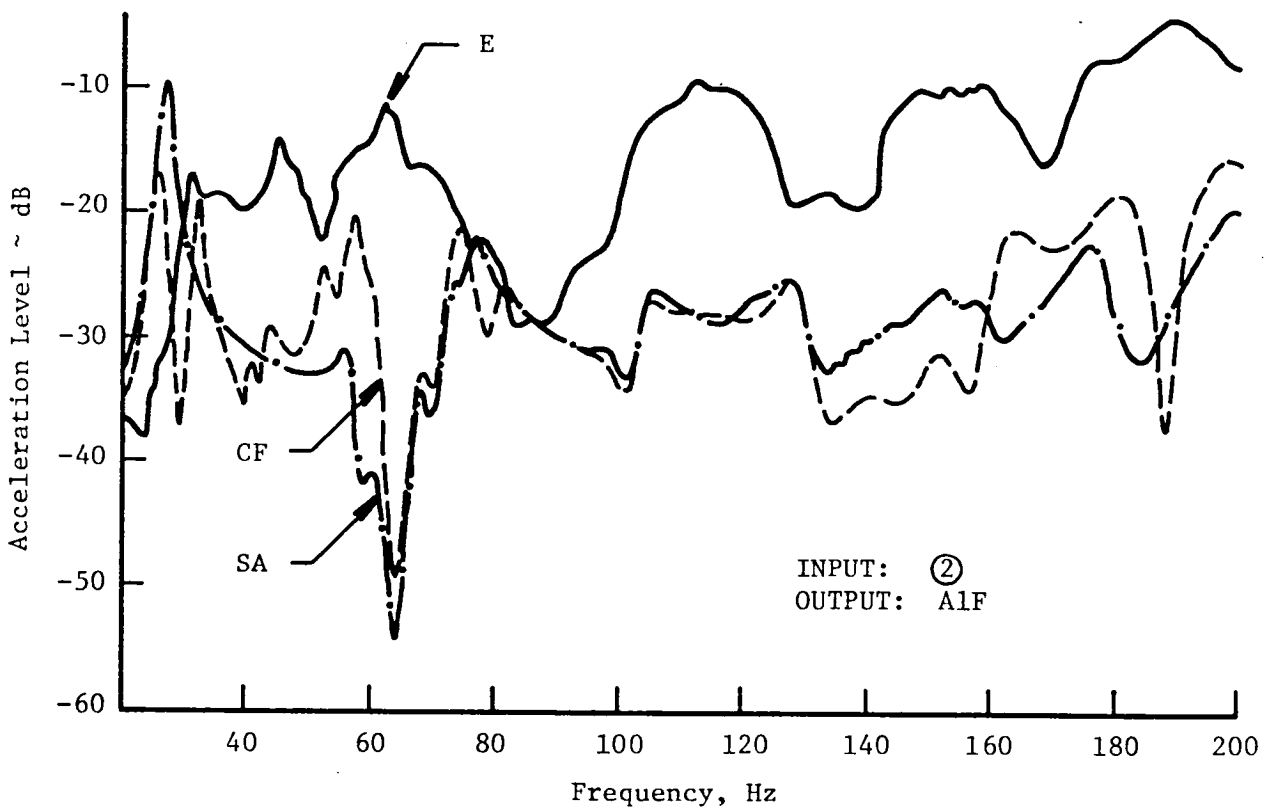

(b)

FIGURE 40. LATERAL ACCELERATION RESPONSE AT A1F FOR LONGITUDINAL HARMONIC INPUT OF 44.48 N RMS.

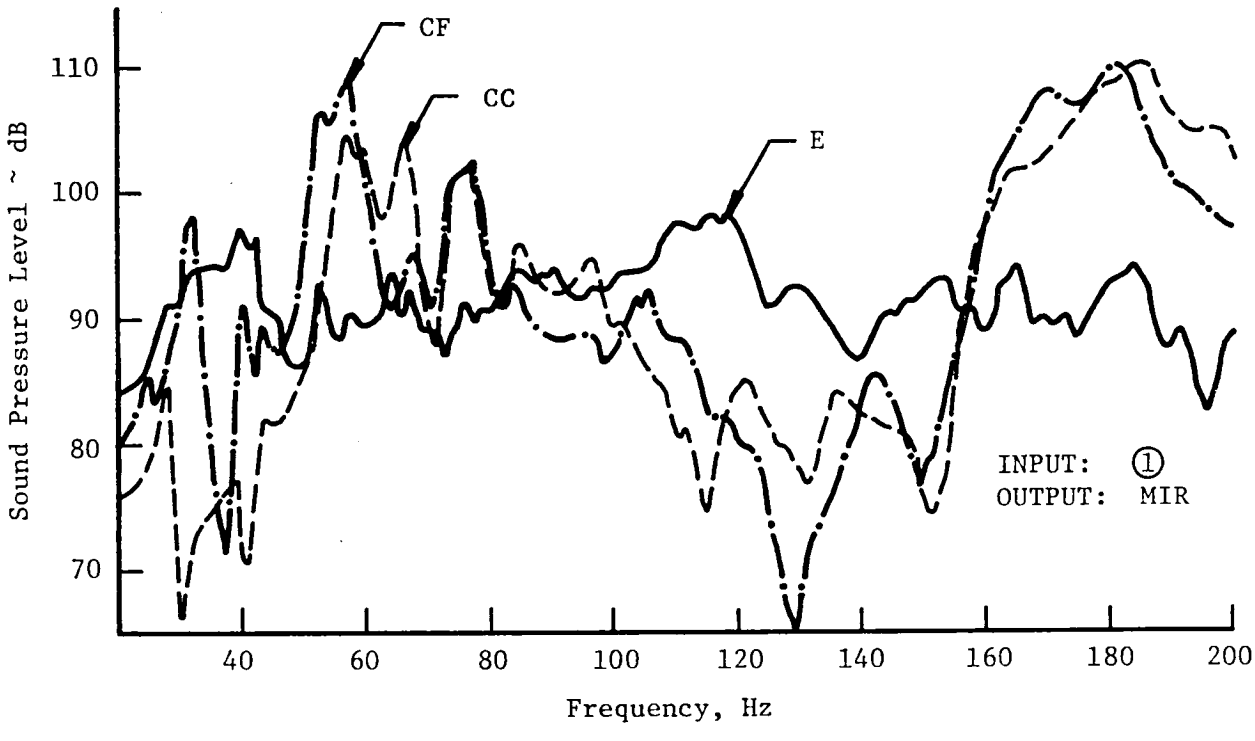

(a)

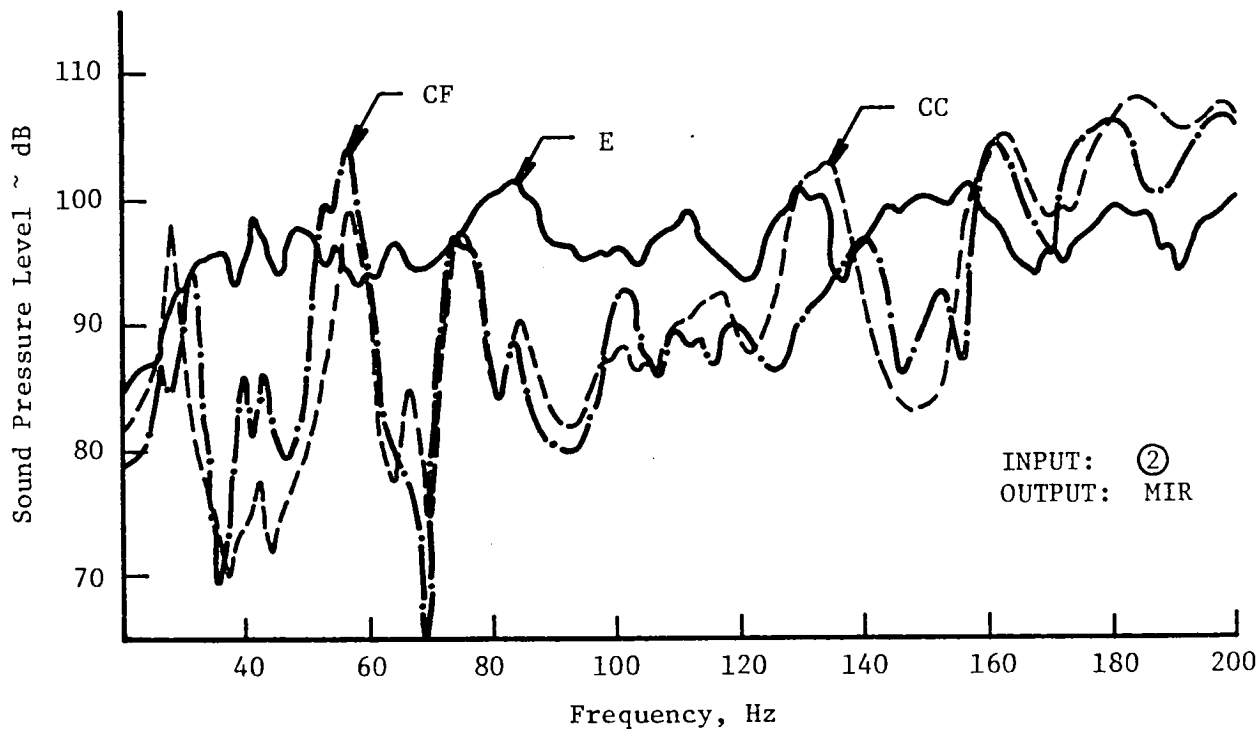

(b)

FIGURE 41. SOUND PRESSURE LEVEL RESPONSE AT MIR FOR LONGITUDINAL HARMONIC INPUT OF 44.48 N RMS.

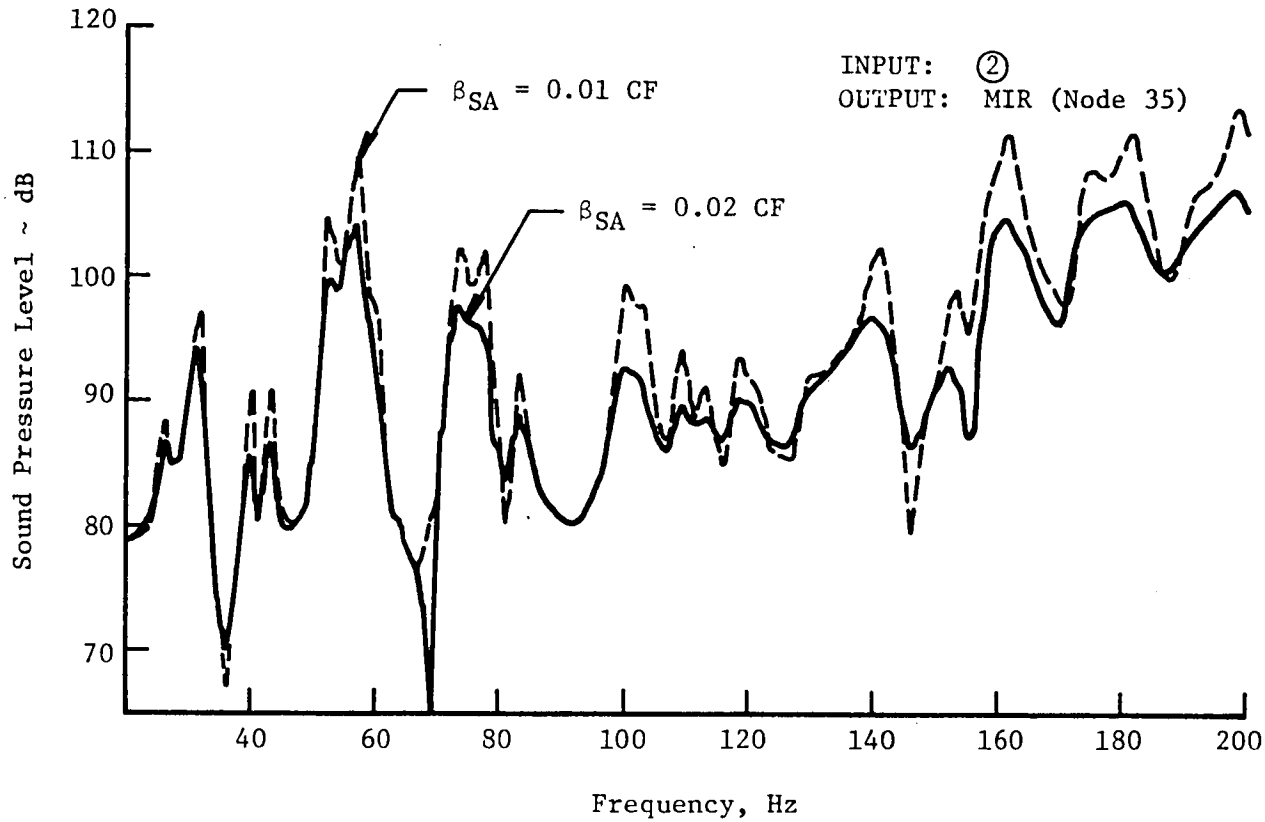

FIGURE 42. SOUND PRESSURE LEVEL RESPONSE AT MIR: EFFECT OF MODAL DAMPING.

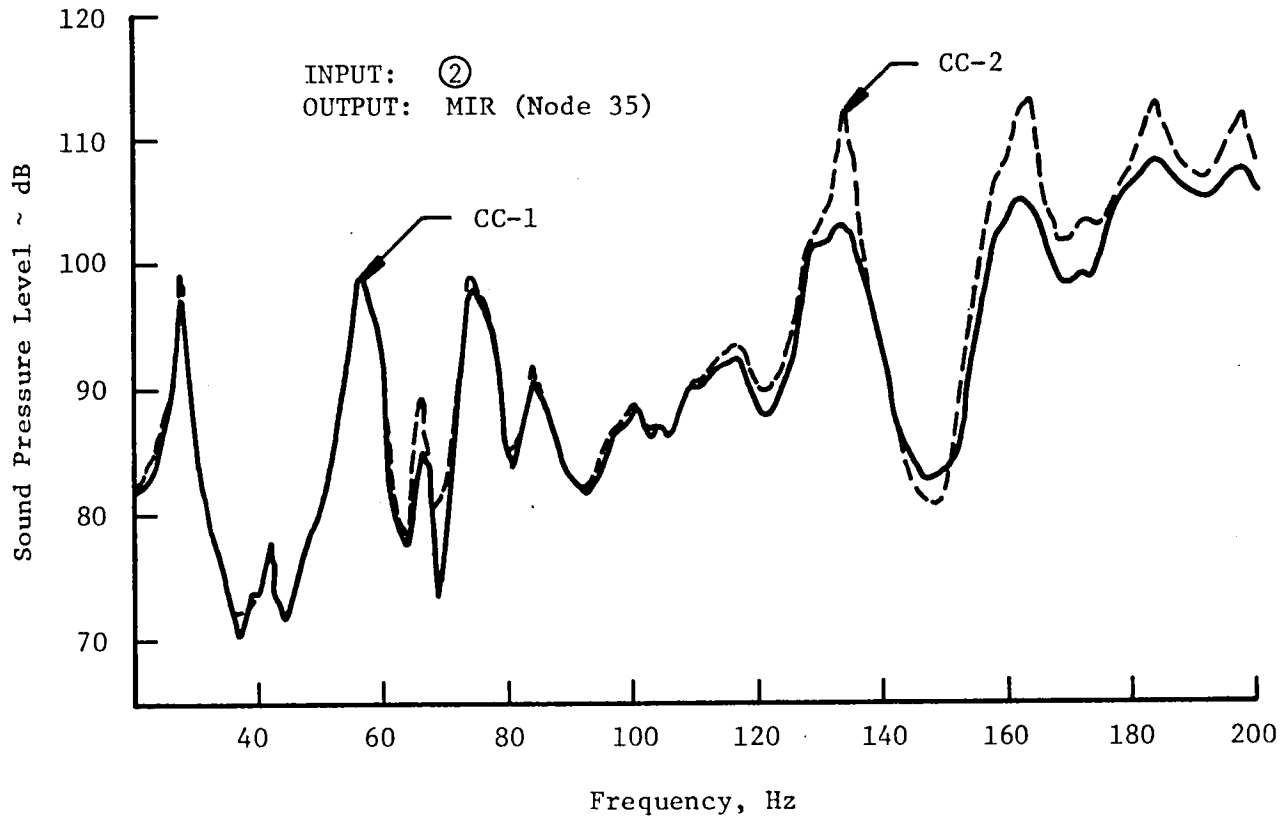

FIGURE 43. SOUND PRESSURE LEVEL RESPONSE AT MIR: EFFECT OF DAMPING REPRESENTATION.

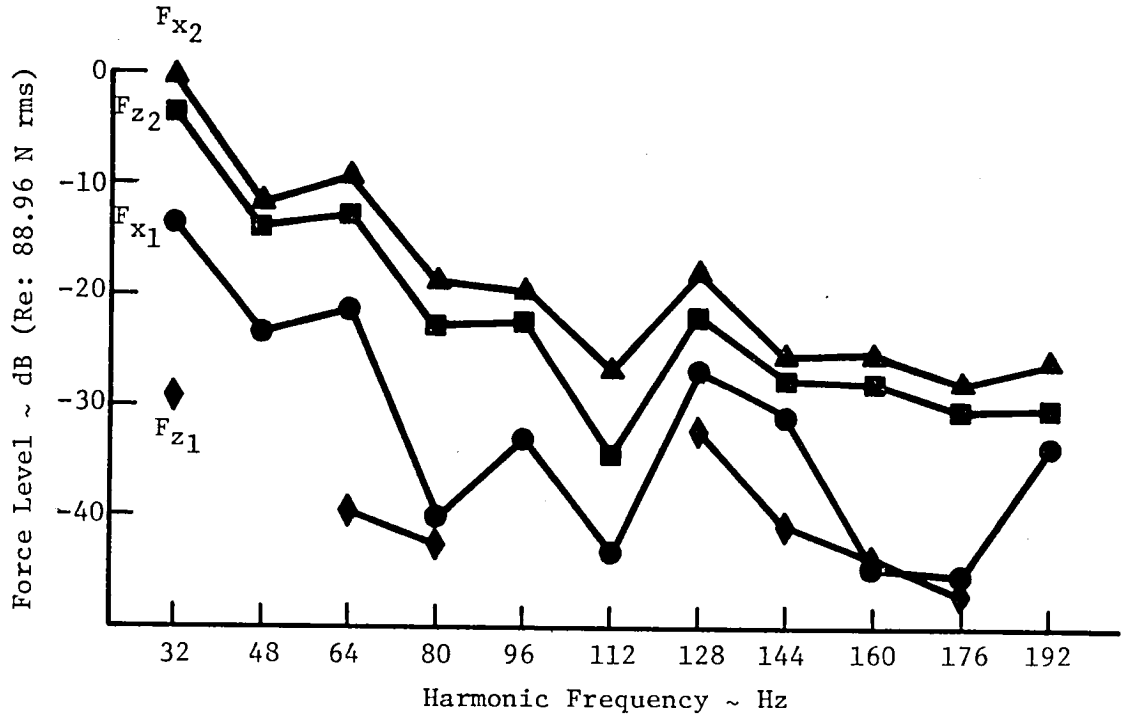

a) 1920 rpm

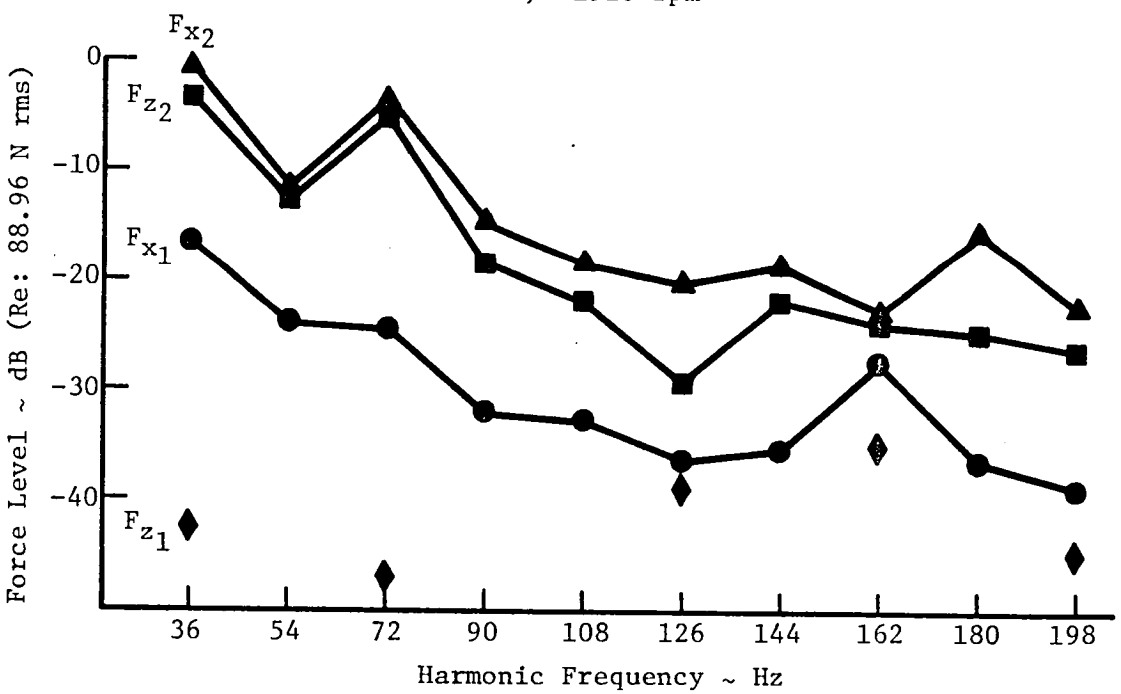

b) 2160 rpm

FIGURE 44. ENGINE SYMMETRIC DRIVING FORCES.

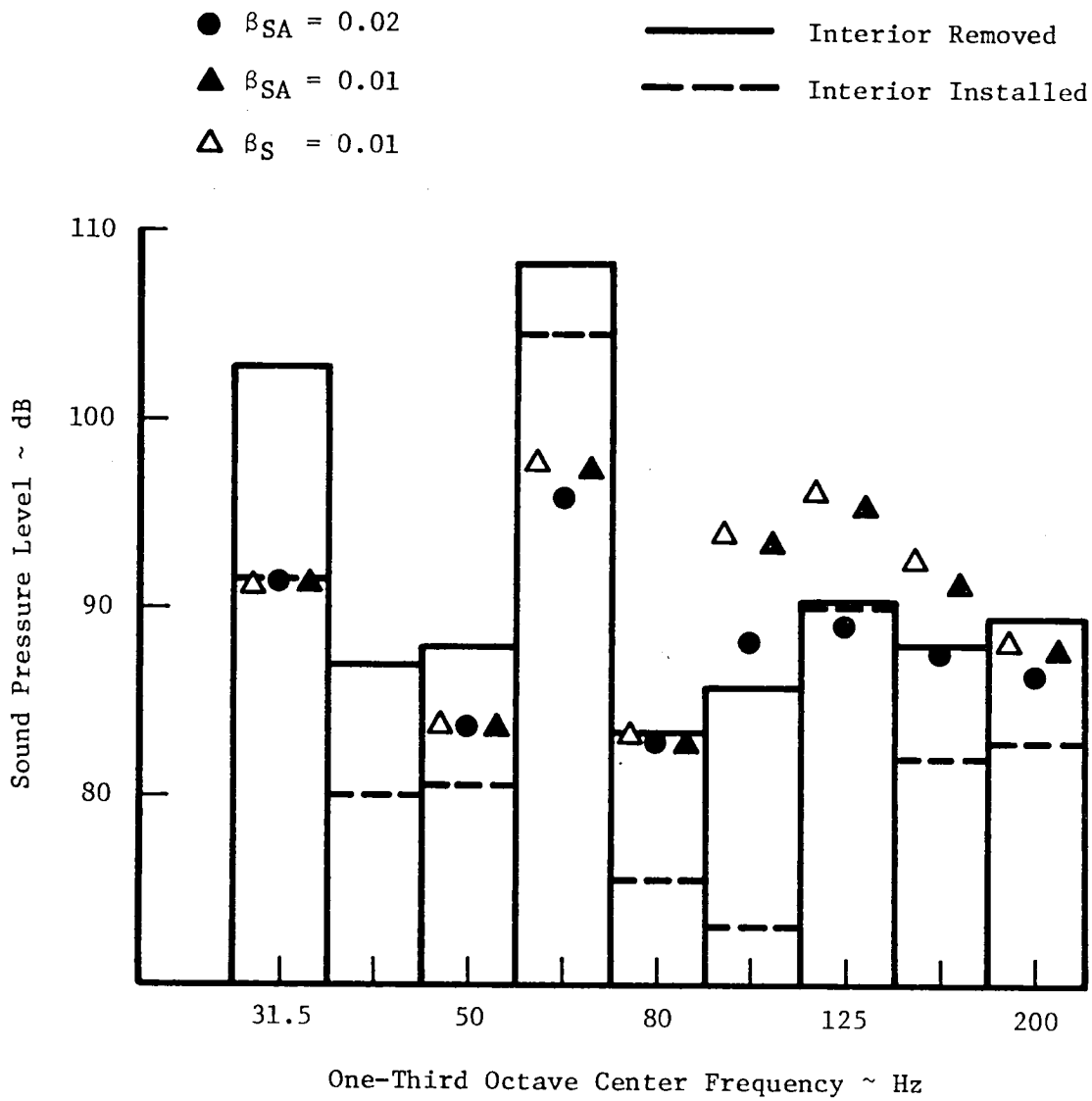

FIGURE 45. PREDICTED ONE-THIRD OCTAVE SPL AT MIR FOR APPLIED ENGINE FORCES; 1920 RPM.

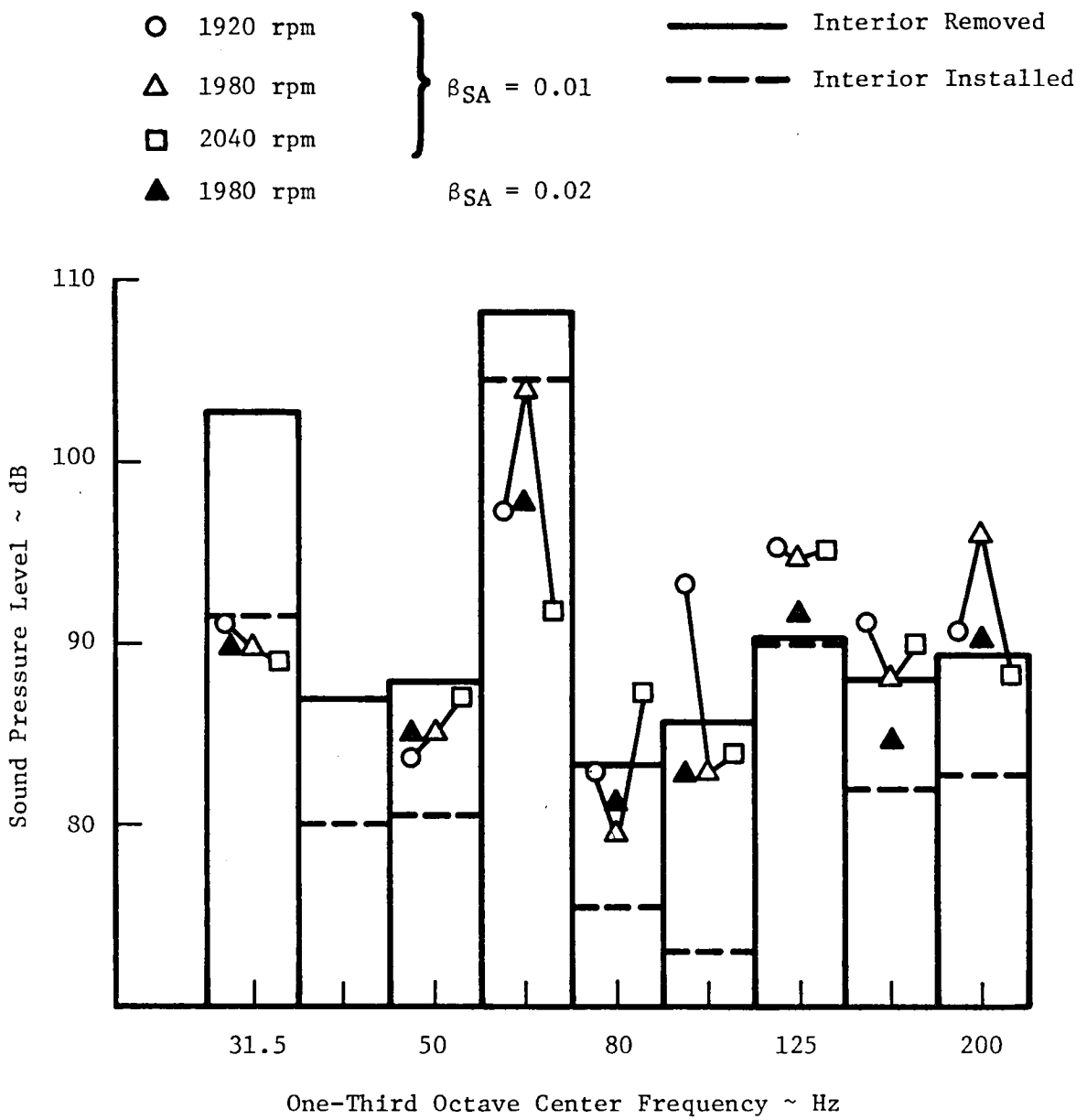

FIGURE 46. PREDICTED ONE-THIRD OCTAVE SPL AT MIR, EFFECT OF CABIN RESONANCE: 1920 RPM.

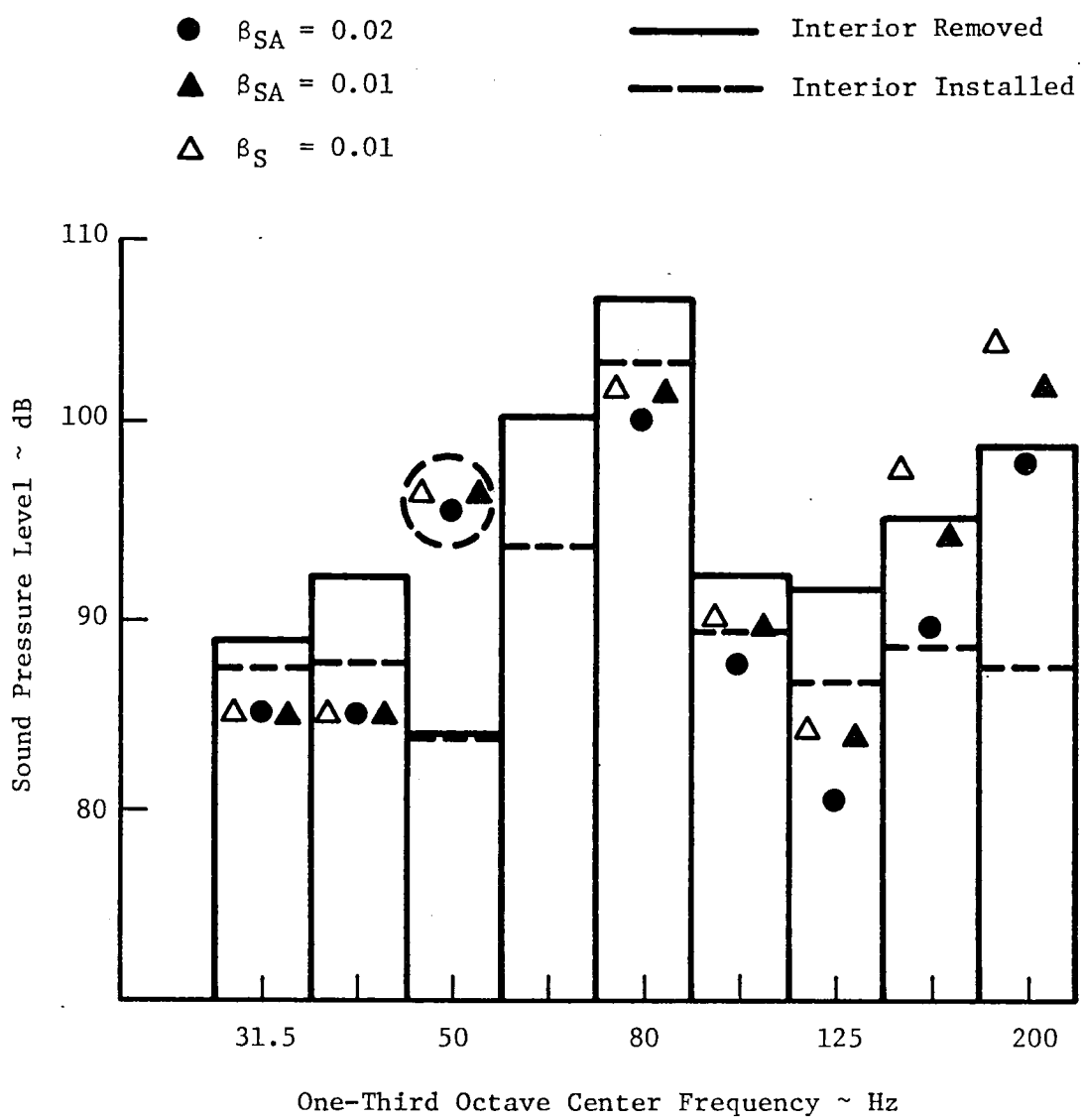

FIGURE 47. PREDICTED ONE-THIRD OCTAVE SPL AT MIR FOR APPLIED ENGINE FORCES; 2160 RPM.

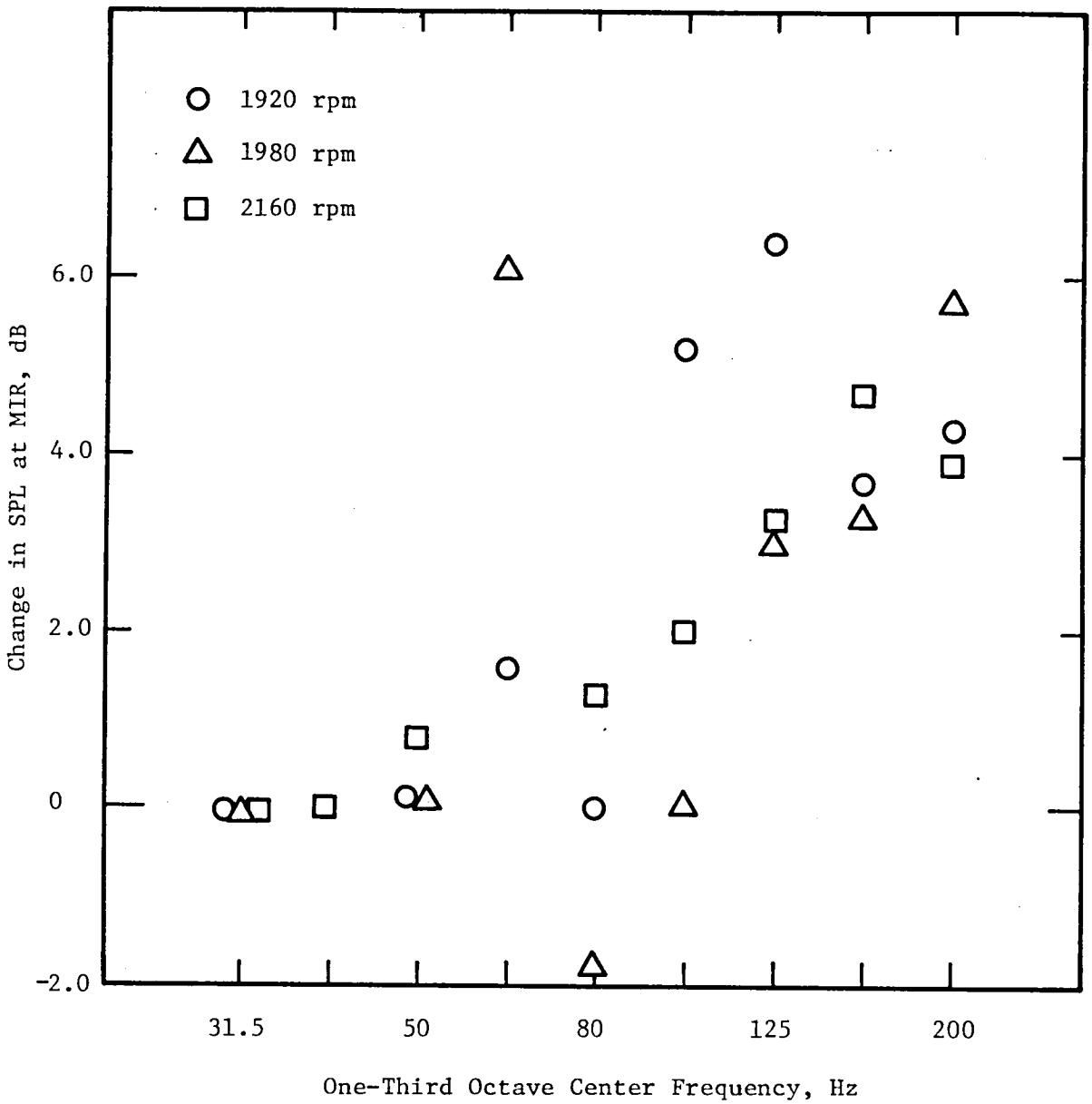

FIGURE 48. EFFECT OF CHANGE IN DAMPING FROM β_{SA} = 0.02 to 0.01 ON INTERIOR SPL AT MIR.

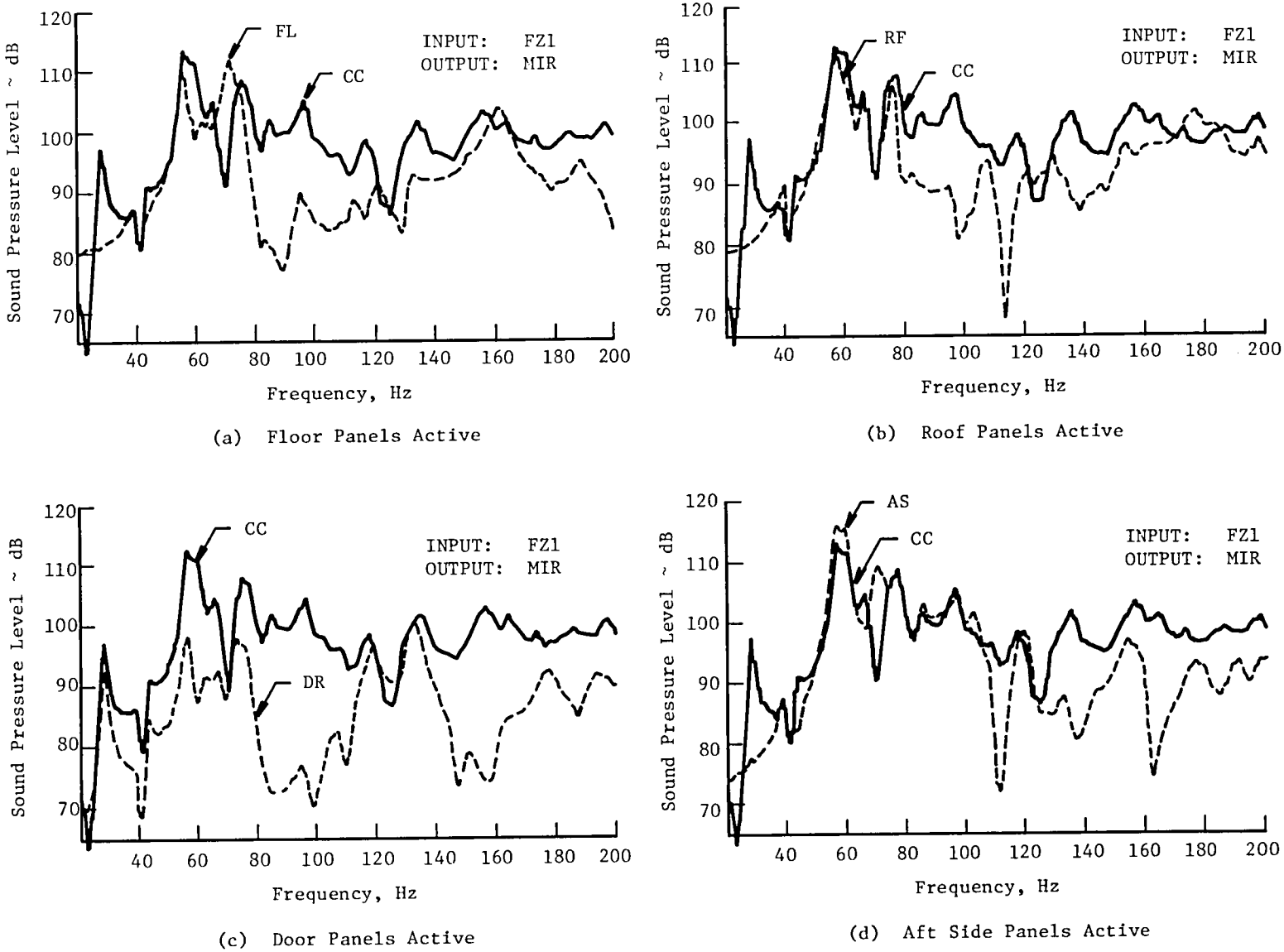

FIGURE 49. EFFECT OF PANEL GROUPS, RESPONSE AT MIR: FZ1 = 44.48 N RMS.

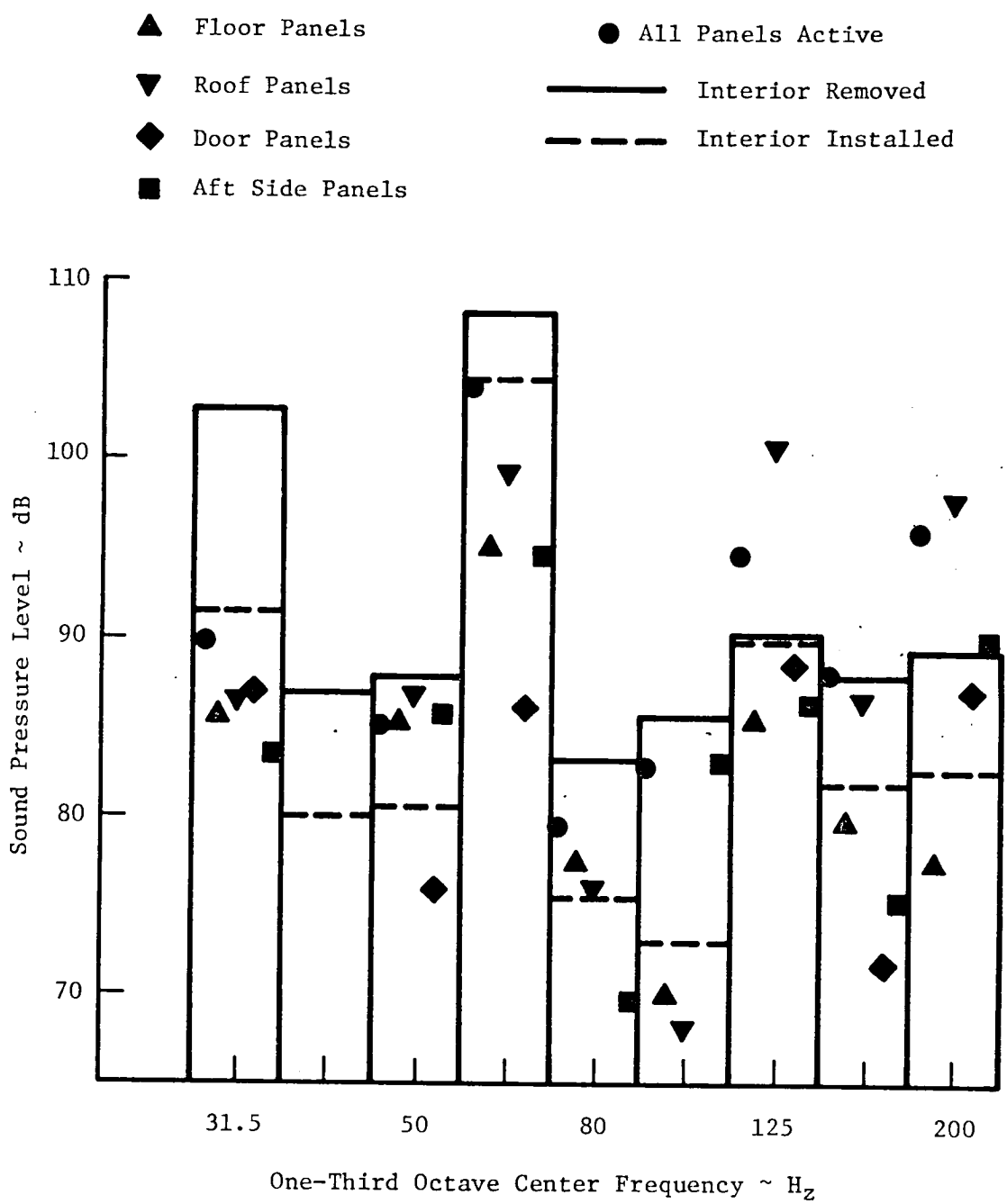

a) 1920 rpm

FIGURE 50. EFFECT OF PANEL GROUPS, RESPONSE AT MIR: APPLIED ENGINE FORCES.

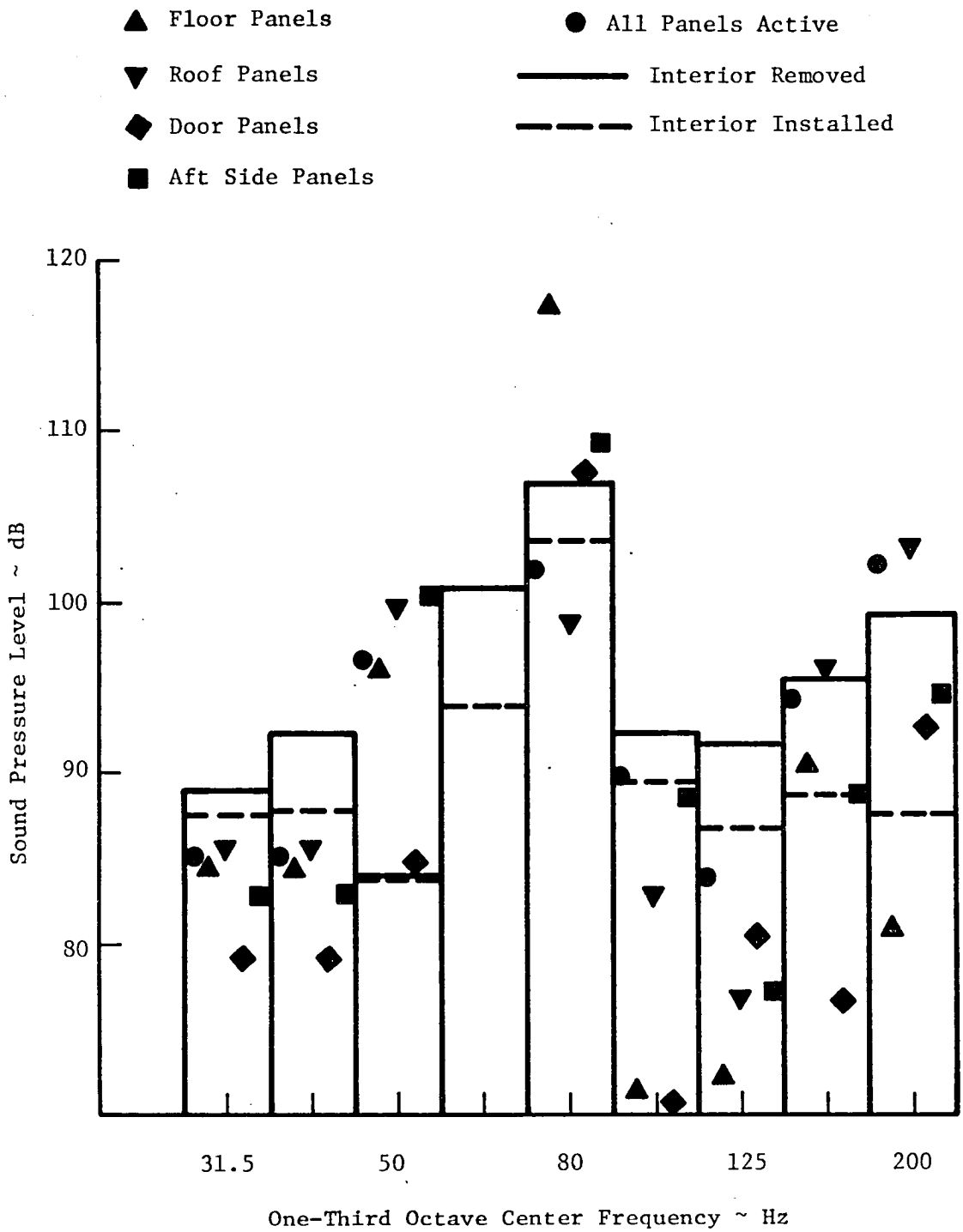

b) 2160 rpm

FIGURE 50 (CONT.). EFFECT OF PANEL GROUPS, RESPONSE AT MIR; APPLIED ENGINE FORCES.